Iron Oxide Nanoparticle Developments for Biomedical Nano-Heating

A Dissertation
SUBMITTED TO THE FACULTY OF
UNIVERSITY OF MINNESOTA
BY

Jacqueline L. Pasek-Allen

IN PARTIAL FULFILLMENT OF THE REQUIREMENTS
FOR THE DEGREE OF
DOCTOR OF PHILOSOPHY

Advisor: John C. Bischof

September 2022

Acknowledgments

This work is the culmination of my academic achievements. I would like to thank my friends and family, especially Tyler Cozort, and Dr. Sarah Lefave for years of discussions and support. I would like to thank Dr. John Bischof, my adviser, for giving me the opportunity to transfer from the University of Utah to the University of Minnesota. His support has been instrumental in my success and professional development. I would also like to thank Dr. Valerie Pierre, my unofficial co-advisor. Through the goodness of her heart and without any personal benefit or responsibility, Dr. Pierre has mentored me in all things related to both chemistry and academia. Without the expertise of Drs. Bischof and Pierre, this work would not have been possible.

The Bioheat Mass Transfer lab and Pierre group have been a wonderful community for research and innovation. I would like to acknowledge Dr. Michael Etheridge, Dr. Zhe Gao, Dr. Hattie Ring, Dr. Kanav Kholsa, Lakshya Gangwar, Randall Wilharm, Dr.Yilin Liu, and Zhonghu Han for their help, brainstorms, discussions, and collaborations.

I also wish to thank Dr. Qi Shao for help with the HDF cell culture, Dr. Gopinath Tata and Todd Rappe at the Minnesota NMR Center for help with HRMAS NMR, Dr. Raj Suryanarayanan for use of the TGA, and Dr. Jon Rainier and Dr. Rameshu Rallabandi for discussions and training. In addition, I thank UMN's Department of Earth Science and Institute for Rock Magnetism for providing instruments and assistance in characterization. Research reported in this publication was supported by the Office of the Vice President of Research, the College of Science and Engineering, and the Department of Chemistry at the University of Minnesota. This work was funded by 5 F31 DK124968-02, NSF EEC 1941543, R01 HL135046, R01 DK117425, and a grant from MicroVention.

Dedication

This dissertation is dedicated to Bde Maka Ska.

Abstract

This work describes iron oxide nanoparticle formulations and heating capabilities for biomedical applications. The coating of iron oxide nanoparticles is key to their dispersion in solution. The heating that results is important for applications including tumor ablation and organ cryopreservation. We propose an iron oxide nanoparticle (IONP)-enhanced precipitating hydrophobic injectable liquid (PHIL, MicroVention Inc.) embolic agent as a localized dual treatment implant for nutrient deprivation and multiple repeatable thermal ablations of deep-seated tumors. Following a single injection, multiple thermal treatments can be repeated as needed based on tumor growth/recurrence. Herein we show the ability to create an injectable solution of stable colloidal dispersion of IONPs with PHIL dissolved in DMSO and monitor deposition of PHIL-IONP precipitate dispersion by μCT and magnetic resonance imaging. Once precipitated, the PHIL-IONP implant can heat to therapeutic temperatures >8 °C for thermal ablation (clinical temperature of +45 °C) in multiple models and in postmortem mouse tissue models. IONPs in other formulations can be used in regenerative medicine such as with "nanowarming" cryopreserved organs. Radiofrequency excited IONPs dispersed in cryoprotectant agents (CPAs) can uniformly rewarm cryopreserved biological samples such as rat kidneys and hearts. To reliably produce IONPs at a scale needed to nanowarm whole human kidneys, a simpler, biocompatible PEG-coated IONP is needed. The IONP needs 1) to be stable in CPAs, 2) have a low volume fraction, and 3) be inexpensive and easy to produce in 10 g batches. We designed a small-molecule phosphonate linker (PLink) which contains a phosphonate "anchor" for high irreversible binding to iron oxide and a carboxyl "handle" for ligand attachment. PLink-PEG removes and replaces the initial coating layer of commercially

available IONPs (EMG1200 (hydrophobic) and EMG308 (hydrophilic), Ferrotec, Inc.) allowing for colloidal stability in both water and CPAs (verified with dynamic light scattering) from minutes (uncoated) to up to 4 weeks. Herein concentrations of IONP in VS55 (common CPA) of 60 mg Fe/mL was reached significantly above our previous capabilities of 10 mg Fe/ mL. These IONPs were successful at nanowarming cryopreserved human dermal fibroblast cells with higher viability as compared to convective rewarming in a water bath and heating rate close to 200 °C/min, 2.5 times faster than our current system. Additionally, initial scale up formulations resulted in 10 g of CPA stable IONPs, which will allow us to significantly accelerate the development of actual kidney cryopreservation and nanowarming for transplantation.

Table of Contents

List of Common Abbreviations

nanoparticles (NPs)

iron oxide nanoparticles (IONPs)

magnetic fluid hyperthermia (MFH)

alternating magnetic field (AMF)

arteriovenous malformations (AVMs)

cryoprotective agents (CPAs)

critical cooling rate (CCR)

critical warming rate (CWR)

specific heat absorption (SAR – W/g Fe)

1,2-distearoyl-sn-glycero-3-phosphoethanolamine (DSPE)

polyethylene glycol (PEG)

meso-porous silica coated IONPs (msIONPs)

silica coated IONPs (sIONPs)

Phosphonate linker (PLink)

polyvinyl alcohol (PVA)

radiofrequency (RF)

magnetic resonance imaging (MRI)

glioblastoma multiforme (GBM)

precipitating hydrophobic injectable liquid (PHIL, MicroVention inc.)

laser interstitial thermal therapy (LITT)

polylactide-co-glycolide (PLGA)

polyhydroxyethylmethacrylate (PHEMA))

dimethylsulfoxide (DMSO)

dynamic light scattering (DLS)

deionized (DI) water

magnetic resonance (MR)

micro computed tomography (μCT)

houndsfield units (HU)

Multi-Band SWeep Imaging with Fourier transformation (MB-SWIFT)

bandwidth (BW)

repetition time (TR)

number of views (N_v)

region of interest (ROI)

specific heat absorption per volume (SAR_V - W/m^3)

specific heat absorption per mass Fe (SAR_{Fe} – W/g Fe)

phosphate buffered solution (PBS)

Institutional Animal Care and Use Committee (IACUC)

inductively coupled plasma mass spectroscopy (ICP-MS)

Weight-average molecular weight (MW)

Number-average molecular weight (Mn)

thermal gravimetric analysis (TGA)

nuclear magnetic resonance (NMR)

high resolution magic angle spin (HRMAS)

human dermal fibroblasts (HDF)

High resolution (HR)

electrospray ionization time-of-flight mass spectrometry (ESI/TOF-MS)

tangential flow filtration (TFF)

List of Tables

List of Figures

Statement of Contribution

This dissertation represents the accumulated research work of the author with contributions from collaborators. The author worked closely with her advisers, Dr. John Bischof and Dr. Valerie Pierre, planning the experiments, analyzing the data, and writing the chapters. The contributions of the author and others are presented below by chapter.

Chapter 1: Introduction

This chapter introduces iron oxide nanoparticles for biomedical applications. Thermal therapy using IONPs for tumor treatment is discussed. This chapter also introduces challenges faced by researchers to cryopreserve organs and describes principles behind radio frequency nanowarming through IONPs.

Chapter 2: Injectable and repeatable inductive heating of Iron Oxide Nanoparticle enhanced "PHIL" Embolic towards tumor treatment

This chapter describes the development of IONPs embedded in PHIL liquid embolic. This work led to the successful implantation of PHIL in postmortem mouse tumor tissue and heating to ablative temperatures. Most of the work in this chapter is taken from the following submitted article (accepted) and reproduced here with the permission of the journal publisher:

Pasek-Allen, J. L.; Kantesaria, S. A.; Gangwar, L.; Shao, Q.; Gao, Z.; Idiyatullin, D.; Han, Z.; Etheridge, M.; Garwood, M.; Jagadeesan, B. D.; Bischof, J. C., (2022), Injectable and repeatable inductive heating of Iron Oxide Nanoparticle enhanced 'Phil' Embolic towards tumor treatment. ACS Applied Materials and Interfaces 2022 (accepted).

Chapter 3: Coating Iron Oxide Nanoparticles

This chapter describes the development of phosphonate coating of IONPs for nanowarming applications. This work led to the successful cryopreservation and nanowarming of human dermal fibroblast cells. Most of the work in this chapter is taken from the following peer reviewed publication and reproduced here with the permission of the journal publisher:

Pasek-Allen, J. L.; Wilharm, R. K.; Gao, Z.; Pierre, V. C.; Bischof, J. C., (2022), Phosphonate Coating of Commercial Iron Oxide Nanoparticles for Nanowarming Cryopreserved Samples. Journal of Materials Chemistry B.

Chapter 4: NMR Characterization of Polyethylene Glycol Conjugates for Nanoparticle Functionalization

This chapter describes the characterization of PEG polymers and conjugation by NMR. This work led to the correct NMR peak identification of 1H-13C NMR coupling in PEG NMR and PEG conjugation yield in coupling reactions. The work in this chapter was taken from a planned submission to Bioconjugate chemistry and reproduced here:

Pasek-Allen, J. L.; Wilharm, R. K.; Pierre, V. C.; Bischof, J. C., (2022), Phosphonate NMR Characterization of Polyethylene Glycol Conjugates for Nanoparticle Functionalization (2022).

Chapter 5: Conclusion and Future Work

This chapter discusses the overall results from the IONP embedded in PHIL liquid embolic heating. Additionally, the formulation of phosphonate coating method of IONPs coatings for stability in CPA and organ cryopreservation is also discussed. Finally, the initial research on coating optimization and scale up is described.

Chapter 1: Introduction

This chapter introduces IONPs for biomedical applications. Thermal therapy using IONPs for tumor treatment is discussed. This chapter also introduces challenges faced by researchers to cryopreserve organs as well as principles behind radio frequency nanowarming through IONPs.

Biocompatible heating with iron oxide nanoparticles

Iron oxide nanoparticles (IONPs) are particles from 1-100 nm in size and consist of a magnetic core, Fe_3O_4 or γ-Fe_2O_3.[1] IONPs with core size under 20 nm are superparamagnetic. These IONPs are attracted to a magnetic field but will return to random spin states through Brownian motion. When an alternating magnetic field is applied to IONPs, the spin state in the particle repeatedly switches, creating localized hyperthermia.[1] This effect may have several applications, including the release of hydrophobically held molecules on the core surface, thermal therapy for tumor treatment, and rewarming of cryopreserved samples.[2-9]

Magnetic fluid hyperthermia (MFH) using magnetic nanoparticles, injected at target location can internally heat from an applied alternating magnetic field (AMF) at low radiofrequency range (40–400 kHz). The temperature increases only where magnetic nanoparticles are located due to magnetic hysteresis losses of superparamagnetic NPs. [10-13] These magnetic NPs are often IONPs as they have been previously FDA approved. IONPs from NanoTherm® in clinical hyperthermia applications have been approved for glioblastoma treatment with AMF (2010) by the European medicines agency and by the FDA (2018) for prostate cancer clinical trials.[14-18] These treatments are designed to have heating properties tuned to cell destruction, but with low collateral toxicity.[19] Unfortunately, IONPs can diffuse with blood flow when injected directly into vasculature, creating a dosage challenge for MFH treatment in highly vascularized, solid tumors. The concentration of IONPs is directly proportional to the heating at the targeted region; therefore, fewer IONPs at a target site from diffusion equates to a less effective treatment.

Previous research has not consistently shown IONPs functionalized with targeting moieties to increase the effective concentration to high thermal therapy concentrations such as those of interest in this study.[20] One option for increasing concentration is to use a non-diffusing solution carrier solution to deliver IONPs. Liquid embolic agents, solutions which are liquid before solidifying or gelling in-situ for embolic or blocking blood flow uses, have been used in the treatment of arteriovenous malformations (AVMs) and other tumors.[21] This may be an option for stabilizing IONPs at the target area.

IONP solutions optimized for nanowarming cryopreserved samples have very different requirements then those used in cancer treatment. Cryopreservation employs vitrification, which is cooling to a glassy state without damaging ice formation. Cryoprotective agents (CPAs) are aqueous solutions containing organic solvents such as dimethyl sulfoxide and glycols as well as salts and sugars which are used in organ cryopreservation.[22-23] These chemical components decrease the critical cooling rate (CCR), the rate needed to vitrify while cooling, and the critical warming rate (CWR), the rate needed upon rewarming to prevent devitrification. The CCR and CWR are functions of the concentration of components.[24] IONPs must be colloidally stable in CPA to perfuse uniformly and maintain heating capabilities at cryogenic temperatures. IONPs should avoid cellular interaction and uptake to maximize removal after perfusion, cryopreservation, or warming.

Nanowarming biological samples requires biocompatible and colloidally stable IONPs (i.e., not aggregated in solution) at concentrations above CWR varying from 0.4 to 50 °C/min depending on the CPA formulation.[23, 25-26] Ideal nanoparticles will have high heating, high specific heat absorption (SAR – W/g Fe), high volume fractions (mg Fe /ml) as a stable dispersion in CPA, and be inexpensive to produce at a scale of >1 g/batch.

Several candidate IONP cores have high SAR as noted in Table 1.1, but none of these are stable in CPA.[7, 27-28] They also tend to aggregate, which can reduce their heating properties for nanowarming and other biomedical applications.[29-30]

Table 1.1: General properties of IONPs.
(SAR at 1 kW RF coil at 25 kA/m and 360 kHz). *EMG1200 SAR in chloroform[3, 7, 31]

IONP	Produced	Coating	Stability		SAR (H_2O) (w/g Fe)	Core size
			Type of solvent	CPA		
EMG1200	Ferrotec	Hydrophobic fatty acid	Nonpolar	No	150	12nm
EMG308	Ferrotec	Hydrophilic surfactant	Aqueous	No	300	12nm
GB - IONP	Bao Lab	Adsorbed PEG	Aqueous	No	2125	40nm

Iron Oxide Nanoparticle Coating methods

The two primary methods for functionalizing IONPs for uniform distribution and biocompatibility are 1) encapsulating the IONP in a shell (i.e., micelle, silica, dextran, or starch), and 2) attaching ligands to the IONP via a linker. Encapsulation using organic ligands such as 1,2-distearoyl-sn-glycero-3-phosphoethanolamine (DSPE) has been tried for stability in CPAs. However, CPAs have organic components which decrease the *Van der Waals* forces, destabilizing the organic layer. This has been shown to cause loss of coating, making the IONPs precipitate out.[28, 32] To address these weaknesses, EMG308 have been encapsulated in silica with a secondary polyethylene glycol (PEG) on the silica. This increases the long-term stability in CPA. [7, 27, 33] For instance, meso-porous silica coated IONPs (msIONPs) were used successfully to rewarm cells and blood vessels; however, they are labor intensive and expensive to make in bulk (1g Fe = $2,000 per human kidney). [27] While silica coated IONPs (sIONPs) are significantly less expensive ($0.50/mg, or $500/human

kidney), they are time-consuming to purify. Furthermore, the silica layer of msIONPs or sIONPs increases the diameter of the IONP roughly 3-fold, thereby increasing the nanoparticle volume fraction 27-fold. This ultimately limits the concentration of nanoparticles which can be used to heat the system. [7, 27]

Linker-enabled ligand attachment directly to the IONP surface addresses these issues. IONPs have different affinities for different functional groups (Figure 1.1). Carboxylic acids have lower affinity to the iron oxide core compared to phosphoric acid. Many IONPs are made with a carboxylic acid fatty acid linked to the core as the simple synthesis gives monodispersed particles. The increased affinity for a phosphonate allows for the simple replacement of almost all carboxylic acid ligands with phosphoric ligands. Replacement of one functional group with a phosphonate through a ligand exchange can change the IONPs' properties. Through ligand exchange, the hydrophobic ligand can be replaced by hydrophilic covalent ligand-core attachment. The result is monodisperse and inexpensive to synthesize.

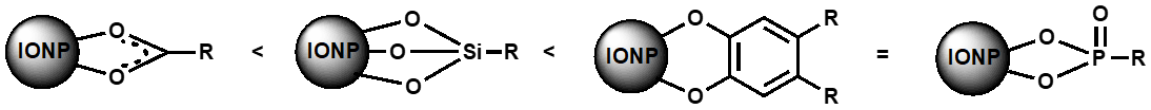

Figure 1.1. Functional group affinity for iron oxide nanoparticle core material. Left to right: Lowest carboxylic acid, silicon oxide, catechol, and phosphonate, highest.

The ideal nanowarming linker will be simple and inexpensive to synthesize, have high affinity for iron oxide, protect the core from further oxidation, metabolize to biocompatible or inert products, and have negligible effect on the IONPs' heating and imaging properties. Several anchors have been used to attach ligands to IONP cores including carboxylates, catechols, and phosphonates.[34-49] Carboxylates have low affinity to Fe and decrease IONP heating capability and are thus a poor choice.[45, 50] Phosphonates and catechols have

excellent iron oxide affinity and preserve core effects and heating.[39, 42, 46-47] For instance, dopamine is an inexpensive, readily available catechol that can be used as both an anchor and a handle.[37, 40, 44] Unfortunately, catechols can be highly unstable and reactive until bound to the core[40, 44, 51] and may increase toxicity because of their reactive side ring.[37, 39-40, 44, 51] Phosphonates have ideal binding geometry and high iron oxide affinity, and they are stable, inexpensive, and easy to synthesize.[35-39, 43, 46-49] Furthermore, phosphonates protect spin layers and magnetism, and they even decompose to stable and biocompatible compounds upon degradation. [46-47, 52] Therefore, a phosphonate anchor with a small hydrocarbon chain terminating with a chemically active end group would theoretically be a versatile yet inexpensive and scalable method for attaching PEG and other ligands onto any IONP core. A phosphonate linker, "PLink," a small molecule intermediary which can link ligands to IONPs without intricate chemistry, was developed for this process. PLink is inexpensive to make and consists of a phosphonate "anchor" and a carboxyl "handle." The anchor has a high affinity to iron oxide, and the handle enables functional molecules to be firmly attached to the IONP without directly binding to it.

Challenges in tumor thermal therapy of Arteriovenous Malformations

Thermal therapy includes thermal ablation. This produces local significant temperature increase above 60 °C for seconds to minutes to destroy tissues or hyperthermia. The less aggressive version increases the local temperature above 43 °C for minutes to an hour.[53] Magnetic fluid hyperthermia (MFH), where magnetic nanoparticles (NPs) are employed, often injected to the target area and an external magnetic field is applied for local heating. Magnetic nanoparticles produce heat through magnetic hysteresis losses at low radio

frequency range (40–400 kHz) of an alternating magnetic field, AMFs.[10-13] In recent decades, AMFs have been used as treatment of glioblastoma, a deep seeded tumor.[10-11, 54] The major challenges with MFH treatment for vascularized, solid tumors, is repeatable and consistent heating to the area of interest.

The loss of injected NPs from the site of injection is a complex combination of active and passive processes. Digestion of IONPs through macrophages, an active process, can take weeks to months. Alternatively, diffusion, a passive process, may take hours to days and likely will speed up with increase temperature in resulting from hyperthermia. Diffusion and uptake vary by tumor and location; therefore, preventing IONP loss combined with identifying and confirming a reliable heating deposit is important for effective treatment.

An option for decreasing loss of magnetic NPs is to combine them with a non-diffusing delivery vehicle carrier such as a liquid embolic agent. Embolic agents reduce blood supply to a tumor bed by blocking the vasculature after injection to target site. There are a range of embolic agents such as particulates and mechanical occlusion devices. Microbead of polyvinyl alcohol (PVA) are often deposited into the tumor bed using a catheter directed to the area of interest. Metal coils have also been used to create a barrier to blood flow. More recently polymeric coils have been studied, and various embolic agents have been used for arteriovenous malformations (AVMs) treatments and for treatment of tumors.[21] Embolization of tumors is generally combined with resection of the tumor afterwards. Unfortunately, resection can miss tumor edges, and these edges can regrow and require secondary treatments. Liquid embolic agents, such as thermos polymers or hydrogels, are injections of liquid solutions which gel or solidify in situ. Magnetic NPs may be added to the initial solution to deliver a high local concentration of magnetic NPs to a tumor vascular

bed or interstitium. The delivered magnetic NPs will be trapped within the solidified embolic. This can then be coupled with an alternative magnetic field to produce local hyperthermia with minimal concentration loss. Combining thermal therapy (with magnetic NPs) with embolization using a liquid embolic agent may allow for maximum heating to destroy both the tumor and edges prior to resection. Furthermore, if the embolic agents and trapped magnetic NPs are stable in-situ, tumor growth can be monitored after the first injection. Multiple heat treatments can then be applied as needed based on long-term tumor monitoring with eventual tumor and embolic resection at optimal timing for patient.

Recently, radiofrequency (RF) heat treatments using iron-oxide nanoparticles (IONPs) in embolic agents have been explored. Alginate hydrogels entrapping magnetic nanoparticles have been studied for localizing thermal therapy.[55] IONP-loaded nanocapsule hydrogels, which are injectable, biodegradable, and thermosensitive with IONP heating, have had success with multiple heat treatments in mice and are observable with magnetic resonance imaging (MRI) contrast.[56] These liquid embolic agents made with hydrogels degrade over one month in aqueous solutions and show decreased heating capabilities after two weeks.[56] Hydrogels' inherent affinity for water allows for the gel degradation in situ and results in IONPs loss. Degradation is thermodynamic; this means that with every additional RF heat treatment, degradation is further intensified.[56] Tumor growth generally requires at least one week to determine effect of treatments after clinical MHF.

Liquid embolic agents without hydrogels or water dissolving constituents provide a better framework for multiple heat treatments. Onyx is a non-hydrogel liquid embolic agent, which when combined with magnetic NPs results in sediments of the compounds in solution. Onyx-containing solutions must be mixed immediately prior to injection and must

have imaging artifacts.[57] Magnetic nanoparticles which enable quantitative imaging and predictive heating have made MFH an attractive thermal therapy. Successful development of this combination will allow for minimally invasive, targeted therapy treatment of complicated vascularized solid tumors, such as glioblastoma multiforme (GBM) and hepatic tumors.

Challenges to cryopreserve organs

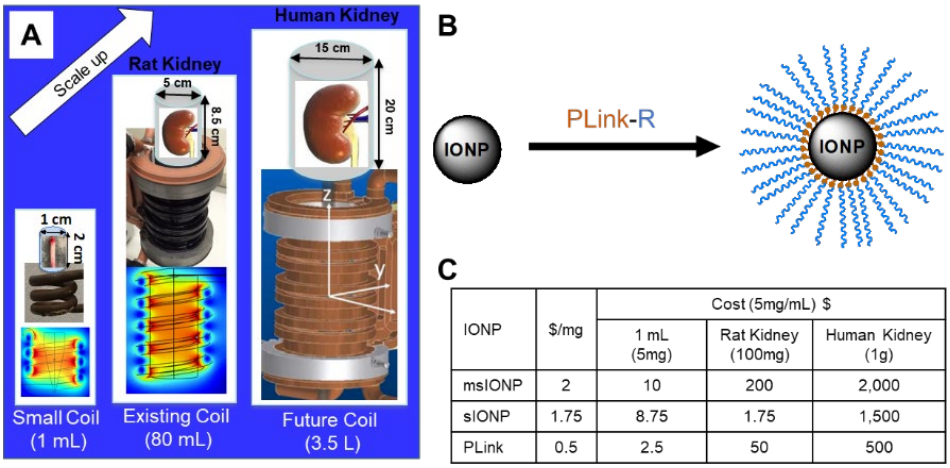

IONP	$/mg	Cost (5mg/mL) $		
		1 mL (5mg)	Rat Kidney (100mg)	Human Kidney (1g)
msIONP	2	10	200	2,000
sIONP	1.75	8.75	1.75	1,500
PLink	0.5	2.5	50	500

Figure 1.2 Scale up goals of organs cryopreservation and nanowarming. **A:** Scale up of kidney nanowarming and radiofrequency coil. **B**: PLink coating method. **C**: Cost comparison of nanowarming IONPs.

Our inability to preserve donor organs for more than a few hours significantly contributes to organ shortages, poor organ matching due to harsh immune suppression and graft rejection, and limitations to the length and quality of life for organ transplant recipients.[58-69] Longer term organ preservation would alleviate many of these issues and, as such, has been identified as a key priority by the NIH, the American Society of Transplantation, and other major transplant societies.[5, 58, 70-71] Considering kidney transplants, the waitlist comprises 83% of the overall U.S. organ transplant waitlist[72]. Yet every year thousands of potentially transplantable kidneys

are discarded when their preservation limits are exceeded.[58, 60] More specifically, for every five kidney waitlist patients who do not receive a new organ in time, three kidneys are discarded.[58]

Using carefully optimized protocols and CPAs developed over many years, we have successfully cryopreserved multiple tissues and animal organs including kidneys in an ice-free vitreous "glassy" or "amorphous" state, allowing for indefinite storage.[26, 73-77] However, significant challenges still exist in rewarming organs and CPA toxicity. Advances in vitrification require fast and uniform warming to avoid crystallization or cracking that reduce viability of tissues or organs upon rewarming. For this reason, traditional convective rewarming is successful only for smaller systems (1-3 mL). Fortunately, "***nanowarming***" (radiofrequency excited iron oxide nanoparticles (IONPs)) **can be** deployed within CPAs to successfully rewarm vitrified biosamples and rabbit kidneys up to 80 mL without crystallization or cracking.[27]

To translate this nanowarming technology, IONPs must be producible at scale of >1g, biocompatible, high heating, evenly dispersed throughout a CPA, and allow for image-based quantification.[27] There are many challenges facing successful deployment of IONPs in cryoprotective agents and further in perfusion of organs. IONPs must remain a stable colloidal dispersion in CPAs during perfusion and washout of an organ. In addition, IONPs must be biocompatible and be produced at a large scale with a low cost for research and development and eventual deployment into human organs, which demands a 1 L volume (Figure 1.1A). Since bare IONPs generally are not biocompatible and tend to aggregate in CPAs, they require a coating for biocompatibility and even dispersion.[34, 41, 78-79] While multiple methods to coat IONPs have been reported (using silica, starch, dextran and adsorbed PEG, for example), a simple, scalable, cost-effective coating method that

maintains high heating and imaging in CPAs has proven elusive. For instance, we have shown that PEG-coated silica IONPs can be used for nanowarming in small animal models and *in vitro* testing, but at more than $2/mg Fe, they are expensive and labor intensive for clinical applications (i.e., $2,000 per human kidney, Figure 1.1C).[27, 33] We hypothesize that a phosphonate-based linker (PLink) will allow for large scale, direct coating (Figure 1.2B of PEG onto IONPs). We further hypothesize that CPA-optimized PLink IONPs can be deployed within CPAs for human kidney cryopreservation and nanowarming for $0.50/mg Fe (i.e., $500 per human kidney).

Chapter 2: Injectable and repeatable inductive heating of Iron Oxide Nanoparticle enhanced 'Phil' Embolic towards tumor treatment

This chapter describes the encapsulation of Iron oxide nanoparticles in precipitating hydrophobic injectable liquid (PHIL, MicroVention inc.) for heating of embolic implant. This work led to the development of a liquid to solid injection in tumor tissue as well as successful 15-minute heating profile. Most of the work in this chapter is taken from the following peer reviewed publication and reproduced here with the permission of the journal publisher:

Pasek-Allen, J. L.; Kantesaria, S. A.; Gangwar, L.; Shao, Q.; Gao, Z.; Idiyatullin, D.; Han, Z.; Etheridge, M.; Garwood, M.; Jagadeesan, B. D.; Bischof, J. C., Injectable and repeatable inductive heating of Iron Oxide Nanoparticle enhanced 'Phil' Embolic towards tumor treatment. ACS Applied Materials and Interfaces 2022 (accepted Pending revisions)

SUMMARY

Deep-seated tumors of the liver, brain, and other organ systems often recur after initial surgical, chemotherapeutic, radiation, or focal treatments. Repeating these treatments is often invasive and traumatic. We propose an iron oxide nanoparticle (IONP) enhanced precipitating hydrophobic injectable liquid (PHIL, MicroVention inc.) embolic as a localized dual treatment implant for nutrient deprivation and multiple repeatable thermal ablation. Following a single injection, multiple thermal treatments can be repeated as needed, based on monitoring of tumor growth/recurrence. Herein we show the ability to create an injectable stable PHIL-IONP solution, monitor deposition of PHIL-IONP precipitate dispersion by μCT, and gauge the IONP distribution within the embolic by magnetic resonance imaging. Once precipitated, the implant could be heated to reach therapeutic temperatures > 8 °C for thermal ablation (clinical temperature of ~45 °C), in a model disk and a 3D tumor bed model. Heat output was not affected by physiological conditions, multiple heating sessions, or heating at intervals over a 1-month duration. Further, in ex vivo mice hind-limb tumors, we could non-invasively heat the embolic to an "ablative" temperature elevation of 17 °C (clinically 54 °C) in the first 5 min, and maintained temperature rise over +8 °C (clinically a temperature of 45 °C) for longer than 15 min.

INTRODUCTION

There are an increasing number of reports on photothermal therapies (over 1600 in 2021 according to PubMed) especially since the groundbreaking work of Hirsch, et al. with photothermal nanoparticle heating.[80] However, this type of laser nanoparticle based

treatment (or laser alone) can only be applied within roughly a cm from the laser source due to light attenuation in tissue.[81] Embolics are generally used to treat much deeper cancer of the liver and abdominal organs.[82] Admittedly, laser interstitial thermal therapy (LITT) can be used to treat deeper tissue cancer such as gliomas, but this requires a diffuse tip laser that can be inserted in the tissue and to our knowledge cannot be used with embolics.[83] Thus, we have emphasized the use of radiofrequency fields which can penetrate into deeper tissues and selectively heat iron oxide nanoparticles such as has been performed in magnetic fluid hyperthermia.[84] Importantly, the concept of heating magnetic materials which can be dispersed in an embolic cannot be achieved by photothermal therapy.

The use of combination embolization and thermal therapy for oncology treatments has been explored due to advancements in radiofrequency (RF) energy delivery devices and technologies.[56, 85] Thermal therapy is generally either thermal ablation, which produces rapid localized heating within seconds to minutes to destroy tissue, or hyperthermia, which elevates local temperature by several degrees above normal body temperature for an extended period.[53] Magnetic fluid hyperthermia (MFH) is an emerging non-invasive thermal therapy in which magnetic nanoparticles (NPs) are injected into an area of interest and then externally heated due to magnetic hysteresis losses in the presence of an alternating magnetic field (AMF) at a low radiofrequency range (40–400 kHz), leading to elevated temperatures in the treated area.[10-13] Heating rate iron oxide nanoparticles are effected by: core size, morphology, phase, and concentration.[86] Optimizing core formulation for increased heating is a complex field of research outside the scope of this study. Increasing concentration of the IONPs is an equally effective way to increase heating repeatably. Low frequency electromagnetic fields (or AMFs) have been applied for human

use, such as treatment for glioblastoma, in the past few decades.[10-11, 54] Because the interaction of electromagnetic fields with tissue induces eddy current–based Joule heating, which is proportional to the frequency of these fields, the low frequency range (<400 kHz) is ideal for avoiding non-specific tissue (eddy) heating during a heating treatment. For these low frequencies there is no significant tissue attenuation, so deeper penetration can be achieved, which is useful for deep tumor applications.[87] For clinical use, homogeneity of the alternating magnetic fields is critical for ensuring spatial uniformity of power deposition in tissue as a measure of patient safety.[88-89]

Further, as eddy current heating also depends upon the size of the treated system, the product of magnetic field strength (H) and frequency (f) could be limited to a threshold value (such as 4 kA/m and 150 kHz for a ~30 cm diameter based on the size of the human torso)[90] for avoiding any potential inhomogeneity in heating, i.e., heating of normal tissue of a patient. MFH has several advantages over other thermal therapy delivery approaches (e.g., RF, ultrasound, microwave, or laser ablation), including being minimally invasive, enabling increased penetration of magnetic field in tissues, and improving accumulation of magnetic NPs in tumors via magnetic targeting, as well as selective heating through power deposition at specific targets.[91] This is promising for treatment of localized, vascularized, solid tumors, such as glioblastoma multiforme (GBM), hepatic tumors, etc., as minimally invasive, targeted therapy minimizes complications. The development of magnetic nanoparticles that enable quantitative imaging and predictive heating has made MFH a promising thermal therapy.

Effective MFH treatment for vascularized, solid tumors, however, remains challenging, as injected NPs solutions can quickly diffuse. Heating efficacy is directly related to the

concentration of magnetic NPs at the targeted region, and NP diffusion results in lower heating and a less effective treatment. The ability to increase the concentration of magnetic NPs or the heating efficiency is promising, particularly since it would not lengthen treatment time.[92-93] Previous work has shown that adding targeting functionalities to magnetic NPs' coating still results in low accumulation in the area of interest.[20] A potential way to increase local delivery of magnetic NPs and decrease their diffusion is to combine them with a non-diffusing carrier such as a liquid embolic agent. Liquid embolic agents—liquid injections that gel or solidify in situ—hydrogels, or thermo polymers have been used extensively in the past for treatment of arteriovenous malformations (AVMs) and more recently for treatment of tumors.[21] They work by reducing blood supply to the tumor and producing ischemia. When they are combined with magnetic NPs, they can be used to deliver a high local concentration of magnetic NPs to a tumor vascular bed or interstitium. The magnetic NPs can then be used to achieve local hyperthermia. The combination of embolization (with the liquid embolic) and hyperthermia (with the magnetic NPs) can allow for heating tumor beds prior to resection of the tumor or for ablating the tumor margins following resection of the tumor. Multiple heat treatments based on long-term tumor monitoring will ideally prevent tumor recurrence at the margins of resection cavities.

Iron-oxide nanoparticles (IONPs) in embolic agents for RF heat treatments have been explored in recent years. Alginate hydrogels have been proposed for localizing the incorporated magnetic microparticles.[55] Furthermore, injectable, biodegradable, thermosensitive, and superparamagnetic iron oxide nanoparticle-loaded nanocapsule hydrogels have been demonstrated to be effective with multiple MFH and long-term magnetic resonance imaging (MRI) contrast.[56] In previously published literature,

embedding magnetic NPs in liquid embolics has only been shown to preserve magnetic NP heating for up to 2 weeks.[56] Multiple heat treatments have been shown to decrease tumor growth.

Several previously demonstrated drawbacks remain with RF heat treatments in embolics. Onyx, another liquid embolic that has been previously combined with magnetic NPs, is a suspension that sediments over time, requiring mixing immediately before injection.[57] Hydrogels' water stability also fosters the degradation of the gel in physiological systems, as the gel resolubilizes. Degradation of gel matrix results in loss of IONPs and is further exacerbated by heat from RF treatments.[56] One week is typically needed to observe whether tumors are growing after a clinical MHF[94]; if heating is not consistent over a week, it cannot be tailored to the patient. There is the clear need to improve the combination of MHF with embolization for multiple heating regimes adapted to the growth of the tumor.

To address these shortcomings, we propose a commercial shelf-stable liquid embolic that acts as an implant to provide consistent and predictable heating and is not degraded by physiological conditions or RF heating. PHIL, precipitating hydrophobic injectable liquid, is a liquid embolic agent that can be combined with magnetic NPs for this purpose. PHIL "is composed of a nonadhesive copolymer (polylactide-co-glycolide (PLGA) and polyhydroxyethylmethacrylate (PHEMA)) dissolved in DMSO [dimethylsulfoxide] with an iodine component (triiodophenol) covalently bound to the copolymer, causing radiopacity."[95] The precipitated hydrophobic injectable polymer (iodinated PLGA-PHEMA polymer) will be referred to as PHIL, when in solution it will be referred to as PHIL-DMSO. PHIL has been clinically tested in humans and has shown to remain stable in vivo for months.[57, 96-97] As PHIL is not a hydrogel and not soluble in water, it will have

long-term stability as a framework to support magnetic NPs. Magnetic NPs need to be colloidally stable in PHIL-DMSO, have high heating capacity, and have predictable heating measurable through imaging. IONPs are often used for heating, and their coatings significantly affect their stability in various solutions. EMG308 (commercial IONP by Ferrotec inc. referred to as EMG) and silica-coated EMG (referred to as sIONP) have been tested in DMSO-containing solutions to varying success.[3, 7]

This pilot study investigated the potential for future noninvasive vascularized tumor treatment by injection of a liquid embolic PHIL and silica-coated iron oxide nanoparticle (sIONP) mixture in combination with RF heating.

MATERIALS AND METHODS

Materials

Unless otherwise noted, starting materials were obtained from commercial suppliers and used without further purification. Commercial IONPs, EMG308, was purchased from Ferrotec inc. The sIONPs were synthesized as we have previously reported. Briefly EMG308 is coated with silica and PEG silane, and purified using centrifugation.[7] All sIONPs batches are characterized by TEM, DLS, ICP-OES, and a heating generation (specific absorption rate [SAR]) to previously published values for 18 nm silica shells. PHIL polymer was supplied in powder form by Microvention Inc under a proprietary process.

Preparation of IONPs with PHIL in DMSO Solutions

Seven solutions of PHIL-DMSO with IONPs were made following formulations in Table S1. Powdered PHIL (25 g) was added to DMSO (66.667 g) and heated to 60°C for approximately 30 min with intermittent shaking until PHIL was completely dissolved and was used as a PHIL-DMSO stock solution. sIONPs (1.63 g) were added to DMSO (1.66 g) and point-sonicated for 15 min at room temperature. EMG (0.081 g) was added to DMSO (1.96 g) and point-sonicated for 15 min at room temperature. PHIL-DMSO solution (11g) was added to each of seven vials, sIONP-DMSO solution was added to appropriate vials (one, 0.411 g; two, 0.822 g; and four, 1.644 g) and EMG-DMSO solution was added to appropriate vials (one, 0.265 g; two, 0.530 g; and four, 1.061 g). Remaining DMSO was then added (Zero: 1g, sIONP one: 0.753 g, sIONP two: 0.495, EMG one 0.755g, EMG two: 0.501g). Solutions were vortexed to mix.

Stability of IONPs in Solutions

Dynamic light scattering (DLS) samples were made by adding PHIL-DMSO stock solution (1.393 g), DMSO (0.127 g), and either sIONP-1 or EMG-1 (0.48 g) solutions to make 0.1 mg Fe/mL solutions. The samples were visually observed and DLS was measured using a standard method for size for 10 days as previously reported.[7] Nanoparticle size was determined by DLS measurements on a Brookhaven Zeta PALS instrument (Brookhaven Instruments Corporation) with a 635 nm diode laser at 15 mW of power. Stability of colloidal suspension was determined by DLS time points at the same concentration, taken several times in the first 24 h and then on daily or weekly intervals up to 10 d.

Measurements were stopped when visual precipitation occurred. Stability was tested in DMSO and PHIL-DMSO.

Tablet Formation and Imaging Sample Preparation

To form the tablet for imaging, a mesh cell strainer was placed in a jar lid and surrounded with approximately 0.5 cm of deionized (DI) water. To make a precipitate disk approximately 1.5 cm in diameter, 0.3 mL of PHIL-DMSO and PHIL-DMSO-IONPs (1, 2, and 4 mg Fe/mL solutions) were pipetted gently into the water (Figure 1). After approximately 30 s, an exterior shell formed, and additional DI water was gently pipetted around the mesh filter to cover the precipitate disks. Once well formed, the PHIL tablet disk was transferred using the mesh filter to a 125 mm diameter crystalizing dish filled with 1 in of fresh DI water (200 mL). DI water was refreshed three times before leaving the samples overnight.

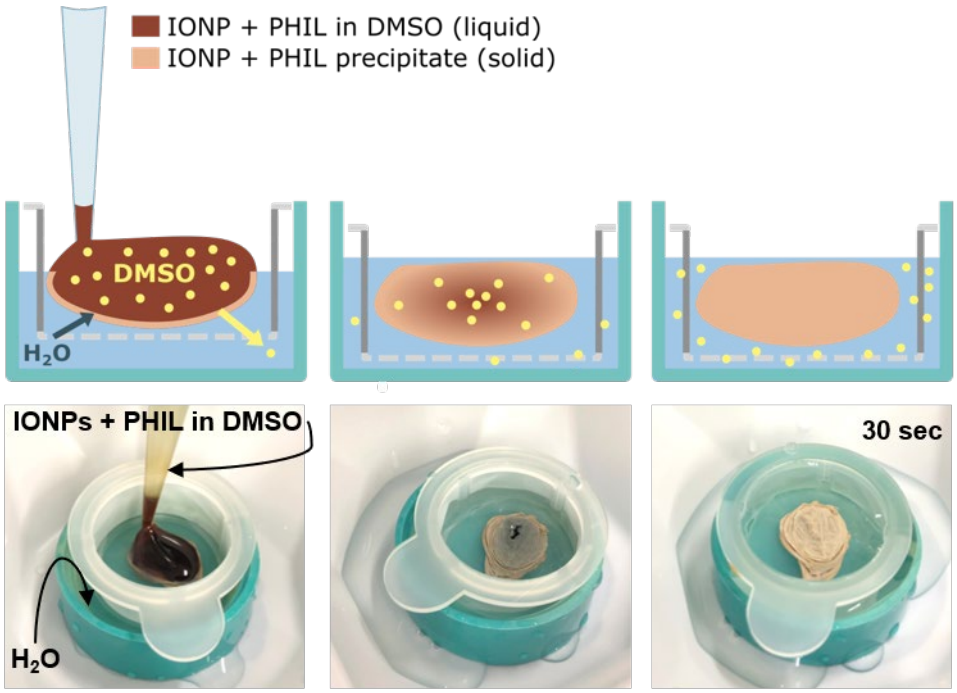

Figure 2.1. Precipitation of IONP embedded in PHIL. Top: cartoon of precipitation of PHIL-IONP tablet in water. Yellow dots denote DMSO molecules. Bottom: photo time-lapse of PHIL-IONP precipitation. On contact with water, DMSO instantaneously diffuses out from the PHIL-IONP solution and exchanges with water, resulting in PHIL precipitation due to insolubility in water. The area of precipitate contacting the water displaces DMSO the fastest, creating a highly porous shell. The desired shape is made by the solution quickly extruding into an enlarging initial shell. Once the final structure is formed, DMSO continues to diffuse outwards from center of precipitate. Fresh water is replaced multiple times over the first 4 h, and samples are left overnight in 200 mL of distilled water to ensure all DMSO is removed. The surrounding solution remains clear, indicating minimal to no leakage of IONPs.

Samples were placed in a 2 cm diameter nuclear magnetic resonance (NMR) tube, layered with Teflon spacers to ensure tablets were in magnetic resonance (MR) coil area and for separation, and the tubes were filled with fresh DI water before running both MR and μCT imaging. MR and μCT imaging was completed on the tablet samples.

microCT Imaging of IONPs in PHIL

The samples were scanned in a μCT imaging system (NIKON XT H 225, Nikon Metrology, MI). The accelerating voltage was set to 121 kV, and the current was set to 150 μA. The resolution was 0.053 mm. A 1-mm aluminum filter was placed between the source and the object to reduce the beam-hardening effect. The images were reconstructed to reduce the beam-hardening effect and improve image quality using vendor provided software (3D CT pro, Nikon Metrology, MI). The images were then imported as unsigned 16-bit float images, post-processed (VGstudio Max 3.2, Volume Graphics, NC), and exported as DICOM images for a final analysis using MATLAB (MathWorks). The grayscale values were transferred into houndsfield units (HU) based on the air and water samples in MATLAB.

MR Imaging of IONPs in PHIL

MR imaging was performed in multiple sessions on a 16.4-T, 26-cm bore magnet (Magnex Scientific, Yarnton, UK) interfaced to a research spectrometer (Varian, Palo Alto, CA). A single-loop surface coil (diameter = 2.5 cm) was used for RF transmission and signal detection. The pulse sequence was achieved using Multi-Band SWeep Imaging with Fourier transformation (MB-SWIFT) combined with a Look-Locker acquisition scheme designed to measure the longitudinal relaxation time (T_1) of rapidly decaying water signals [98-100]. Parameter settings included acquisition bandwidth (BW = 500 kHz), repetition time (TR = 1.32 ms), longitudinal recovery delay (t = 97.154 ms - 2857.154 ms; 16 linearly spaced points), flip angle (1°), RF pulse length (2.0 μs), acquisition delay (1.7 μs), gaps (2), and total acquisition time (~14 min). The number of views (N_v) and number of complex points (N_{spiral}) were adjusted between N_{spiral} = 440 or 400 and N_v = 100 or 80, respectively, depending on the image size. The field of view (FOV) varied from 30–40 mm in x, y, and z, depending on the sample size with a resolution of 256 × 256 × 256 pixels.

All MB-SWIFT images were reconstructed using an in-house C++ program and VnmrJ version 3.2.

Image Analysis

A MATLAB (MathWorks) script was used to determine both the mean T_1 and HU of each tablet. To determine the relaxation rate constant R_1 (= $1/T_1$) and HUs of a given PHIL tablet, a circular region of interest (ROI) was manually selected in the approximate middle

slice of a given tablet for the T_1 map and microCT (μCT) image stacks. The mean T_1 and HUs were taken for this ROI, ignoring T_1 values < 0 s and > 1.5 s and removing outliers more than 3 median absolute deviations from the mean. The T_1 values were then converted to R_1 values by taking the reciprocal.

A separate MATLAB (MathWorks) script was used to determine the mean R_1 for the center cross section of the 1 mg Fe/mL tablets as a function of distance from the closest edge of the tablet to approximate distribution of IONPs within the tablet. A cross section without any visible artifacts or bubbles was taken from the center of each 1 mg Fe/mL PHIL-sIONP tablet T_1 map, which again was converted to R_1 values by taking the reciprocal of the T_1 value at a given pixel. The outline of this tablet was manually drawn using ImageJ, and the entire image was converted to a binary image via thresholding for nonzero pixels.[101] The distance transform of this was then computed for the inverse of this image, and the mean R_1 as a function of distance from the edge of the tablet in bands of 5 pixels (0.586 mm) was then plotted as a moving average from the edge of the tablet toward the center. ImageJ was also used to create a 3D surface plot of a representative cross section of one of these PHIL-sIONP tablets from the manually outlined MR image.

Heating Characterization of IONPs in PHIL tablet

Heating experiments were performed in a 15 KW RF system on a PHIL-IONP tablet precipitated using the same method as for the imaging with the addition of a fiber optic, as shown in Figure S3. Following immersion in DI water overnight, tablets attached to fiber optics were placed into a container with fresh DI water (approximately 5 mL) before the heating run. PHIL-IONP coprecipitate tablets were heated using a 15 kW (at 60 kA/m, 175

kHz) custom-built RF coil with 5 cm ID (~80 mL capacity) (Fluxtrol, Auburn Hills, MI).[27, 29, 33, 102] Each sample was heated three times for 60 s. A fiber optic temperature probe (Qualitrol, Fairport, NY) was used to collect the temperature inside the system. Fe was later quantified using ICP or relaxometry. The thermometry data was later analyzed to calculate temperature rise ($\Delta T = T_{final} - T_{initial}$) as well as SAR_V, which is the power deposited per unit volume (in W/m^3), using the combined heat capacity of the water and PHIL tablet along with the initial slope, i.e. first 30 s of temperature rise recorded using the time rise method. [103-104] For a representative SAR_V calculation and details about the governing equation, refer to SI.

Heating Characterization of PHIL-sIONP in an agarose 3D AVM model

We demonstrated PHIL-sIONP coprecipitation in an agarose 3D AVM model designed from a silicone model provided by MicroVention (Figure S8). The 3D model consisted of "an afferent tube, representing the feeding artery, supplying the artificial nidus; a round, flat, honeycomb-like 3D space; and 3 efferent tubes, representing 3 draining veins."[95] The silicone of the provided model inductively couples to the coil and thus could not be used for heating runs. A clay reverse imprint of the AVM model was recreated to have dimensions of 2 inches diameter and 1 cm thickness. 3% Agarose (3g) in water (97 mL) solution was made by heating the mixture until completely dissolved and then immediately poured into the clay imprint model. Once cooled, the agarose model was removed from the mold, attached to a water pump flowing at 1 mL/min, with 3-way connecter attached 1 inch from the drain inlet, and clamped between two pieces of 1cm plexi-glass. After equilibrating the 3D agarose model with water, 0.5 mL of 4 mg Fe/mL PHIL-DMSO with

IONPs was injected into the center of the honey comb area of the model. This was completed under continuous water flow, following the previously established procedure.[95] The sample was allowed to cure for 20 minutes at 1 mL/min of water flow, and then removed from the plexi-glass set up. The agarose model was then attached to a 3D printed holder and placed inside a120kW (at 365 kHz) RF Coil with maximum field strength of ~35.2 KA /m (Fluxtrol, Auburn Hills, MI). Three trials of heating for 60 seconds were performed for each sample. An Infrared camera (FLIR A300 Thermal Imaging Camera, Teledyne FLIR LLC, Oregon) was used to record the temperature inside the system and the data collection is procured using the ThermaCam Researcher Pro Software. The thermometry data was analyzed by evaluating temperature rise over 60 seconds at three locations on the agarose model face. The amount of Fe in the coprecipitate was later quantified using relaxometry.

Heating Characterization for Long-Term Repeatability in Physiological Conditions

Heating data was analyzed using a 1 kW (RF coil) Hotshot inductive heating systems with a 2.75-turn, water-cooled copper coil (Ameritherm Inc., Scottsville, NY). A blunt-tip needle was used to place 1 mL phosphate buffered solution (PBS) solution in the center bottom of a 2 mL cryotube, and 1 mL of PHIL-DMSO or 8 mg Fe/mL PHIL-DMSO-sIONPs solution was injected into the cryotube through the PBS and around the needle. The needle acted as both a placeholder for the future thermocouple and a method to inject water into the bottom of the tube to force DMSO up while precipitating PHIL. The surrounding solution was removed and replaced by injecting PBS through the needle and removing excess solution from the top, which was repeated with 15 mL of PBS for five

times over 1 h. Sample solution and needle were then completely removed and 1 mL of PBS was added. The weight was recorded. The cryotube was capped with a rubber stopper, and a fiber optic temperature probe was placed through the center of the PHIL tablet in the hole created by the needle.

Temperature data was recorded in 1 s intervals for a total period of 120 s. The initial 30 s were kept for temperature stabilization, and the RF coil was kept on for heating for the subsequent 60 s. The coil was turned off, and temperature was recorded for the final 30 s. PBS was used as a reference for coil heating characterization results. SAR_V (power deposited per unit volume) in the sample was measured using a 1 kW RF coil at 360 kHz and 20 kA/m, and the calculations for PHIL tablet heating (W/m^3)were performed in the same way as previously described.[7, 27, 29, 103] Each sample was tested for three trials at given time points. Samples were tested 1 h, 24 h, 7 d, and 30 d after initial precipitation. When not being heated, samples were placed on an incubating shaker at 37 °C, rotating at 170 RPM for the entirety of the experiment. PBS was replaced every 3 to 4 d by completely emptying the previous solution off with a blunt-tip needle and adding 1 mL of fresh PBS. PBS was also refreshed and the new mass was recorded before every heating test.

Heat Characterization in a Postmortem Tumor Model Heating for 15 min

Mice bearing an MC-38 tumor on the hind limb were humanely euthanized, in accordance with protocols approved by the Institutional Animal Care and Use Committee (IACUC), University of Minnesota.[105] Postmortem tumor-bearing mice were recycled to explore the heating methodology and repeatability to the hyperthermic range for 15 min in tissue,

without additional sacrifice. Mice were kept at 4 °C until day of use, then equilibrated to room temperature. Hind limb tumors were injected with 0.2 mL of PHIL-DMSO-IONPs (0, 4, 8 mg Fe/mL) over a time span of 3 min. The injection point was then flushed with 10 mL of water four times over 20 min to remove all excess DMSO. Temperature monitoring was performed with the help of an infrared camera which recorded the temperature of the tumor system, and the data collection was procured and analyzed using the ThermaCam Researcher Pro Software. Mice were then heated in a 120 kW RF coil operating at 365 kHz with varying magnetic field strength 35.2-18 kA/m for 15 min as shown in Figure S11.

Fe Quantification

Elemental analysis by inductively coupled plasma mass spectroscopy (ICP-MS) on an Agilent 7700 was performed by Australian Laboratory Services (ALS) Global Environmental (Kelson, WA). Prior to ICP analysis, PHIL and PHIL-IONPs tablets were lyophilized in a FreeZone 6L Console Freeze Dry System (Labconco) overnight and crushed into powder. This powder was digested using our previously method.[3, 106] Powder (approximately 20 mg) with 0.2 mL DI water and 0.4 mL concentrated nitric acid were briefly flame sealed in a glass ampule and left at 100 °C overnight. Relaxometry (magnetic relaxometer, MQ60 TD-NMR ANALYZER VT, Bruker Biospin Corporation, MA) was used for further iron quantification following our previously published method.[106] A linear regression of R_1 vs concentration of Fe obtained by ICP of the digested IONPs was determined from a range of concentrations (0, 1, 2, 4 mg Fe/mL powder aliquots) (Figure S5).

RESULTS AND DISCUSSION

Precipitation of IONPs in PHIL

IONPs stay with the precipitate rather than pass into the aqueous solution with DMSO. PHIL-DMSO or PHIL-DMSO-IONPs was pipetted into a bed of water (dark colored liquid, Figure 1, left) so that the initial contacting edge precipitated first, creating a porous shell as the bottom of the tablet (a tan colored solid). After the bottom shell formed, continued addition of PHIL-DMSO or PHIL-DMSO-IONPs backfilled porous areas rather than creating a new edge interface with water. Additional water was added after injection to complete shell formation on the top of the tablet (a tan shell covering a dark liquid center, Figure 1, middle). The cell filter was used to disturb the solution, increasing diffusion of DMSO and water, to create a stable framework precipitation. Once the tablet was formed, water was then refreshed multiple times to hasten diffusion of DMSO from the center of the precipitate outward (tablet visually tan throughout, dark center no longer visible, Figure 1, right). Remaining DMSO was removed by the final steps of submersion in large volumes of fresh DI water overnight (tablet color does not change from Figure 1, right).[95] The IONPs embed in the precipitate as the PHIL-DMSO-IONPs are extruded into water (Figure S2). The color of the surrounding solution does not change, and a slight brown tint can be seen even at very low concentrations (0.1 mg Fe/mL of IONPs in solution, Figure S2). Visually, all solutions surrounding the precipitate, with or without IONPs, are clear in color, indicating IONPs are not leaking out of the PHIL precipitate matrix. IONPs coloring

of solution was not seen in samples left in water for over 6 months (Figure S4, increasing confidence that IONPs are not leaking from tablet.

IONPs embed in PHIL during precipitation and remain embedded rather than following solubility trends and transferring into aqueous solution. Both sIONPs and EMG are very soluble in water, but this work demonstrates that EMG does not transfer from DMSO to water during precipitation and instead is trapped by the PHIL precipitate.[7] sIONPs, which are stable in both solutions, embed in the PHIL precipitate rather than staying in solution.

µCT and MR imaging of PHIL+IONP tablets.

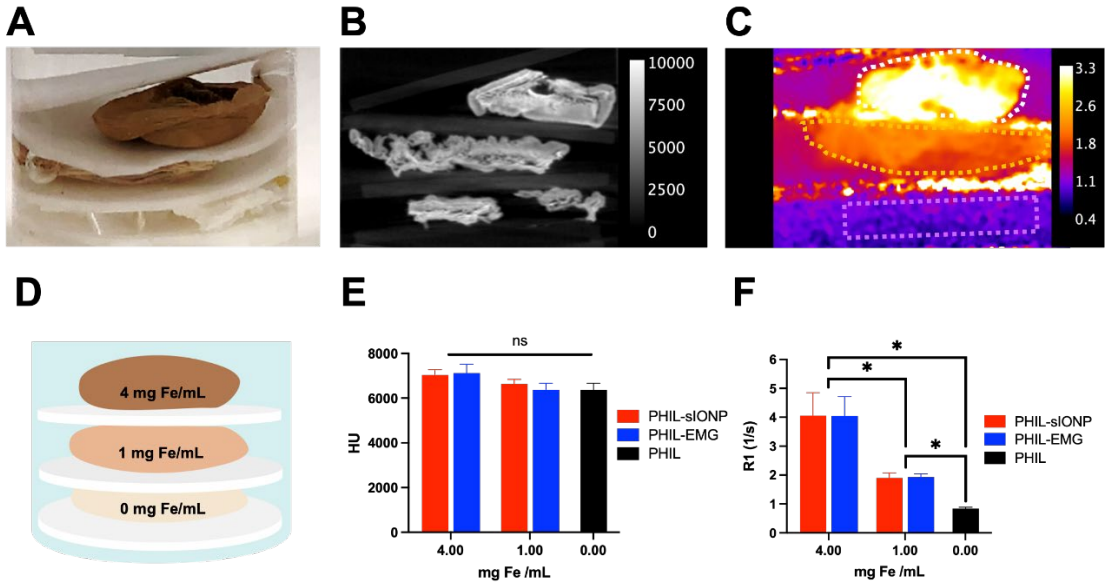

Figure 2.2. Comparison of µCT and MR imaging of PHIL-sIONP Tablets. A. Photos of PHIL-sIONP Tablets in a 2 cm NMR tube. Tablets layered in water with Teflon spacers; 4, 1, and 0 mg Fe/mL. **B.** representative µCT imaging of shown NMR tubes of PHIL precipitate with sIONPs (121 kV, 150 µA, 0.053 mm resolution). PHIL is a high CT contrast agent, IONPs marginally increase contrast, and intensity slightly increases with Fe concentration. **C.** MR imaging of PHIL precipitate with IONPs. This representative image was filtered via a non-local means filter in MATLAB and despeckled in ImageJ to remove noise. PHIL is almost invisible, IONPs add contrast, and intensity increases with Fe concentration (16.4T, MB-SWIFT Look Locker sequence, 0.117 mm resolution). **D.** Diagram of PHIL-IONP tablet

positioning within tube. **E**. Graph of Hounsfield units of IONPs (sIONP and EMG308) coprecipitated in PHIL tablets (ns denotes no significant difference). **F.** Graph of R1 values of IONPs (sIONP and EMG308) coprecipitated in PHIL tablets (asterisk indicates $P < 0.05$ via unpaired two-sample t-test).

Image analysis of the μCT stacks of the PHIL and PHIL-sIONP tablets showed HUs varying from 6370–7130 HU (Figure 2D). While this could locally vary from ~1000–10000 HU in a given tablet, there were no features in the μCT images (Figure 2B) one could use to differentiate between tablets. The samples were not significantly different by one-way ANOVA, which was not surprising given that PHIL is designed to be radiopaque. Although IONPs are also CT active, they do not significantly affect PHIL's overall radiopacity because there is a slightly increasing trend in HUs likely due to an increase in Fe density. In summary, μCT images of PHIL-sIONP did not show significant changes in HU compared to PHIL alone for different Fe concentrations.

Thus, one benefit of PHIL over other embolics, such as Onyx and Squid, is related to its imaging properties on CT. As shown even with the added IONPs, PHIL produces μCT images with high contrast and minimal artifacts (Figure 2C). In contrast, Onyx, while FDA approved and used clinically, produces streak artifacts (low HU and high HU streaks) on CT imaging due to the presence of micronized tantalum. Streak artifacts in general can lead to issues with determining the position of the embolic on CT, which may interfere with detecting hemorrhage during a procedure and could also obscure surrounding tissue features, making detection of tumor recurrence difficult. Squid, similar to Onyx but with smaller tantalum grain size, also suffers from streak artifacts on CT.[57]

Another issue with using Onyx or Squid is the fact that the tantalum in both of these embolics sediments over time. Onyx, with a larger tantalum grain size, requires at least 20 min of shaking prior to use and will settle over the course of a procedure. This leads to a

decrease in radiopacity over time and can make it difficult to determine embolic positioning. Squid has smaller tantalum grain size but still settles over time, though to a lesser degree. The radiopaque iodine in PHIL alone does not have the issue of settling, as it is covalently bound to PHIL itself. The IONPs do not settle or aggregate within the liquid embolic, unlike the tantalum powder.[57] Furthermore, the IONPs do not visibly leech out of the embolic on precipitation (Figures S2 and S4).

In contrast to μCT, MR imaging demonstrates contrast due to IONPs in PHIL. The primary objective of MR imaging was to determine whether the R_1 of a given PHIL tablet containing IONPs could be reliably mapped to a concentration of IONPs within the tablet. IONPs, as well as other magnetic materials in general, tend to drastically increase the R_1 of the surrounding water and therefore make R_1 measurement difficult. Using the MB-SWIFT sequence, images of fast decaying (large R_1) water signals can be obtained. Quantification of R_1 of water molecules in the vicinity of IONPs is made possible by combining the MB-SWIFT with a Look-Locker acquisition scheme, as in our previous study.[100] PHIL-EMG and PHIL-sIONP both showed R_1 values that positively correlated to Fe concentration in the coprecipitate (Figure 2E; EMG R_1 range =1.92-3.69 1/s, sIONP R_1 range = 1.86-3.80 1/s). There is a slight increase in the R_1 of water (R_1~0.33 1/s) when PHIL is present (R_1 = 0.84 +/- 0.09 err 1/s) (Figure 2C); however, pure PHIL is not visually observable on MR imaging through T_1 mapping with Look-Locker MB-SWIFT or MB-SWIFT alone (Figure 2C). Statistical significance was completed by an unpaired two-sample t-test between each set of R_1 values for a given concentration assuming equal variance between sample sets (Figure S6). PHIL alone (0 mg Fe/mL) was statistically

different from PHIL + 4 mg Fe/mL (P = 0.003) and PHIL + 1 mg Fe/mL (P = 0.00008). PHIL + 1 mg Fe/mL was also statistically different from PHIL + 4 mg Fe/mL (P = 0.02).

While the R_1 values correlated well with the IONP concentrations in PHIL-IONP tablets, some changes in pixel locations due to the local magnetic field produced by IONPs, i.e., pileup effects, were observed at increased concentrations of 4 mg Fe/mL (Figure 2C). Pileup may lead to position inaccuracies of ~1–2 mm.

It is also suspected that the IONPs distribute unevenly within the embolic on precipitation. This can be seen in Figure S7. A cross-section of the MR images of 1 mg Fe/mL tablets were taken, and the R1 as a function of distance away from the edge of the tablet was plotted for n = 3 tablets at 1 mg Fe/mL in blocks of ~0.6 mm as a moving average. Tablets at this concentration were specifically chosen because the pileup artifacts from the IONPs on MR imaging were lowest compared to the other two concentrations, so any general trends in IONP distribution could potentially be extracted from these images. While the percent change in R_1 was different between tablets, the overall trend was that R_1 increased from the edge of the tablet to the center, most likely indicating a higher concentration of IONPs in the center.

The MR imaging of PHIL alone also suggests minimal impact on increases in R_1 and therefore T_1 shortening in comparison to Onyx and Squid (Figure 2C). Meanwhile, Onyx appears hypointense (short T_1) on T_1-weighted imaging in MRI. Further shortening of the T_1 on T_1-weighted MRI by Onyx alone could potentially interfere with IONP quantification on MRI. This is because this method of using SWIFT to detect IONPs is primarily T_1-weighted, with decreasing T_1 corresponding to increased IONP concentrations, so a further

decrease in T_1 would potentially limit the upper bound of IONP quantification. While minimal MR imaging studies have been done on Squid, since it is very similar to Onyx, it may still produce variable T_1 hypointensities on MR imaging.[107]

One issue that needs to be addressed, however, is the inhomogeneity of the R_1 values within the same PHIL/IONP tablet obtained from MB-SWIFT imaging. To address this, further studies measuring IONP distribution during precipitation will be needed. IONP concentration measurements on more tube-like structures (as would be injected into a vessel) could also yield more uniform R_1 values and therefore concentrations on imaging. In this case, the solution precipitated immediately on contact with the surrounding water, minimizing inhomogeneities from IONP distribution during PHIL precipitation.

Heating Capability of IONPs in PHIL Precipitate

Here we show that IONPs embedded in PHIL precipitate are able to heat reproducibly and in proportion to the amount of Fe deposited. The heating of PHIL-EMG was lower than PHIL-sIONP for the same concentrations, as shown in Figure 3A. This is likely due to aggregation instability of EMG in PHIL precursor DMSO, as shown in Figure 4. Heating capability (SAR_V), which is related to the rate of heating (see SI SARv calculations), was shown to increase for both IONPs and EMG as Fe concentration increased in PHIL. At 4 mg Fe/mL, sIONPs in PHIL were able to generate more than the minimum therapeutic temperature rise (ΔT) needed for magnetic hyperthermia, i.e., > 8 °C above control (Figure

3B), which in the body would lead to a hyperthermically destructive temperature > 45 °C if applied for > 30 s.[108-109] PHIL-EMG was only able to reach 6.5 °C above initial temperatures under similar conditions.

A temperature elevation of 8 °C above body temperature in a patient would allow a treatment temperature of 45 °C (from 37 °C physiological temperature), which should cause significant cell necrosis when applied for 30 min (equivalent thermal dose to 43 °C for 120 min).[109-113] The time needed for necrosis is decreased exponentially at increased temperatures until 60 °C, at which point necrosis is effectively instantaneous (seconds).[112, 114]

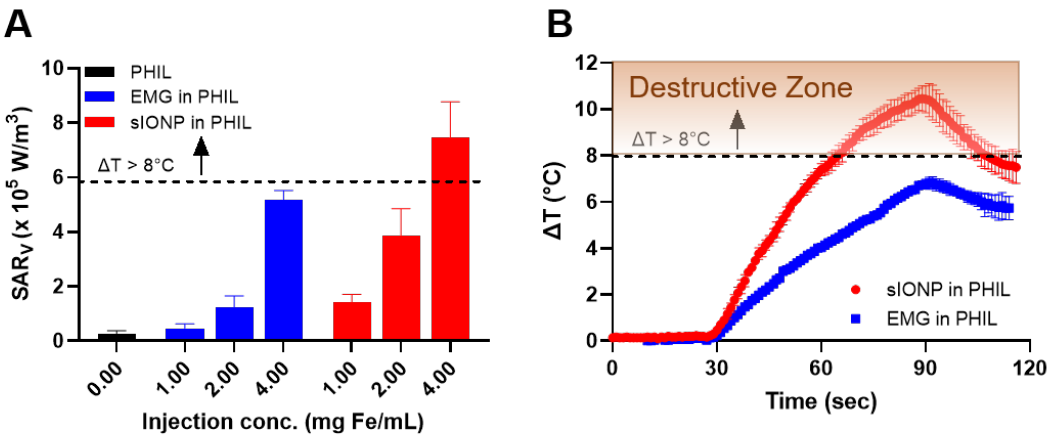

Figure 2.3. Heating of tablets in 15 kW coil at 184 kHz and 65 kA/m. **A.** Effect of varying concentration and type of IONPs on SAR_V. Higher concentration result in higher power deposition per unit volume (SAR_V), and sIONPs have higher SAR_V than EMG308. **B.** Normalized temperature rise for 5 mg Fe/mL of sIONP and EMG308 coprecipitated in PHIL in water. Observation of 8°C temperature rise above the initial temperature (23 °C in vitro for study, and 37 °C in vivo) shows that the sIONPs should be able to potentially achieve temperatures capable of tumor hyperthermia (≥ 45 °C) as opposed to EMG308. Dashed lines in A represent SARv estimated for a ΔT of 8 °C for time span of 60 sec as given by eq. in SI. Dashed line in B represents ΔT threshold of 8 °C, i.e., the minimum therapeutic temperature rise required.

The concentration of IONPs in PHIL plays an important role in the overall heating. For instance, as seen in Figure 3A, both PHIL-EMG and PHIL-sIONP in PHIL have higher

SAR_V (higher heating) with increasing concentrations compared to PHIL alone without any IONPs. Statistical analysis was completed by one-way ANOVA (Figure S8). The SAR_V for PHIL, PHIL-sIONP at 1 mg Fe/mL, PHIL-EMG at 1 mg Fe/mL, or 2 mg Fe/mL are not statistically significant. Further, increasing the concentration of IONPs increases the heating in both EMG and sIONP. As shown in Figure 3A, 4 mg Fe/mL had the highest heating in both IONPs although further increase in heating is possible by increasing the concentration to at least 8 mg Fe/mL, as shown later (Figure 7).

The extent of heating also depends on the stability of the IONPs in solution. sIONPs are EMG coated in silica. sIONPs and EMG have a SAR_{Fe} of approximately 400 W/g Fe in water, and the SAR_{Fe} decreases in cryoprotective solutions such as VS55.[7] Though sIONPs and EMG share similar SAR_{Fe}, the major difference lies in their stability in solution. sIONPs are stable in DMSO, while EMG is not, as can be seen by hydrodynamic diameter measurements in Figure 4. As aggregation of IONPs in solution affects the heating capability of these particles alone, the same is likely to apply within a precipitate.[103] Thus, IONPs more prone to aggregation in solution, like EMG, will likely have lower heating after precipitation. sIONPs coprecipitated with PHIL have better heating than EMG coprecipitated with PHIL at comparable concentrations, even though SAR_{Fe} are identical. As seen in Figure 3A, both EMG308 and sIONP in PHIL have higher SAR_V output (hence higher heating) even at the lowest concentration of 1 mg Fe/mL when compared to PHIL alone without any IONPs. Further, increasing the concentration of IONPs increases the heating for both EMG and sIONPs. As shown in Figure 3A, 4 mg Fe/mL concentration demonstrated the highest heating for both types of IONPs. Further increases in heating are possible by increasing concentration to 8 mg Fe/mL, which is shown in Figure 6.

Colloidal Stability of IONPs Solutions

In order to encapsulate IONPs into PHIL, we needed to demonstrate that IONPs are stable in the PHIL precursor solution, which contains DMSO. To this end, EMG and sIONPs were tested for colloidal stability in DMSO (Figure 4A), PHIL-DMSO (Figure S1B), and PHIL-LV-DMSO (PHIL-low viscosity, a smaller MW of polymer; Figure S1A). The colloidal stability of EMG or sIONPs in DMSO proved to be most important, so the colloidal stability in the other solutions PHIL-DMSO or PHIL-LV-DMSO (Figure S1) followed the same outcome. EMG is not stable in DMSO, whereas sIONPs, silica-coated EMG, are stable in DMSO (seen in Figure 4B). The size of EMG aggregates was initially large, at 450 nm, and slowly dropped to 250 nm after 10 d. As a comparison, the size of EMG particles in water is 45 nm, based on our previous study.[7] EMG likely aggregates instantaneously; the largest aggregates sediment quickly and smaller aggregates follow over several days. The size of EMG in PHIL-DMSO or PHIL-LV-DMSO matched this pattern and started above 500 nm. sIONPs were more stable in DMSO and PHIL-DMSO, both showing stable sIONP size with an average size of 100 nm. This matches well with our previous measurement of a 104 nm effective diameter of sIONPs in water.[7] The size of sIONPs started at 120 nm and dropped to 115 nm in 6 h. After 7 days, the size was still 115 nm. This initial drop was likely due to any large aggregates breaking apart or falling out of solution so that the remaining IONPs are stable. The size in PHIL-DMSO and PHIL-LV-DMSO did not change significantly during the rest of the trial. The stability of sIONPs on visual inspection is higher than that of EMG, as seen in Figure 4B.

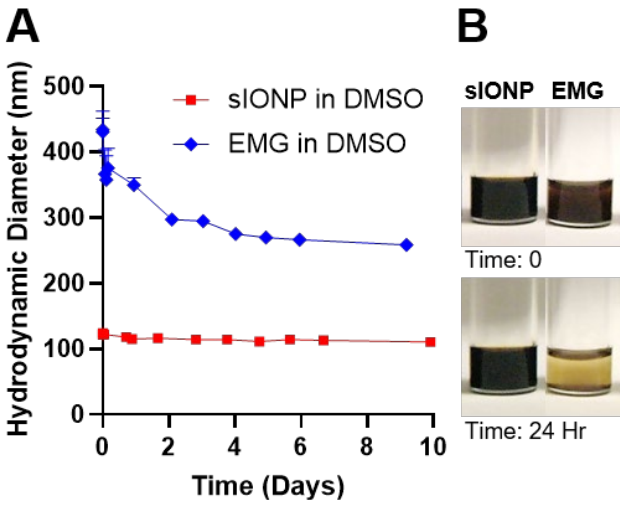

Figure 2.4. DLS determination of stability of IONPs in DMSO. **A.** Hydrodynamic radius of IONPs in DMSO alone and inset of percent of instrument counts. **B.** Photo of solutions at initial time and 24 h. Aggregation and sedimentation (particles falling out of solution) occur with EMG308, but not with sIONPs.

Heating inside Agarose AVM model

To explore the deployment of PHIL-sIONP, we demonstrated its coprecipitation in an in vitro AVM model made from agarose gel from a previous silicone model (Figure S9) and then measured heating under an RF field (Figure 5A, left). Agarose gel is used as a simple physiological model for brain tissue and tumor models and is mostly water, which does not couple to RF fields significantly.[115] A concentration of 3% agarose was used to balance the firmness of higher concentrations of agarose and the flexibility seen at lower concentrations because the compression seals of the setup required mechanical strength under compression and flexibility for the water seal. The agarose concentration is not expected to affect the overall understanding of precipitation or heating.

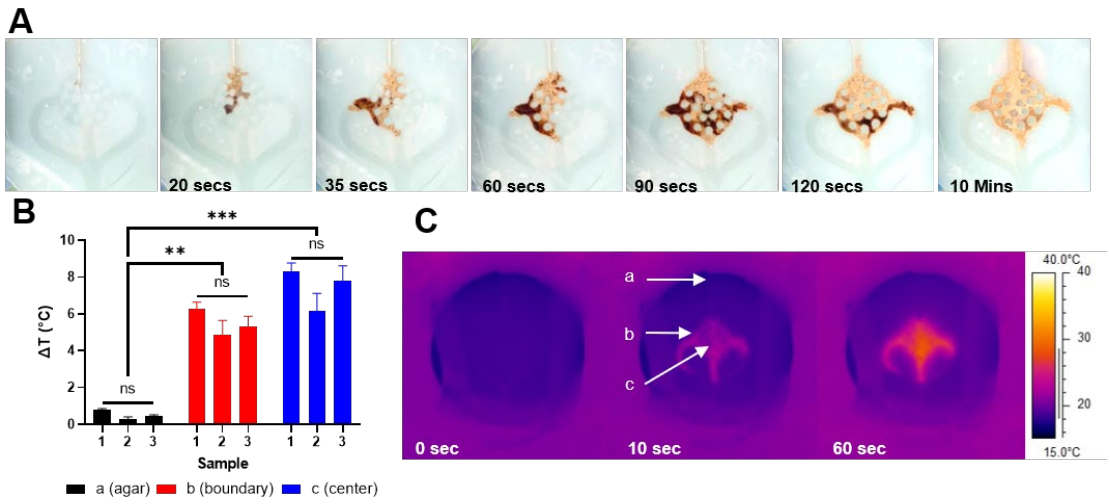

Figure 2.5. Agarose AVM model with PHIL-DMSO-IONP injection and heating. 4 mg Fe/mL PHIL-DMSO-sIONP injection and heating on 120 kW RF coil. **A.** Timelapse photos of PHIL-sIONP co-precipitation in white agarose, AVM model. Needle was placed in the model inlet, and PHIL-DMSO-sIONP was injected into the center of the grid. Tan color is precipitated PHIL-sIONP, and dark areas show PHIL-sIONP still in liquid phase. PHIL-sIONP virtually completely solidified after 20 min continuous flow of water. **B.** Temperature rise from initial after 60 s of heating in RF coil (n = 3 repeats) from three locations on AVM model face: a, agarose furthest from center; b, boundary of vascular bed; c, center of vascular bed. Three separate models with injections. Statistical analysis AVM 3D model heating using one way Anova. ns denotes no significant difference, ** denotes significance of $P < 0.001$, *** denotes significance of $P < 0.0001$. Additional statistical significance exists between center 1 and boundary of 2 and 3, and center of 3 and boundary of 2. **C.** IR temperature image of the shower drain model at room temperature, up to 60 s. Location of interest label for graphs.

The PHIL-sIONP (4 mg Fe/mL) was injected into the center of the model's capillary bed grid and allowed to precipitate for 10 min under a continuous flow of water before heating in an RF coil (Figure 5A). PHIL is a white precipitate without IONPs, whereas the IONPs create a tan tint in the precipitate and make the injection solution a dark brown color. The precipitate edges turn tan instantly on contact with water, as seen at 20 s. The inner areas, where DMSO has not diffused away from the PHIL-IONPs, remain dark brown. As the DMSO diffuses out of the porous precipitate matrix, the polymer deposits, and the area changes to a tan color. The IONPs were not visually seen flowing away from the precipitate at any point in time, as the surrounding solution in the output channels remains completely clear. DMSO and water are both colorless and transparent, but IONPs even at low

concentrations (0.1 mg Fe/mL) in either solution are visible (Figure S2). IONP precipitation with PHIL is not affected by the flow and shear of water through and around the forming precipitate. Once water flushes DMSO away, a porous structure is left, which can be backfilled with additional PHIL-IONP solution, as seen in Figure 5A, from 35 to 60 s. The concentration of IONPs can theoretically be tripled by slowly backfilling space resulting from DMSO diffusion, based on volume percent of PHIL in solution. This has been observed in figure S7, as the center of the tablet has higher concentration then the edges. Pausing the injection to allow DMSO to diffuse away creates space for additional PHIL-IONPs to precipitate upon restarting injection. Backfilling porous areas results in both better embolization and increased concentrations of IONPs for increased heating.

When injected into the agarose AVM model, 4 mg Fe/mL sIONP with PHIL in DMSO was able to heat repeatedly, over three trials. Heating was monitored by an IR camera to compare the temperature increase of agarose to the AVM model grid with PHIL-IONP precipitate. The perimeter of the agarose (location a, Figure 5B) was used as a convective heating control. The boundary edge of the grid (location b) was compared to the center of the grid (location c) to understand the uniformity of heating throughout the precipitate. Each sample has slightly different heating because the three embolic injections precipitate slightly differently. Areas with precipitates were seen to have significant heating over the agarose border, which did not increase significantly (Figure 5C). Statistical analysis was done by one-way ANOVA, as in Figure S10. The center of the model increased in temperature 6–8 °C and the boundary of the grid reached 75% higher in the 60 s tested (Figure S10). Temperature increase was relatively consistent over each of the three trials

on individual samples, suggesting PHIL precipitate was not being degraded or changed by increased temperature or heating gradients.

Heating Stability under Physiological Conditions

To better understand the stability of IONPs in a physiological setting, heating was tested on 8 mg Fe/mL of IONPs in PHIL at multiple time points over 1 month (Figure 6) as well as SEM before and after testing (Figure S11). To simulate physiological conditions, a PBS buffer was used to mimic the pH and osmolality of the human body. An incubating shaker was used to keep the temperature at 37 °C and moving, similar to blood flow. This test is important because IONPs in solution have been known to degrade or aggregate over time in increased temperature, protein, or salt in the buffer.[29, 56] Nevertheless, IONPs in PHIL were consistently heated with a SAR_V ~15×10^5 W/m^3 on each test day, suggesting repeated heating, shaking, PBS buffer, and time did not alter the reproducibility of heating.

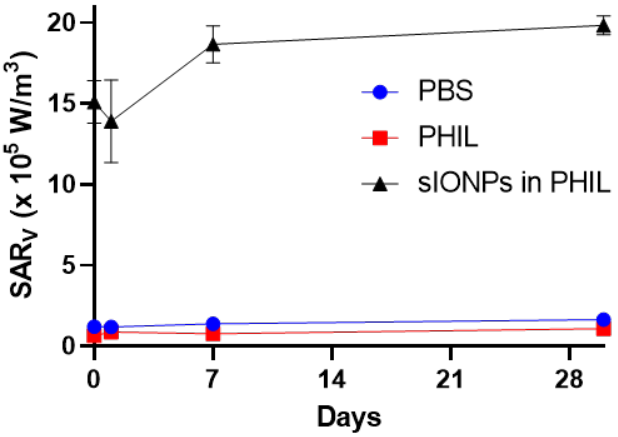

Figure 2.6. Repeatable heating of PHIL-IONP precipitate over 1 month. Stability of heating in physiological conditions of three solutions on an incubating shake at 37 °C and 170 RPM for 30 days: Black line: 8 mg Fe/mL of sIONPs in PHIL in 1 mL PBS, Red line: PHIL W/O IONPs in 1 mL of PBS, Blue line: PBS alone. Heating time points taken on 1 kW Hotshot inductive heating systems with 2.75-turn, water-cooled copper coil (Ameritherm Inc., Scottsville, NY), 360 kHz and 20 kA/m. Heating was consistent

over 1 month. Asterisk denotes slight increase over time that is likely due to inward collapse of precipitate, increasing local concentration of Fe around the fiber optic probe.

The slight initial dip of the SAR_V (W/m^3) was likely due to an initial shift in the location of the sIONP PHIL embolic mass away from the fiber optic insertion spot, or residual DMSO diffusing out of the precipitate and being replaced with PBS buffer. This second possibility would occur if there were significant residual DMSO, given that its heat capacity of ~1.97 (J/g K) is less than ½ that of water's 4.18 (J/g K), which would imply that the temperature rise in DMSO would be larger than water under similar conditions. Similar to the above, we attribute the increase of heating between day 1 and 7 to the increase of PHIL at the center of the tube, closer to the fluoroptic probe. The fluoroptic probes were removed during shaking and incubation periods, leaving an unsupported hole. The shaking at 170 RPM over the first week led to the PHIL super structure shifting inwards. Without secondary support, such as capillary beds, PHIL is freely moving inside the tube. Over time, slight fractures formed, resulting in PHIL pieces shifting into the hole created for the fiber optic. For the heating test on day 7, the fiber optic was replaced into the same position, now overlapping with precipitate. This increase in PHIL and IONP density around the fiber optic resulted in an increase in temperature rise at that spot.

Importantly, IONPs in PHIL precipitate did not show decreased heating capability over time or after repeated testing. Additionally, the structure of PHIL as observed by SEM was not affected, Figure S11C and D. Thus, in principle, a single PHIL-IONP injection could be used to heat a tumor multiple times over an extended period, allowing time (weeks to months) to monitor tumor reduction, remission, or relapse. Although other IONPs in embolic type agents such as hydrogels have been tested over 2 weeks, their heating saw

significant decreases after 4 d and complete loss after 2 weeks, presumably due to IONP attrition from the gel.[55-56]

Heating Capabilities in Tissue

To assess the ability of PHIL-IONP to heat tumors, the embolic was injected into mice with hind limb tumors postmortem and then heated repeatedly within an RF field. Ultimately, living animals will have blood flow surrounding the embolic site, which may affect heating from IONPs and will need to be studied further. In this proof of principle study, we elected to use postmortem animals with no blood flow to understand the capabilities of our 120 kW coil to heat for 15 min and customize the heating based on the concentration of IONPs in PHIL and magnetic field strength as measured with an IR camera (Figure 7A). Injections of 0.2 mL of 10 mg Fe/mL IONPs in PHIL DMSO were used, as this volume has been commonly used with mice.[116] Several initial tests were done at 0, 4, and 8 mg Fe/mL sIONPs in PHIL and at various field strengths (Figure S12). Coil settings of 33.2 kA/m (94% coil power) for 0–5 minutes and 28.5 kA/m (80% coil power) for 5–15 min were chosen for the maximum stable field strength and then lowered to the field strength to maintain a stable temperature increase (Figure 7C). Notably, for larger scale treatments, any amount of non-specific heating (eddy heating) in healthy tissue could be avoided by lowering the field strength and/or frequency and increasing the IONP concentration to maintain the required heating (targeted therapeutic temperature). An average of 17 °C increase was seen after 5 min (Figure S12B), which, assuming minimal blood flow heat loss, would translate to 54 °C in vivo, well into the therapeutic range for

treatment. Heating reached therapeutic increases, 8 °C, after approximately 90 s, and remained above this level for the entirety of the coil operation and 5 min after the coil was turned off.

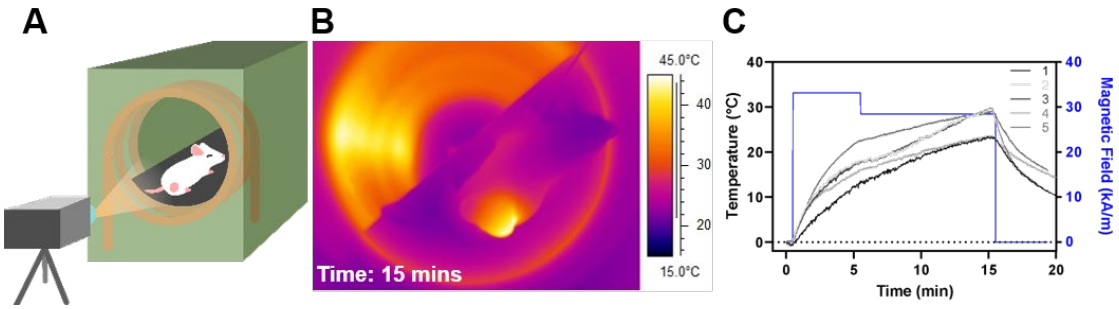

Figure 2.7. Heating of postmortem mice tumors with PHIL-IONPS. Post mortem mice hindlimb tumor injected into center of hindlimb tumor. A. Illustration of the heating setup inside the RF coil. B. IR image of postmortem mouse heating at 15 min for 8 mg Fe/mL injection case. C. Temperature curves of mice injected with 0.2 mL of 8 mg Fe/mL sIONPs in PHIL DMSO solution in coil at 365 kHz and 33.2 kA /m (94% coil power) for 0–5 min, 28.5 kA /m (80% coil power) for 5–15 min, and coil off after 15 min. Blue line is magnetic field strengths for 81 mg Fe/mL heating trials. Each of the five grey lines represents an individual heating trial on separate mice.

by an IR camera. The temperature increase was found to be localized only to the injection site in the tumor, as seen in Figure 7B. This suggests that PHIL and therefore heat is localized to the tumor and likely will not produce thermal damage to non-target tissues or organs. It should be noted that there is a heating gradient similar to the agarose AVM model, which under sufficiently long heating of the tumor can exceed 8 °C at the tumor edge. Further refinement of sIONP PHIL heating can be tuned with concentration changes and visualization upon injection through fluoroscopy.

CONCLUSION

These results demonstrate that RF heating of the PHIL-sIONP embolic is a potentially promising method of treating vascularized tumors. IONPs were shown to coprecipitate with PHIL in a 3D AVM agarose model. This was heated to therapeutic temperatures in a

RF coil and could be performed multiple times with reproducible heating over 1 month in PBS at 37 °C. Further, we confirmed the capability of injecting tumors in mice with PHIL-sIONP and heating the embolized tumors in an RF coil to therapeutic temperatures. This embolic is imageable on both μCT (primarily PHIL contrast) and MRI using MB-SWIFT (primarily IONP contrast) potentially allowing for monitoring of embolic position and IONP concentration during and after embolization. It was demonstrated that despite the ability to encapsulate both EMG (IONP core, Ferrotec) and silica coated EMG in PHIL only the sIONPs are colloidally stable in DMSO and PHIL. We also showed that the addition of IONPs to PHIL does not lead to premature precipitation of PHIL. Future studies should continue these experiments on live tumor-bearing animals to show the impact on tumor growth for clinical relevance as well as to show the effect of blood flow on the stability of PHIL-sIONP precipitates within tumor beds. Further optimization of RF field strength, IONP concentration, and PHIL deployment should also be characterized and refined.

SUPPORTING INFORMATION

Representative Calculations for SAR_V (or Power) deposition:

The total power deposited (P, Watts) into an embolic tablet can be estimated as below:

$$P = m' * C_P' * \frac{\Delta T}{\Delta t}$$

m' (kg): & C_P' (J/kg.K): specific heat at constant pressure for combined PHIL + water tablet

C_P': Combined specific heat of water + PHIL (tablet) is estimated by weighted mass average-

$$C_P{}' = (m_{water} * C_{P_{water}} + m_{PHIL} * C_{P_{PHIL}})/(m_{water} + m_{PHIL})$$

Further, we assumed the SAR_V is the power deposited per unit volume (W/m^3) as calculated by time rise method in literature: [104, 117]

$$SAR_V = \frac{P}{V} = \rho' * C_P{}' * \frac{\Delta T}{\Delta t}$$

ρ' (kg/m^3): density of tablet is a combination of PHIL and water, with the vast majority of it being water. Thus the density of water (1000 kg/m^3) can be used as an approximation for the density of the tablet.

To asses SAR_V by the time rise method, the $\Delta T/\Delta t$ slope of temperature curve over initial 30 seconds is used. For instance, in the case of sIONP trial 5C at 5mgFe/mL, slope of heating curve was observed to be 0.228 K/s (average of 3 repeats). C_P of water = 4180 J/kgK and C_P of PHIL = 1400 J/kgK

$$C_P' = \frac{7.36 * 4.18 + 0.339 * 1.4}{0.339 + 7.36}$$

$$C_P' = 4057\ [\frac{J}{kgK}]$$

$$SAR_V = 1000\ \left[\frac{kg}{m^3}\right] * 4057\left[\frac{J}{kgK}\right] * 0.228\left[\frac{K}{s}\right]$$

$$SAR_V = 9.25 * 10^5\ [\frac{W}{m^3}]$$

Table 2.1. Sample formulation of IONPs in PHIL.

IONP	Conc mg Fe /mL	Mass (g)			PHIL wt/vol%
		IONP	PHIL	DMSO	
None	0	0	3	9	31%
sIONP	1	0.204	3	8.96	
	2	0.407		8.91	
	4	0.814		8.83	
EMG308	1	0.02	3	9	
	2	0.041		8.99	
	4	0.081		8.98	

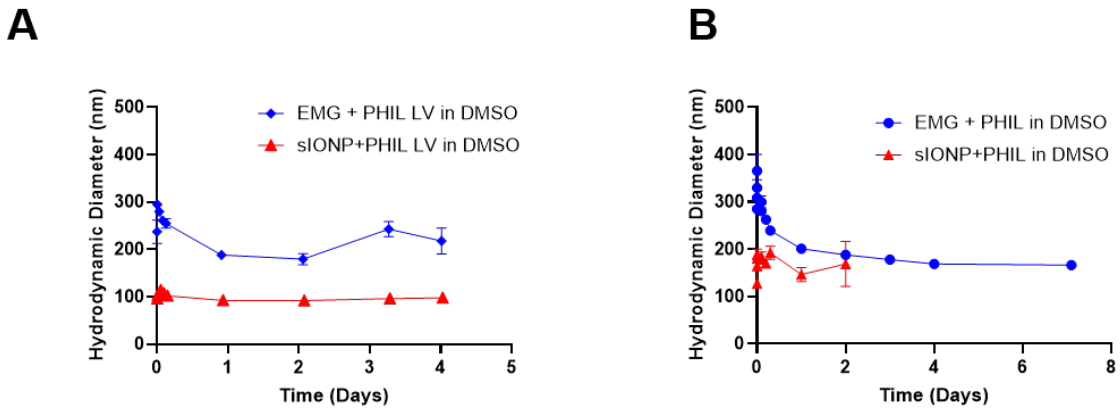

Figure S2.1. DLS determination of stability of IONPs in PHIL DMSO solutions. **A.** Hydrodynamic radius of IONPs with PHIL-LV in DMSO. **B.** Hydrodynamic radius of IONPs with PHIL in DMSO

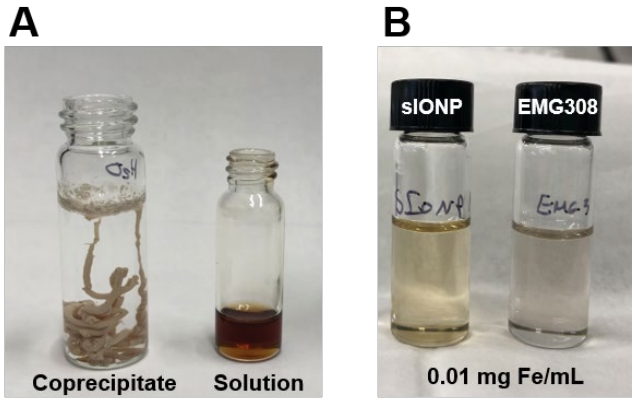

Figure S2.2. Visual evidence of IONPs in PHIL precipitate vs solution. **A.** Photos of right: 1 mg Fe/mL sIONP with PHIL dissolved in DMSO solution, left: solution pipetted into water resulting in precipitate as DMSO exchanges with water. Solution surrounding PHIL precipitate remains clear after precipitation event, indicating IONPs are not leaking into H_2O. **B.** Low concentration of IONPs in DMSO solution.

Figure S2.3. PHIL Tablet formation around fiber optic.

Figure S2.4. PHIL-IONP coprecipitates in water after 6 months. PHIL without IONPs is white (■), increasing concentration of sIONP results in darker tan color (▲), increasing concentration of EMG308 results in darker grey color (*). Fragmentation of precipitate is due to sample transport knocking tablets against glass. Tablets with more sIONPs are less fragmented. Solution remains clear indicating IONPs are not leaking.

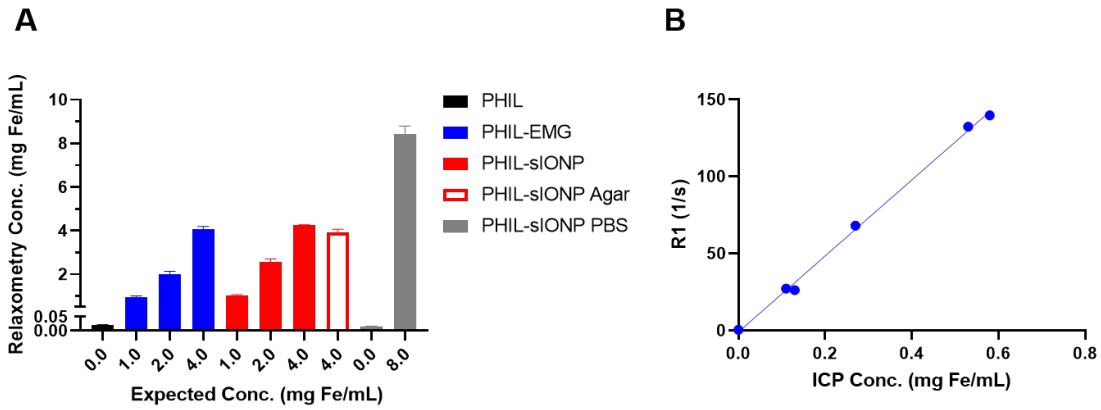

Figure S2.5. PHIL-IONP Fe quantification using relaxometry. Lyophilized samples of PHIL+ IONP precipitate were crushed up and digested for relaxometry and ICP Fe quantification **A.** Concentration of injections by R1 of digested powered, normalized to amount of powdered sample digested, 15-30 mg powder per sample. **B.** Linear regression of ICP reported Fe concentration to R1 values.
One may note that the R1 values obtained via MR Imaging are noticeably lower than expected as IONPs can increase R1 to ~40 1/s or so on imaging.[118] This effect is most likely a result of the PHIL around the IONPs limiting the amount of free water close to the IONPs compared to IONPs dispersed in water or in agar.

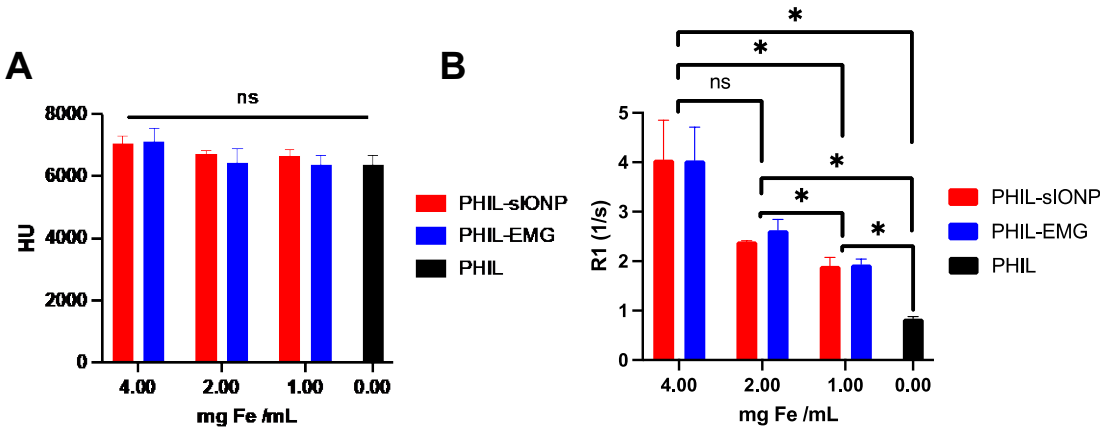

Figure S2.6. Statistical analysis of µCT and MR imaging analysis of PHIL tablets A. µCT and **B.** MR imaging using two-sample unpaired t-test (includes 2 mg Fe/mL PHIL-IONP tablets). ns denotes no significant difference, * denotes significance of $P<0.05$

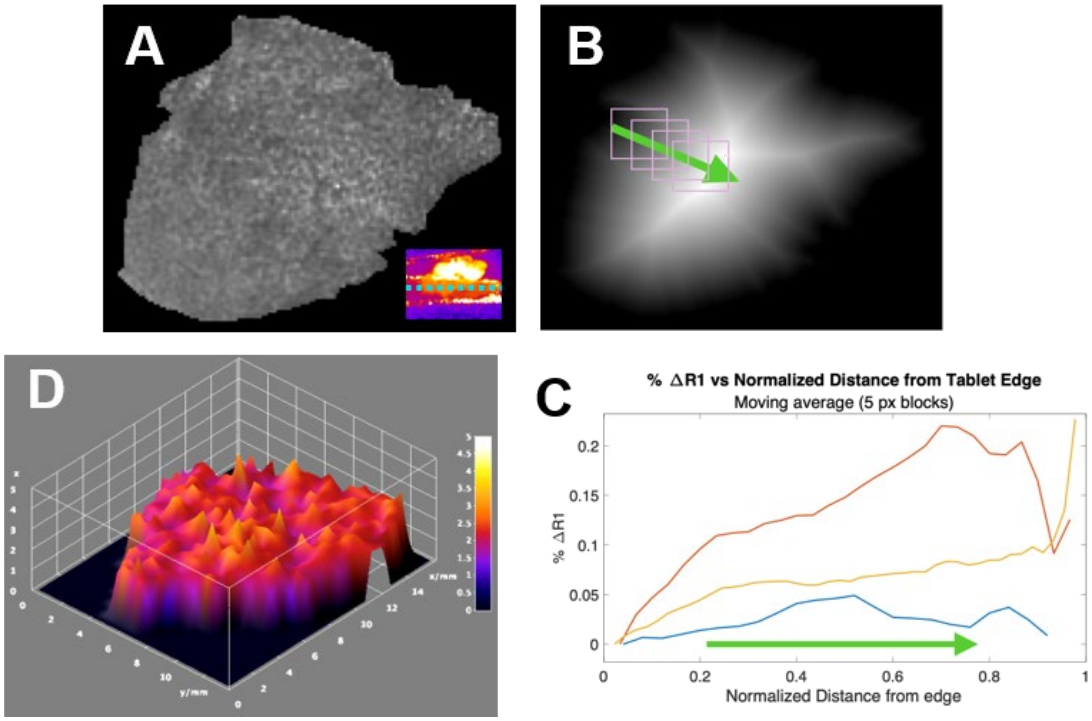

Figure S2.7. Mapping MR R1 trends across PHIL-sIONP tablets. A. Manually outlined cross section of the representative PHIL-sIONP tablet shown in Fig. 2C at 1 mg Fe/mL. **B.** Distance transform of A after thresholding and representation of R1 sampling. **C.** Plot of percent change in mean R1 from the mean R1 at the tablet edge (% ΔR1) as a function of normalized distance from the tablet edge for MR images of 1 mg Fe/mL tablets. **D**. 3D surface plot of R1 across section of tablet in A.

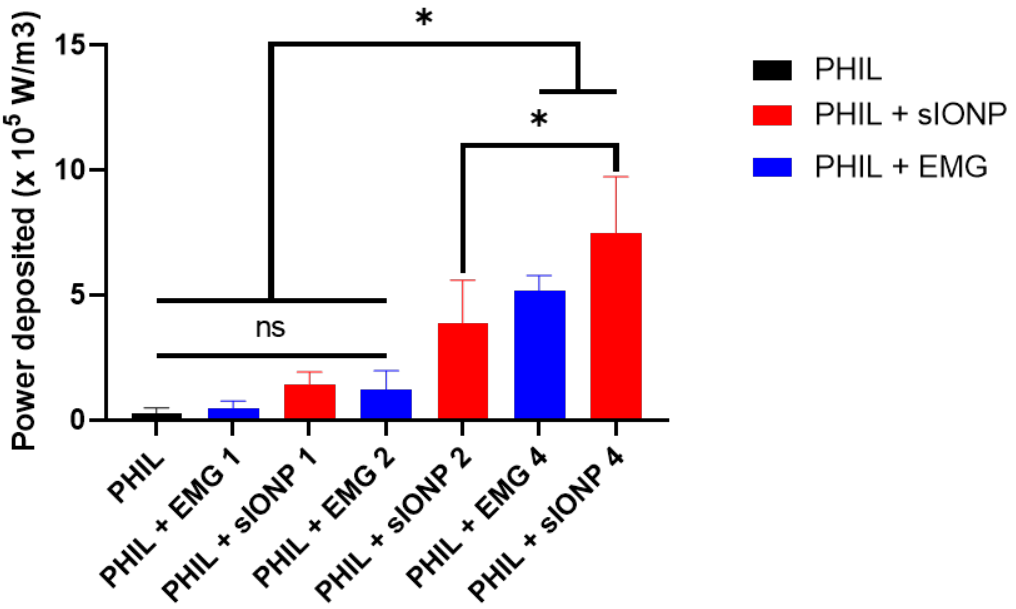

Figure S2.8. Statistical analysis of tablet heating using one-way ANOVA. Ns denotes no significant difference, * denotes significance of P<0.01

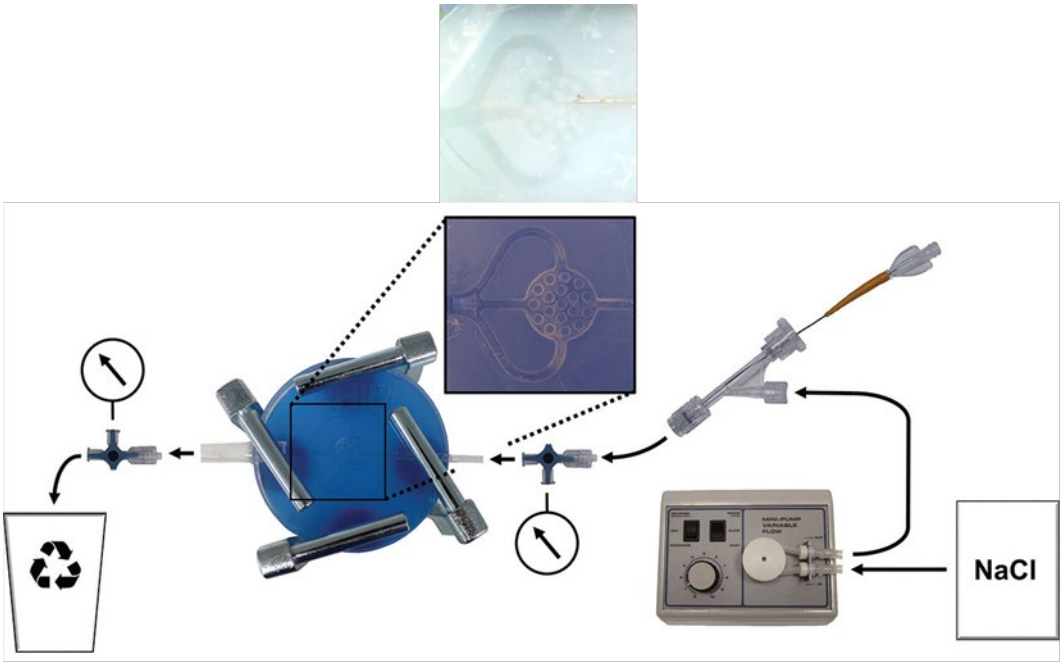

Figure S2.9. Microvention 3D AVM model and injection system. Herein, agarose 3D AVM replaced silicone model. Reproduced from Vollherbst, D. F, Et.al. with permission from American Society of Neuroradiology.[95]

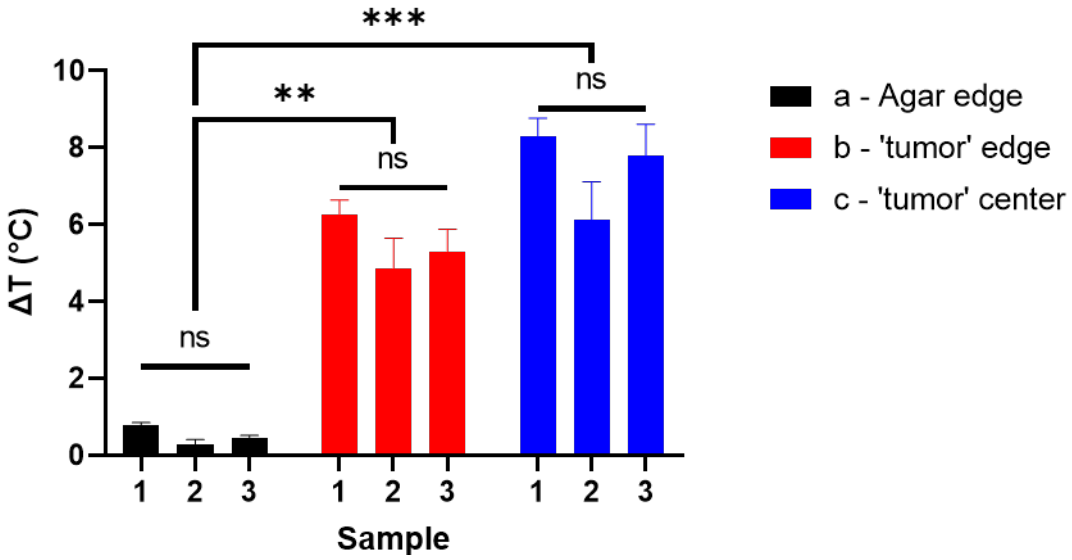

Figure S2.10. Statistical analysis of Figure 6: AVM 3D model heating of 8 mg/mL sIONPs in PHIL using one-way ANOVA. Location on agarose model is denoted by letter and description. Ns denotes no significant difference, ** denotes significance of P<0.001, *** denotes significance of P<0.0001 Additional statistical significance Between center 1 and edge of 2 and 3, and center of 3 and edge of 2.

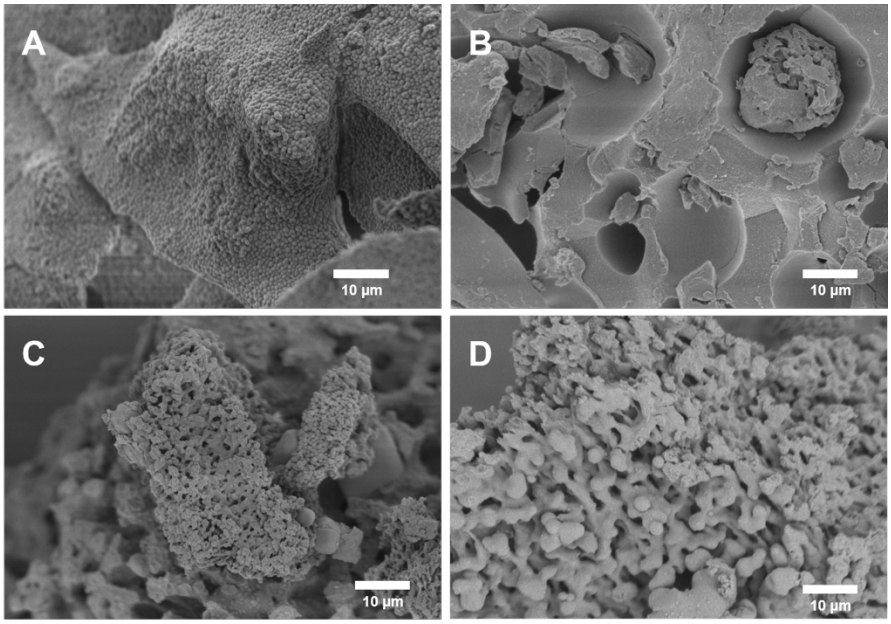

Figure S2.11. SEM imaging of sIONP and PHIL samples. **A.** sIONPs after synthesis. **B.** PHIL polymer **C.** PHIL-IONPs precipitated in PBS before incubating on shaker for 30 days. **D.** PHIL-IONPs precipitated in PBS after incubating on shaker for 30 days.

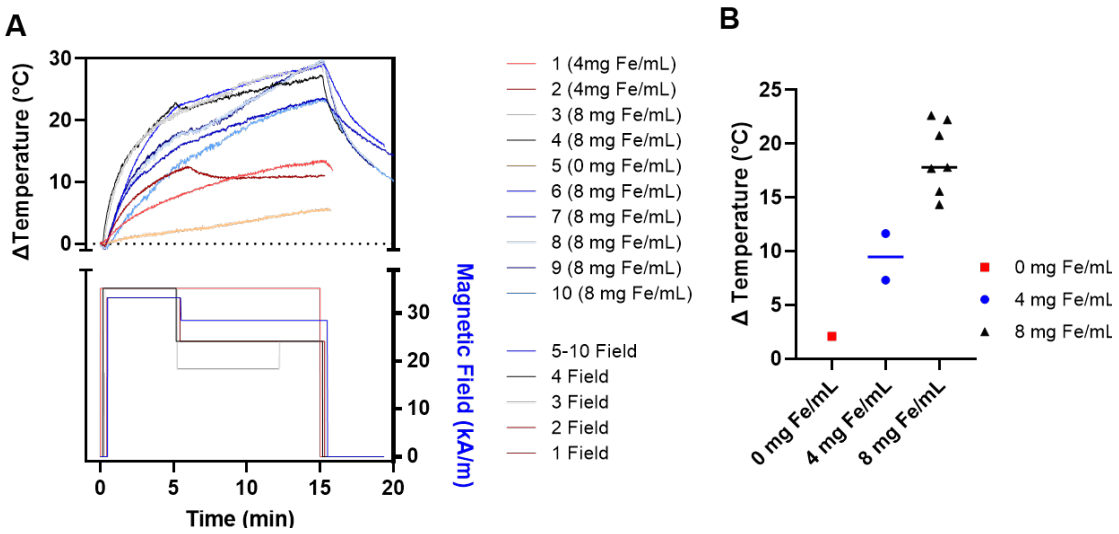

Figure S2.12. 15 minute heating of postmortem tumors in 120 kW coil at various fields. **A. TOP.** Temperature curves of mice injected with 0.2 mL of various concentrations of sIONPs in PHIL DMSO solution in coil at 365 kHz and various field strengths. Mouse number with concentration. **BOTTOM.** Repeat of magnetic field strengths of heating trials from Figure 8 for visualization. **B.** Temperature increase in 0-5 minutes at various concentrations of IONPs in 0.2 mL PHIL DMSO injections, red: 0 mg Fe/mL, Blue: 4 mg Fe/mL, Black 8 mg Fe/mL. Mouse number to field for legend.

Chapter 3: Phosphonate Coating of Iron Oxide Nanoparticles for Organ Cryopreservation

This chapter describes the development of phosphonate coating of iron oxide nanoparticles for nanowarming applications. This work led to the successful cryopreservation and nanowarming of human dermal fibroblast cells. Most of the work in this chapter is taken from the following peer reviewed publication and reproduced here with the permission of the journal publisher:

Pasek-Allen, J. L.; Wilharm, R. K.; Gao, Z.; Pierre, V. C.; Bischof, J. C., (2022)**,** Phosphonate Coating of Commercial Iron Oxide Nanoparticles for Nanowarming Cryopreserved Samples. *Journal of Materials Chemistry B*.

DOI: 10.1039/D1TB02483C

SUMMARY

New preservation technologies may allow for organ banking similar to blood and biomaterial banking approaches. Using cryoprotective agents (CPAs), aqueous solutions with organic components such as DMSO, propylene glycol, and added salts and sugars, organs can be used to vitrify and store organs at 140 C. When needed, these organs can be rewarmed in a rapid and uniform manner if CPAs are supplemented with iron oxide nanoparticles (IONPs) in an applied radiofrequency field. Speed and uniformity of warming are both IONP concentration and CPA suspension dependent. Here we present a coating method of small molecule phosphonate linker (PLink) and biocompatible polymer (i.e. polyethylene glycol PEG) that tunes stability and increases the maximum allowable concentration of IONPs in CPA suspension. PLink contains a phosphonate 'anchor' for high irreversible binding to iron oxide and a carboxylic acid 'handle' for ligand attachment. PLink-PEG removes and replaces the initial coating layer of commercially available IONPs (EMG1200 (hydrophobic) and EMG308 (hydrophilic) Ferrotec, Inc., increasing colloidal stability and decreasing aggregation in both water and CPAs, (verified with dynamic light scattering) from minutes (uncoated) to up to 6 days. Heating properties of EMG1200, specific absorption rate (SAR), measured using an applied field of 360 kHz and 20 kA/m, increased from 20 to 180 W per g Fe with increasing PLink-PEG5000. PEG replacing the initially hydrophobic coating decreased aggregation in water and CPA, consistent with earlier studies on heating performance. Furthermore, although the size is minimized at 0.20 mol PEG per g Fe, heating is not maximized until concentrations above 0.43 mol PEG per g Fe on EMG1200. SAR on hydrophilic EMG308 was preserved at 400 W per g Fe regardless of the amount of PLink added to the core. Herein concentrations of IONP in

VS55 (common CPA) significantly above our previous capabilities, sIONP at 10 mg Fe per mL, was reached, 25 mg Fe per mL of 308-PEG5000 and 60 mg Fe per mL of 1200-PEG5000, approaching stock EMG308 in water, 60 mg Fe per mL. Furthermore, at these concentrations cryopreserved Human dermal fibroblast cells were successfully nanowarmed (at applied fields described above), with higher viability as compared to convective rewarming in a water bath and heating rate close to 200 1C min_1, 2.5 times faster than our current system. Using PLink as the coating method allowed for higher concentrations of IONPs to be successfully suspended in CPA without affecting the heating ability. Additionally, the model ligand, PEG, allowed for increased stability over time in nanowarming experiments.

INTRODUCTION

The inability to preserve donated organs for more than a few hours contributes to organ shortages, poor organ matching (i.e. harsh immune suppression and graft rejection), and limitations to the length and quality of life for organ transplant recipients.[58, 66, 69] Each year approximately 30,000 patients are added to the kidney transplant list, but only about 17,000 kidney transplants take place each year.[119] In 2015 of the almost 100,000 patients on the kidney transplant waiting list, close to 5,000 people died and an additional 4,154 were removed as they were too sick for transplant.[119] Yet every year, thousands of potentially transplantable kidneys are discarded when their preservation limits are exceeded.[58, 60] Using carefully optimized cryoprotective agents (CPAs) and perfusion protocols, researchers have successfully cryopreserved multiple tissues and animal organs including kidneys in an ice-free vitrified, glassy or amorphous, state, allowing for indefinite

storage.[26, 73-74, 76-77, 120] However, these advances require fast and uniform warming to avoid ice crystallization and cracking that reduce viability of tissues or organs on warming. Diminishing ice crystal formation on rewarming can be achieved by increased rate of warming or increasing the concentration of CPAs which retard ice formation but can increase toxicity. A solution to this problem is to use "nanowarming", a new technology, based on radiofrequency excited iron oxide nanoparticles (IONPs) deployed within CPAs to rewarm vitrified biosamples.[27] Using this approach, the higher the concentration of IONPs allows for faster rates of heating, and therefore lower concentration of CPA needed to avoid ice damage.

Successful translation of nanowarming technology requires IONPs with scalable synthesis (>1 g/batch), that are biocompatible, produce high heating, and disperse evenly throughout a CPA.[7, 27] Bare IONPs can be toxic to cells and tend to aggregate in CPAs, coatings are required for biocompatibility and even dispersion.[34, 41, 78-79] CPAs are aqueous solutions with components of salts, sugars and organic solvents. The organic components of CPAs decrease the Van der Waals forces of adsorbed ligands, causing loss of coating and IONPs to aggregate or sediment in solution.[32, 121] Salt solutions, with high ionic strength reduce the impact of electrostatic forces separating nanoparticles, resulting in aggregation.[122] While multiple methods to coat IONPs have been reported (silica, starch, dextran and adsorbed PEG), a simple, scalable, cost-effective coating method that maintains high heating and imaging capacity of IONPs in CPAs is still needed. We have shown that silica coated IONPs, using a small PEG layer, sIONPs, can be used for nanowarming in small animal models and in vitro testing, but at more than $2/mg Fe, they are expensive and labor intensive for clinical applications.[27, 33] To advance nanowarming applications the cost of

IONP formulation must be accessible for large scale organs. For instance, when planning on perfusing IONP into a human scale organ, grams of coated colloidally stable IONPs are needed on a daily basis. Human scale (porcine, primate) kidneys require 2.2 g Fe of fresh IONPs at 10 mg Fe/mL for perfusion and the surrounding solution.[5] Hundreds of human scale organs will be needed to be tested for method preparations, uniformity of perfusion, cryopreservation and nanowarming, and toxicity.

The drawback with the silica coating of the sIONP is the thickness of silica shell, 18nm, which increases the volume per nanoparticle thereby decreases the maximum concentration of IONP cores, and therefore heating capabilities in CPA.

Based on our prior studies with iron oxide nanoparticles contrast agents for magnetic resonance imaging, we hypothesize that a phosphonate-based linker will allow for large scale, anchoring of ligands directly onto iron oxide cores, with- out a thick silica shell to make a large quantity of cheap IONPs for biomedical applications.[106, 121 32, 123-124] Developing this coating method would lead the way to an affordable IONP for organ nanowarming and other applications that require high concentrations of IONPs in CPA for faster heating.

We have synthesized and characterized a phosphonate linker, called PLink, to functionalize two commercially available iron oxide nanoparticle (IONP) cores. IONPs were coated with PEG as a model compound, to determine PLink's effect on core heating and NP stability in water and CPA. Three different molecular weights (MW) of PEG were investigated, 500, 2000 and 5000 Da based on our current sIONP coating method, and commonly used PEG MW to prevent cellular uptake.[7, 78] Ligand exchange was determined by thermal gravimetric analysis (TGA) and High resolution magic angle spin (HRMAS) nuclear

magnetic resonance (NMR) to show removal of initial ligand and replacement with PEG. We studied the surface coverage of IONPs through stability in water, and CPA. The effect of linkage on heating was tested to determine feasibility of phosphonate coating. Finally, we tested the cell viability of nanowarmed cells using our best coating method on both IONPs.

EXPERIMENTAL

Materials and Methods

Unless otherwise noted, starting materials were obtained from commercial suppliers and used without further purification. IONPs, EMG308 and EMG1200, were purchased from Ferrotec inc. Pd-10 column G25 sephadex media were purchased from Global Life Sciences solutions USA LLC. Neodymium Magnetic Blocks 2" x 1" x 1/2" N52 and 4" x 1" x 1/2" Bar Magnets, purchased from CMS Magnetics.

General characterization

1H, 13C, and 31P NMR spectra were recorded on a Bruker Avance III HD nanobay AX-400 at 400, 101 or 162 MHz respectively; with chemical shifts referenced to appropriate internal standards. Data for 1H, 13C, and 31P NMR are recorded as follows: chemical shift (d, ppm), multiplicity (s, singlet; d, doublet; t, triplet; m, multiplet) integration, coupling constant. High resolution (HR) electrospray ionization time-of-flight mass spectrometry (ESI/TOF-MS) were recorded on a Bruker BoTOF I at the LeClaire-DOW instrumentation

facility of the Department of Chemistry of the University of Minnesota. (MS data was collected by Randall Wilharm) FTIR spectra were recorded on a ThermoFisher Scientific Nicolet iS FT-IR spectrometer. (IR data was collected by Randall Wilharm) TEM images were collected on a FEI Tecnai T12 at 120 kV. (TEM images data were collected by Zhe Gao) Nanoparticle size was determined by dynamic light scattering (DLS), measurements on a Brookhaven Zeta PALS instrument (Brookhaven Instruments Corporation) with a 635 nm diode laser at 15 mW of power. Stability of colloidal suspension was determined by DLS time points at the same concentration, taken several times in the first 24 hours and then on daily or weekly intervals up to 4 weeks. Measurements were stopped when visual precipitation occurred. Stability was tested in water, and CPA VS55 with Euro Collins carrier solution, table S1.[125] A thermogravimetric analyser (TGA, Model 951, TA Instruments, New Castle, DE) was connected to a thermal analysis operating system (Thermal Analyst 2000, TA Instruments). Approximately 5–10 mg of the sample, in an open aluminium pan, was heated in the TGA from room temperature to 300°C at 10°C/min under nitrogen purge. Data was collected from lyophilized IONPs with the following method; remove residual water: temperature increase to 100 °C at 20 °C/min, hold for 10 minutes, increase temperature to 800 °C at 10 °C/min.

Elemental analysis by inductively coupled plasma optical emission spectroscopy (ICP-OES) on a Perkin–Elmer Optima 3000V was performed by the Soil Testing and Research Analytical Laboratory of the University of Minnesota, Twin-Cities. Prior to analysis by ICP, IONPs were digested by a 0.2mL of stock IONP solution, 0.4mL concentrated nitric acid in a flame sealed glass ampule at 100 °C overnight. Relaxometry (magnetic relaxometer, MQ60 TD-NMR ANALYZER VT (Bruker Biospin Corporation, MA) was

used for further iron quantification following our previously published method.[106] A linear regression of 1/T1 vs ICP Fe of digested IONPs was the determined from a range of concentrations (0.1, 0.6, 1, 3, 6, 12 mg Fe/mL)

Synthesis of phosphonate linker of PEG to IONP

The following compounds were synthesized based on the scheme in Figure 1, based on a similar phosphonate linkage method from previous co-workers research.[126]

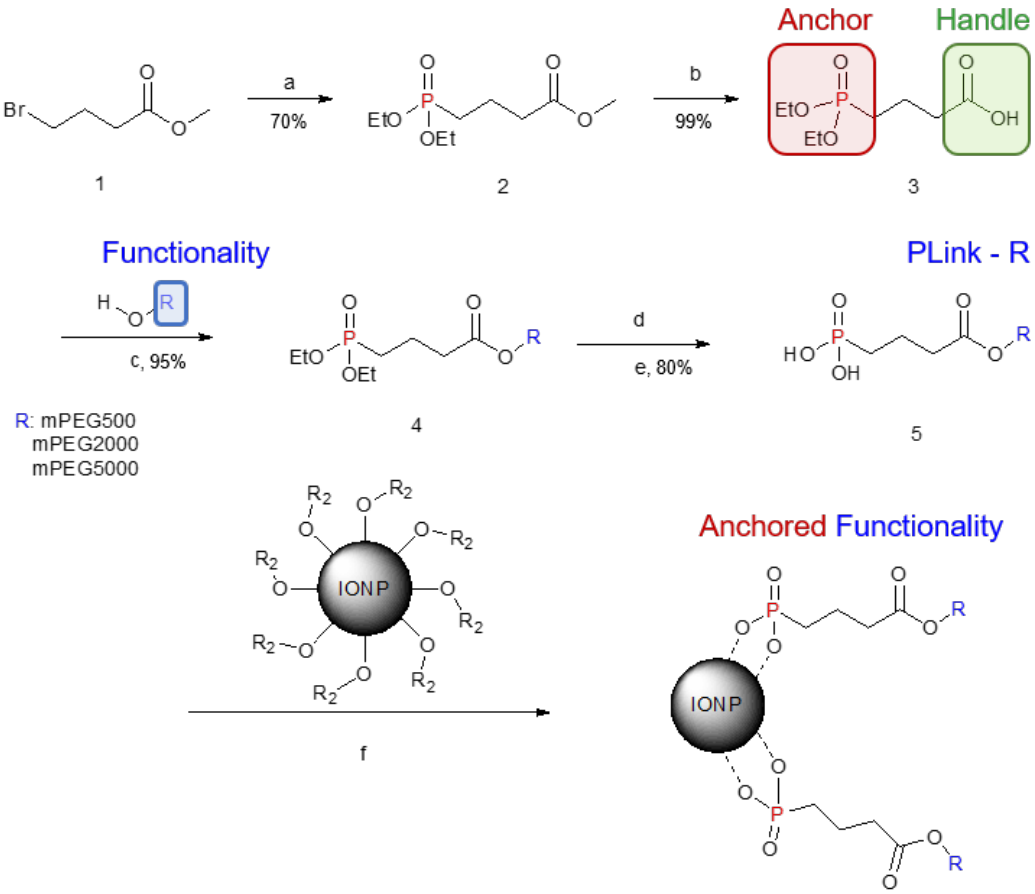

Figure 3.1. IONP functionalization via PLink and synthesis. Experimental conditions: (a) $P(OEt)_3$, 160 °C, 18 h; (b) NaOH, H_2O, rt, 4 h; (c) PEG, DCC, DMAP, rt, 18 h; (d) TMS-Br, 0 °C, 18 h; (e) MeOH, 0 °C, 4 h (f) rt, 18 h

methyl 4-(diethoxyphosphoryl)butanoate (2). The liquid methyl 4-bromobutyrate (0.9 g, 5 mmol) was added to liquid triethylphosphite (0.91 g, 5.5 mmol) without solvent. The reaction mixture was stirred at 160 °C and refluxed overnight. The crude product was distilled at 180 °C at 100 Torr vacuum to remove excess starting materials, then at 15 Torr to obtain methyl 4-(diethoxyphosphoryl) butanoate as a colorless oil. 1H NMR (400 MHz, CDCl3) δ 4.17 – 4.03 (m, 4H), 3.68 (s, 3H), 2.44 (t, J = 7.2 Hz, 2H), 2.03 – 1.89 (m, 2H), 1.85 – 1.74 (m, 2H), 1.33 (t, J = 7.1 Hz, 6H). 13C NMR (101 MHz, CDCl3) δ 173.20 (s, 1C), 61.61 (d, J = 6.4 Hz, 2C), 51.64 (s, 1C), 34.17 (d, J = 15.9 Hz, 1C), 24.93 (d, J = 141.8 Hz, 1C), 18.12 (d, J = 4.8 Hz, 1C), 16.46 (d, J = 6.1 Hz, 2C). 31P NMR (162 MHz, CDCl3) δ 31.15 (s, 1P). IR νmax/cm-1: 3457, 2984, 2955, 2910, 1736, 1643, 1439, 1392, 1370, 1226, 1175, 1137, 1098, 1054, 1024, 962, 890, 786, 691. ES-HRMS m/z 261.0879 ([M+Na]+, 100%, calc'd 261.0862), 262.0910 (16).

4-(diethoxyphosphoryl)butanoic acid (3). The liquid methyl 4-(diethoxyphosphoryl)butanoate 2 (1.1 g, 4.5 mmol) was added to a solution of NaOH (0.22 g, 5.4 mmol) in MilliQ water (10 mL). The reaction mixture was stirred for 4 hours at room temperature. The compound was extracted with ethyl acetate. First, the aqueous solution was adjusted to pH 3 using 1M HCl, and saturated with NaCl and added to a separation funnel. Ethyl acetate was added to the solution, followed by vigorous shaking and extraction three times. The organic layer was collected and dried over anhydrous MgSO4 (s), filtered and the solvent was removed from the product under reduced pressure. The resulting product was a colorless oil. 1H NMR (400 MHz, CDCl3) δ 4.20 – 4.02 (m, 4H), 2.46 (t, J = 6.9 Hz, 2H), 2.01 – 1.88 (m, 2H), 1.83 (m, 2H), 1.33 (t, J = 7.1 Hz, 6H). 13C NMR (101 MHz, CDCl3) δ 176.33 (s, 1C), 61.90 (d, J = 6.5 Hz, 2C), 34.06 (d, J = 15.8

Hz, 1C), 24.69 (d, J = 141.6 Hz, 1C), 17.91 (d, J = 4.8 Hz, 1C), 16.41 (d, J = 6.0 Hz, 2C). 31P NMR (162 MHz, CDCl3) δ 31.81 (s, 1P). IR νmax/cm-1: 3424, 2984, 2937, 2911, 1725, 1408, 1393, 1198, 1134, 1098, 1052, 1026, 964, 826, 806, 786. ES-HRMS m/z 247.0729 ([M+Na]+, 100%, calcd 247.0706), 248.0768 (14).

PEG 4-(diethoxyphosphoryl)butanoate (4). A solution of 4-(diethoxyphosphoryl)butanoic acid 3 (0.27 g, 1.2 mmol) in dichloromethane (10 mL) was added to a solution of N,N'-dicyclohexylcarbodiimide (DCC) (0.25 g, 1.2 mmol), 4-dimethylaminopyridine (DMAP) (0.001 g, 0.012 mmol) and methyl ether PEG of 500, 2000 or 5000 Da (0.5, 2, or 5 g respectively, 1 mmol) in dichloromethane (10 mL). The reaction solution was stirred at room temperature overnight. The solution was cooled to -20 °C for 1 hour and filtered through a fine frit filter funnel. Solids were washed 3 times with -20 °C CH2Cl2. The filtered solution was collected and concentrated under reduced pressure and dried on the high vac. All three PEG derivatives, PEG500, PEG2000 and PEG5000 were purified using two gravity Pd-10 column (G25 Sephadex media) stacked one on top of the other. The PD-10 column was first washed with 20mL of distilled (DI) water. 200 mg of product was dissolved in 1 mL of DI water and loaded on to the top of the top pd-10 column. 1 mL aliquots of DI water were added after previous aliquot were emptied. 1 mL fractions were collected from the lower column, immediately following addition of the product; pure product was recovered from lyophilization of the 7th-10th fraction, yielding a colorless liquid for PEG500 and a white solid for PEG2000 and PEG5000. PEG500: 1H NMR (400 MHz, CDCl3) δ 4.25 (t, 2H), 4.19 – 4.04 (m, 4H), 3.75 – 3.62 (m, 43H), 3.57 (t, 2H), 3.40 (s, 3H), 2.48 (t, J = 7.2 Hz, 2H), 2.00 – 1.88 (m, 1H), 1.88 – 1.75 (m, 1H), 1.34 (t, J = 7.1 Hz, 6H). 13C NMR (101 MHz, CDCl3) δ 173.20 (s, 1C), 71.94 (s, 1C), 70.57 (s, 1C), 69.11

(s, 1C), 63.59 (s, 1C), 61.53 (d, J = 6.4 Hz, 2C), 59.04 (s, 1C), 34.17 (d, J = 15.9 Hz, 1C), 24.93 (d, J = 141.8 Hz, 1C), 18.12 (d, J = 4.8 Hz, 1C), 16.46 (d, J = 6.1 Hz, 2C). 31P NMR (162 MHz, CDCl3) δ 31.16 (s, 1P). IR νmax/cm-1: 3468, 2875, 2749, 1732, 1647, 1456, 1391, 1350, 1325, 1292, 1241, 1202, 1105, 1054, 1029, 959, 836, 788.

PEG2000: 1H NMR (400 MHz, CDCl3) δ 4.25 (t, 2H), 4.19 – 4.04 (m, 4H), 3.75 – 3.62 (m, 180H), 3.57 (t, 2H), 3.40 (s, 3H), 2.48 (t, J = 7.2 Hz, 2H), 2.00 – 1.88 (m, 1H), 1.88 – 1.75 (m, 1H), 1.34 (t, J = 7.1 Hz, 6H). 13C NMR (101 MHz, CDCl3) δ 173.20 (s, 1C), 71.94 (s, 1C), 70.57 (s, 1C), 69.11 (s, 1C), 63.59 (s, 1C), 61.53 (d, J = 6.4 Hz, 2C), 59.04 (s, 1C), 34.17 (d, J = 15.9 Hz, 1C), 24.93 (d, J = 141.8 Hz, 1C), 18.12 (d, J = 4.8 Hz, 1C), 16.46 (d, J = 6.1 Hz, 2C). 31P NMR (162 MHz, CDCl3) δ 31.15 (s, 1P). IR νmax/cm-1: 3459, 2944, 2882, 2804, 2694, 1732, 1646, 1467, 1418, 1360, 1327, 1280, 1233, 1147, 1114, 1061, 947, 842.

PEG5000: 1H NMR (400 MHz, CDCl3) δ 4.25 (t, 2H), 4.19 – 4.04 (m, 4H), 3.75 – 3.62 (m, 453H), 3.57 (t, 2H), 3.40 (s, 3H), 2.48 (t, J = 7.2 Hz, 2H), 2.00 – 1.88 (m, 1H), 1.88 – 1.75 (m, 1H), 1.34 (t, J = 7.1 Hz, 6H). 13C NMR (101 MHz, CDCl3) δ 173.20 (s, 1C), 71.94 (s, 1C), 70.57 (s, 1C), 69.11 (s, 1C), 63.59 (s, 1C), 61.53 (d, J = 6.4 Hz, 2C), 59.04 (s, 1C), 34.17 (d, J = 15.9 Hz, 1C), 24.93 (d, J = 141.8 Hz, 1C), 18.12 (d, J = 4.8 Hz, 1C), 16.46 (d, J = 6.1 Hz, 2C). 31P NMR (162 MHz, CDCl3) δ 31.15 (s, 1P). IR νmax/cm-1: 3466, 2945, 2883, 2804, 2694, 1733, 1649, 1467, 1413, 1360, 1344, 1280, 1234, 1148, 1115, 1061, 947, 842.

(PEG-4-oxobutyl)phosphonic acid (5). A solution of PEG 4-(diethoxyphosphoryl)butanoate (4) (PEG500: 0.5 g, PEG2000: 2 g, PEG5000: 5 g, 1 mmol) in cooled CH2Cl2 (-20 °C, 4mL) was placed in a freezer for 1 hour. To this solution,

bromotrimethylsilane (0.6 g, 4 mmol) was added, the mixture was shaken and placed in a 4 °C fridge overnight. The reaction was allowed to come to room temperature and stirred for 4 hours. The resulting mixture was concentrated under reduced pressure. Cool methanol (–4 °C, 4 mL) was added. The mixture was vigorously shaken and returned to the refrigerator (4 °C) for two hours. The solution was concentrated under reduced pressure, slowly over 1 hour. PEG derivatives were purified using two gravity Pd-10 column stacked on top of each other, as described above. PEG500: 1H NMR (400 MHz, CDCl3) δ 4.27 (t, 2H), 3.66 (m, 43H), 3.57 (t, 2H), 3.40 (s, 2H), 2.51 (t, J = 7.1 Hz, 2H), 2.07 – 1.92 (m, 2H), 1.90 – 1.76 (m, 2H). 13C NMR (101 MHz, CDCl3) δ 173.20 (s, 1C), 71.94 (s, 1C), 70.57 (s, 1C), 69.11 (s, 1C), 63.59 (s, 1C), 59.04 (s, 1C), 34.17 (d, J = 15.9 Hz, 1C), 24.93 (d, J = 141.8 Hz, 1C), 18.12 (d, J = 4.8 Hz, 1C). 31P NMR (162 MHz, CDCl3) δ 31.15 (s, 1P). IR νmax/cm-1: 3436, 2877, 1732, 1647, 1456, 1350, 1280, 1246, 1179, 1105, 1023, 991, 947, 848, 774, 719, 700.

PEG2000: 1H NMR (400 MHz, CDCl3) δ 4.27 (t, 2H), 3.66 (m, 180H), 3.57 (t, 2H), 3.40 (s, 2H), 2.51 (t, J = 7.1 Hz, 2H), 2.07 – 1.92 (m, 2H), 1.90 – 1.76 (m, 2H). 13C NMR (101 MHz, CDCl3) δ 173.20 (s, 1C), 71.94 (s, 1C), 70.57 (s, 1C), 69.11 (s, 1C), 63.59 (s, 1C), 59.04 (s, 1C), 34.17 (d, J = 15.9 Hz, 1C), 24.93 (d, J = 141.8 Hz, 1C), 18.12 (d, J = 4.8 Hz, 1C). 31P NMR (162 MHz, CDCl3) δ 31.15 (s, 1P). IR νmax/cm-1: 3526, 2882, 2694, 1733, 1653, 1467, 1413, 1360, 1340, 1280, 1234, 1145, 1114, 1061, 946, 842.

PEG5000: 1H NMR (400 MHz, CDCl3) δ 4.27 (t, 2H), 3.66 (m, 443H), 3.57 (t, 2H), 3.40 (s, 2H), 2.51 (t, J = 7.1 Hz, 2H), 2.07 – 1.92 (m, 2H), 1.90 – 1.76 (m, 2H). 13C NMR (101 MHz, CDCl3) δ 173.20 (s, 1C), 71.94 (s, 1C), 70.57 (s, 1C), 69.11 (s, 1C), 63.59 (s, 1C),

59.04 (s, 1C), 34.17 (d, J = 15.9 Hz, 1C), 24.93 (d, J = 141.8 Hz, 1C), 18.12 (d, J = 4.8 Hz, 1C). 31P NMR (162 MHz, CDCl3) δ 31.15 (s, 1P). IR νmax/cm-1: 3418, 2945, 2883, 2805, 1467, 1360, 1340, 1280, 1234, 1148, 1114, 1060, 946, 842.

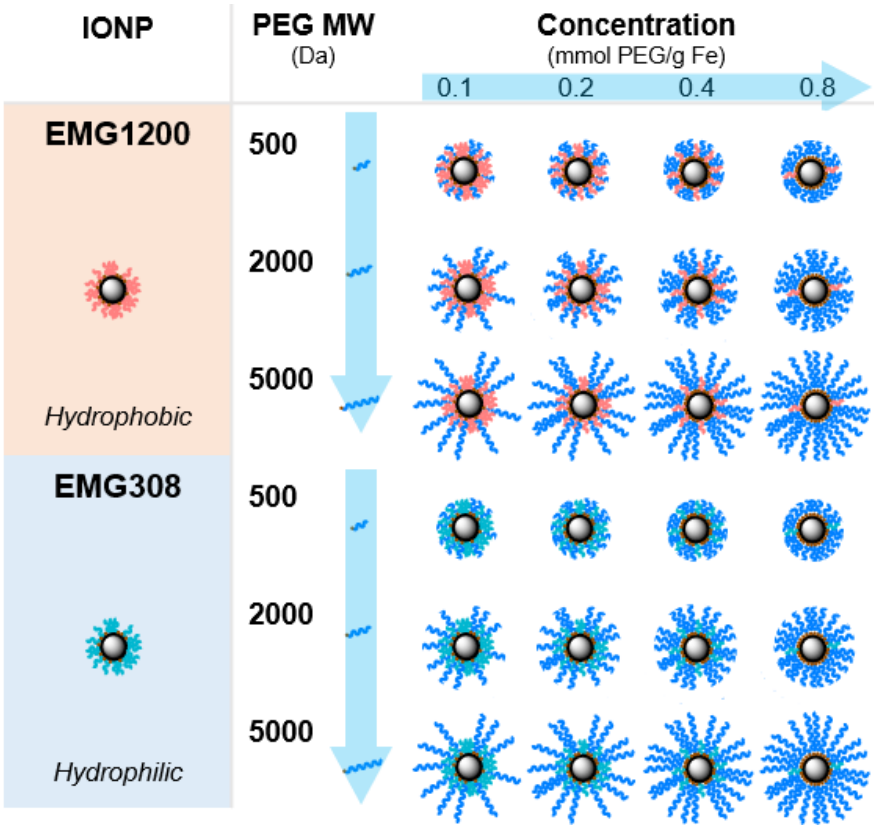

Figure 3.2. Scope of coating IONP table of IONPs coated by PEG Mw: 500, 2000 and 5000 Da and the concentration of PLink-PEG added during ligand exchange.

Ligand exchange on EMG1200. A solution of EMG1200 (Ferrotec inc. 30mg), hydrophobic fatty acid (proprietary) coated IONPs in CH2Cl2 (1 mL) was bath sonicated for 10 minutes. A solution of (PEG-4-oxobutyl)phosphonic acid (5) (PEG 500; 0.065 - 0.52 g, 0.1-0.8 mmol, PEG 2000; 0.2 - 1.6 g, 0.1-0.8 mmol PEG/g Fe, PEG 5000; 0.5-6.5 g, 0.1-1.3 mmol) in CH2Cl2 (1.4 mL) and methanol (0.6 mL) was added to the IONP solution, following concentrations and mPEG MW are shown in Figure 2. The reaction mixture was sonicated for 1 hour and removed for 1 hour three times, and then left overnight at room

temperature. Solutions were concentrated to 2 mL under reduced pressure. 2 mL of hexane was added to the solution and sonicated for 5 minutes in a glass vial. Magnet was applied vertically outside vial, where IONPs precipitated vertically along interior wall and supernatant was poured off. This was repeated twice with hexane, and four times with acetone. Hexane was added dropwise to acetone solutions to induce magnetic separation at higher PEG concentrations. Excess solvent was evaporated under reduced pressure and then under high vacuum. Distilled H2O (1.6 mL) was added to dry IONPs and redisperse with bath sonication (5 minutes) and then point sonication (5 minutes, pulse; 4 sec on, 2 sec off) to make the stock solutions.

Ligand exchange on EMG308. All PEG MW and concentrations were reacted in the same way. A solution of EMG308 (Ferrotec inc., 0.5 mL, 60 mg Fe/mL) coated in hydrophilic surfactant (proprietary) (1 mL) was added to solution of (PEG-4-oxobutyl)phosphonic acid (5) (PEG 500; 0.065 - 0.52 g, 0.1-0.8 mmol, PEG 2000; 0.2 - 1.6 g, 0.1-0.8 mmol, PEG 5000; 0.5-6.5 g, 0.1-1.3 mmol) in distilled water (1.9 mL) and methanol (0.6 mL), following Figure 2. The reaction mixture was sonicated for 1 hour, removed for 1 hour and repeated three times, and then left overnight at room temperature. Solutions were concentrated to 2 mL under reduced pressure and purified using magnetic separation. 2 mL of ethyl acetate was added to the concentrated solution, the solution was sonicated for 5 minutes in a glass vial. Magnet was applied vertically outside vial, where IONPs precipitated vertically along interior wall, and supernatant was poured off. This was repeated twice with ethyl acetate, and four times with acetone. Ethyl acetate was added dropwise to acetone solutions to induce magnetic separation at higher PEG concentrations. Excess solvent was evaporated under reduced pressure and then under high vacuum.

Distilled H2O (1.6 mL) was added to dry IONPs and redisperse with bath sonication (5 minutes) and then point sonication (5 minutes, pulse; 4 sec on, 2 sec off) to make the stock solutions.

High Resolution Magic Angle Spin (HRMAS) NMR

Lyophilized IONPs were added to 99.96% D2O and bath sonicated for 10 minutes. Approximately 10uL of 0.5-1mg Fe/mL solution was loaded on to the HRMAS NMR tube insert and approximately 20uL pure solvent was added to dilute the solution to result in a pale brown color, Figure S10. The insert was sealed with the insert pressure cap and secondary screw cap, HR-MAS disposable insert kit. The sealed insert is then inserted into the zirconium tube and pressure caped with a rotor, 4mm MAS Rotor Kit, Bruker. Samples were then loaded on the NMR, Bruker 700-MHz Avance 4-mm High Resolution Magic-Angle Spinning inverse-detect probe and spun at 6000 Hz, 25 °C, after locking to D2O, the probe was tuned for 1H acquisition. Shims were manually adjusted, using a single scan refreshing every 0.5 second. The peak shape and width at half max of D2O was optimized by increasing or decreasing shims: Z, Y, X, ZY, ZY2, Z2, Z4, and Z5. Manual shimming the D2O allowed for significantly increased resolution of peaks, where highest grade D2O gave the best results. Adjusting the phase of the spectra in the instrument during shimming, increased resolution and allowed for easier data processing.

Specific absorption rate (SAR)

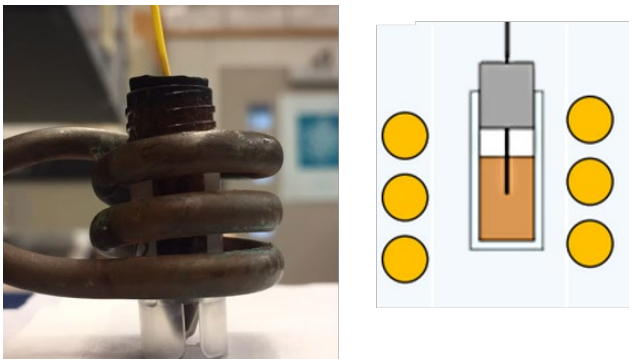

Figure 3.3. Photograph and schematic of RF coil, used for SAR measurements. Radio frequency, 3 turn coil – 360kHz, 25 kA/m 1mL of 4-8mg Fe/mL in water or VS55. Note the flouroptic probe placed within the middle of the IONP solution in order to assess the temp rate change once RF heating had begun.

Heating rate was determine as previously described using a 1 kW Hotshot inductive heating systems with 2.75-turn, water-cooled copper coil (Ameritherm Inc., Scottsville, NY), 360 kHz and 20 kA/m.[29, 33, 102] Briefly, 1 mL (approximately 6mg Fe/mL) of stock solution was added to a cryotube, Figure 3. The cryotube was capped with a rubber stopper, with a fibreoptic thermocouple through the center. Temperature was recorded in 1 second intervals for 120 seconds, initial 30 seconds for temp stabilization, 60 seconds while the coil is on and 30 seconds after the coil is off. Water and VS55 are used as reference of coil heating) SAR is calculated using the equation 1, and the first 30 seconds of temperature.

$$SAR = \frac{\rho V C_{water}}{Fe\ g}\left(\frac{\Delta T_{IONP}}{\Delta t_{IONP}} - \frac{\Delta T_{water}}{\Delta t_{water}}\right)$$

Equation 1. Specific absorption rate.

Cell studies

IONP toxicity was studied based on our previously published protocol for sIONP using HDF cells.[7] Briefly, cells were incubated with 0.3 mLs of PLink-PEG5000 0.8 mmol

PEG/g Fe coated EMG308 or EMG1200 respectively in biological media for 24 hours at concentrations 0.1, 0.5, 1, 5, and 10 mg Fe/mL.

CPA loading with IONPs toxicity was tested using our CPA step loading method at 4 °C to mimic organ perfusion.[27] HDF cells were subjected to CPA for 25 minutes in 3-minute steps, each with increasing concentration of VS55, with IONPs at 1, 5, and 10 mg Fe/mL added in the final 3 minutes.[7, 103] CPAs at high concentration at room temperature and above can lead to toxicity, thus the time interval and temperature (≤ 4 °C) were designed to limit any injury.[33, 103]

Cellular viability after cryopreservation with or without IONPs in HDF cells was tested in three experimental groups all step loaded with CPA VS55 with the following procedure: 1) HDF cells vitrified with IONPs at concentrations ranging 8- 60mg Fe/mL and nanowarmed using RF coil, 2) HDF Cells vitrified without IONPs and warmed convectively in a water bath at 37 °C, 80 °C/min warming, and 3) HDF cells without IONPs slow warmed 6 °C/min warming, data not shown.[7] Hoechst-PI stains was used to determine viability.

RESULTS AND DISCUSSION

Synthesis of PLink and IONP coating

The synthesis is versatile yet inexpensive and scalable for attaching PEG or other ligands onto IONP cores through the linker, "PLink". This linker (Fig. 1), consists of a phosphonate

“anchor” and a carboxyl “handle.” The anchor has a high affinity to iron oxide, and the handle enables functional molecules to attach to the IONP without affecting phosphonate binding to iron oxide. Other researchers have tested using phosphonates as linkers to IONPs.[106, 127-128] Davis, et. Al. also uses a 5 step synthesis, but requires centrifugation to purify the final step. This is less desirable for scale up as the time for centrifugation increases with volume. Additionally their synthesis uses an amide vs an carboxyl handle which can be more reactive or charged in salt solutions. Goff et al. also uses a 5 step synthesis, but uses a sulfur, silica, and charged nitrogen. This synthesis is more complicated and requires polymerization of PEG rather than a coupling attachment. The charged nitrogen will likely create stability issues in a salt solution or in an organ perfusion.

PLink-PEG is inexpensive to make, and the time for synthesis and purification estimated for large scale synthesis is low as shown in Table S2. Further, the purification of PLink is very scalable, as reaction ‘a’ is a distillation, reaction 'b’ is a phase separation, and reactions ‘c’ and ‘e’ are filtrations. The most expensive material and time consuming purification is addition of the PLink-PEG to the IONPs. EMG308 is 102$/g Fe and EMG1200 is 26$/g Fe. We expect future large scale purification will be done using tangential flow filtration (TFF), a continuous circulation of IONPs over a molecular weight cut off filter, which is expected to take 5 hours per 25 g of Fe. Our sIONP synthesis currently takes approximately 1 week for 1.4 g Fe.[7]

PLink is very small, 6 atoms long, allowing for attachment of CPA stable ligands to IONPs without adding significant thickness. PEG was chosen as a model ligand and the co-dissolution method for exchange is sufficient to coat the IONPs in PLink-PEG. CPA vitrification solution was comprised of 55% organic components which is termed VS55.[125]

This model CPA has been used for viability and previous work in our lab. A range of PEG MW (500, 2000, and 5000 Da) and increasing concentrations in the reaction as shown in Figure 2 were used to determine the amount of PEG needed to achieve colloidal stability of IONPs in CPA. This PEG MW range corresponds to the size of sIONPs (500 Da) and the MW of PEG has been shown in literature to stabilize gold NPs (5000 Da).[79] IONPs with initially hydrophobic or hydrophilic initial coatings were used to confirm feasibility of PLink coating method on the majority of IONPs. Two IONPs were used, EMG1200, hydrophobic, EMG308, initially hydrophilic. EMG308 has high heating capabilities and is inexpensive (SAR of 400 W/g Fe, approximately 100$/ g Fe). In our previous studies we coated EMG308 with silica and PEG to achieve long term colloidal stability in VS55.[7] EMG1200 has the same core as EMG308 but is coated with a hydrophobic fatty acid. Successful ligand exchange of the hydrophobic fatty acid with PEG will allow this IONP to become dispersible in aqueous solutions, an easy visual test as shown in Figure 4. The EMG1200 became stable in water with 0.2 mmol PEG5000/g Fe IONPs, Figure S9. The colloidal stability in water also affects IONP heating and imaging properties. Testing the ligand exchange of hydrophilic model polymer PEG, on hydrophilic EMG308 allowed determination if the Linker affected the heating and imaging properties of a IONP while not effecting the solubility in water.

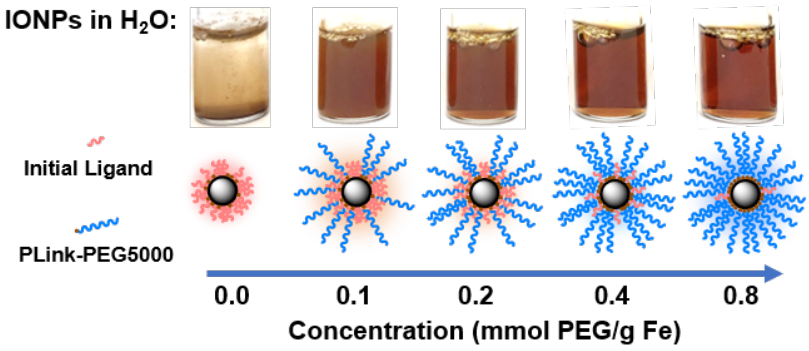

Figure 3.4. Visual stability of EMG1200, initially hydrophobic IONP, coated with increasing amounts of PLink-PEG5000 in H_2O. IONPs which are not stable in H_2O precipitate to the bottom of the vial. Increasing clarity and uniform brown color is indicative of colloidal stability, which is reached here between 0.2 and 0.4 mmol PEG5000/g Fe.

Size characterization

Dynamic light scattering (DLS) was used to measure the hydrodynamic size of coated IONPs, Figure 5 A and B. The size of PEG coated EMG1200 decreased with increasing amount of PEG added to the reaction. With 0.8 mmol PEG/ g Fe of 500, 2000, or 5000 MW PEG the IONP size was below 100nm and close to the size of EMG308, 40 nm. Increasing the MW of PEG allowed decrease in size at lower concentrations. 1200-PEG5000, EMG1200 coated with PEG, at 0.02 mmol is 240 nm, but at 0.15 it is 61 nm. Whereas, 1200-PEG500 is 225 at 0.09 mmol PEG/g Fe but at 0.2 mmol PEG/g Fe it is significantly larger at 216 nm. The increased hydrophilicity of longer PEGs overcomes the hydrophobicity of FA at lower concentrations. The size is initially high due to aggregation from the hydrophobicity of FA. The size decreases with increasing PEG (MW and concentration) as FA is replaced with PEG, resulting in decreased aggregation and increased stability.[79]

The EMG308 had little change in size due to the addition of PEG, Figure 5B, as both PEG and the initial hydrophilic surfactant are soluble in water. At 0.2 mmol PEG/g Fe of any MW all coated EMG308 were ~40 nm in size, corresponding to the smallest size of PEG5000 coated EMG1200. There is a slight increase in size with addition of PEG at ~0.4 mmol PEG/g Fe: where 308-PEG500, 2000 and 5000 are respectively: is 51 nm, 53 nm, and 48 nms, which can be attributed to steric interactions between PEG and intial

hydrophilic surfactant. TEM was used to verify this result, Figure S8, virtually no difference can be discerned between uncoated EMG1200, EMG308 and 0.8mmol PEG/g Fe of PEG5000 on each.

Importantly the size of the IONPs is close to the size before coating, meaning the addition of the coating is not significantly affecting the size of the core and will allow for high concentrations of IONPs into solution.

Stability characterization

Colloidal stability was quantified as consistent hydrodynamic size distribution over 7 days. Chiu et al has tested PEG coated IONPs with stability in CPA VS55.[129] Their initial IONPs were not stable in CPA, but with additional re-coating, they succeeded in stability in VS55. Their major issue was likely "unreacted amines resulting from remaining in PEG silane" on coated IONPs. To resolve this issue they backfilled additional PEG on to free amines on the surface. Importantly they are coating lab synthesized IONPs, not commercially available, previously coated IONPs.

Increasing size over that time was indicative of aggregation and instability. Concentration of PEG was tested on EMG1200 using PEG 5000, at 0.1, 0.2, 0.4, 0.8 mmol PEG/g Fe, Figure S9. 0.8mmol PEG 5000/g Fe resulted in the best stability and was used for the test of MW. 0.1 mmol PEG/g Fe allowed for aggregation slowly over five weeks. 0.8mmol PEG/g Fe coated on EMG1200 had the smallest size most consistently over five weeks. Therefore, IONPs of various MW were coated with 0.8mmol of PEG in the reaction. PEG5000 showed the best stability in water when compared to PEG 2000 and PEG500,

consistently under 50nm from 24 to 840 hours (35 days), Figure 5D. In water EMG1200 coated in both MW of 2000 and 5000 at 0.8 mmol PEG/g Fe IONPs were stable, but not PEG500 coated EMG1200. PEG500 is likely too short to provide stability for EMG1200 in water. All EMG308 coated samples were stable in water for 14-28 days regardless of PEG MW, Figure 5D. This was expected as uncoated EMG308 is stable in water.

The same set of IONPs were tested in VS55. Tests were halted when aggregation was above 1000 nm or after 24 hours which ever was longer. The size of a capillary of normal human glomeruli at physiological hydrostatic pressures are 10,000-21,000 nm (10-21 µm) and in rats are 7,000-9,500nm (7-9.5µm).[130] We choose 1000nm as maximum aggregated size threshold based on sedimentation of IONPs at 6000nm, seen visually (data not shown).

Uncoated EMG1200 is hydrophobic and therefore not dispersible in VS55. Increasing the concentration of coating of PEG5000 on either IONP, from 0.1 to 0.8 mmol PEG/g Fe consistently increased the stability of the IONPs in VS55, Figure S9 B and D.

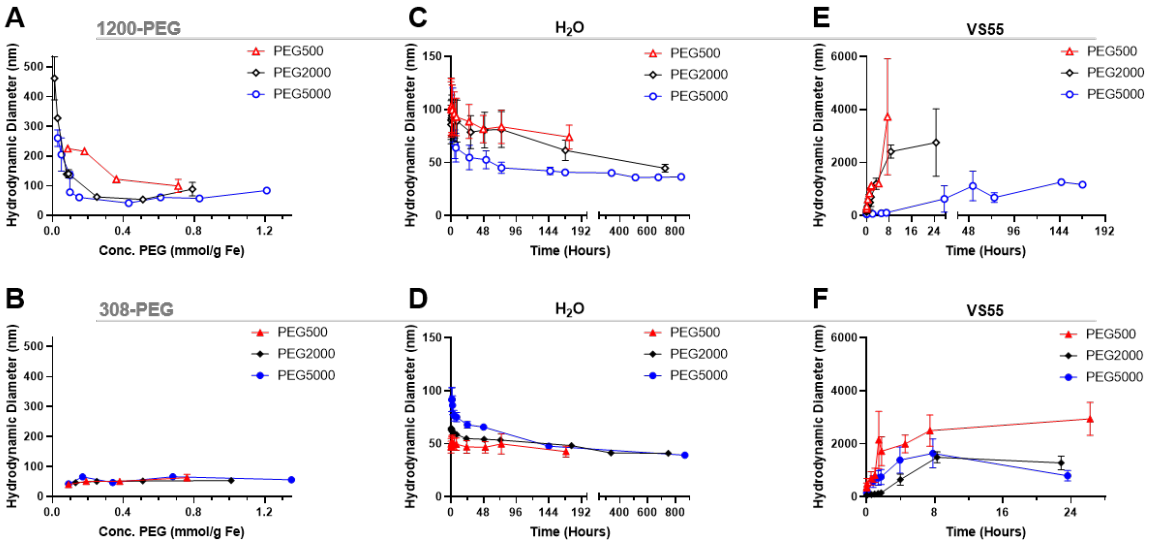

Figure 3.5. Study of IONPs as a function of PEG coating by DLS intensity weighted. **Top** PEG coated EMG1200, initially hydrophobic IONP, and **Bottom**, PEG coated EMG308, initially hydrophilic IONP, Red-PEG500, Black-PEG2000, Blue-PEG5000. **A** and **B** are size of IONPs in water as a function of PEG concentration and MW during ligand exchange. PEG concentration and MW during exchange affect aggregates of initially hydrophobic EMG1200, but less so on initially hydrophilic EMG308. **C** and **D** show stability of IONPs in water over time by function of PEG MW at 0.8 mmol PEG/g Fe. In water PEG MW affected stability of initially hydrophobic EMG1200 more so than initially hydrophilic EMG308. **E** and **F** show the impact of PEG MW on growth of IONP aggregates in VS55 CPA solution. In VS55 PEG MW affected stability of initially hydrophobic EMG1200 more so than initially hydrophilic EMG308.

The MW of the PEG coating increased the colloidal stability of both IONPs, where longer PEG increased stability and the effect was greater on the initially hydrophobic EMG1200 over EMG308, (See Figure 5E vs. 5F). PEG500 coated EMG1200 was the fastest to crash, reaching 1000 nm in two hours and full aggregation in 24 hours. PEG2000 was similar, reaching 1000 nm in 4 hours and fully crashed out by 24 hours. PEG5000 coated EMG1200 did not reach 1000 nm for 144 hours or ~ 6 days and did not fully precipitate until the 7th day. Aggregation of PEG5000 coated EMG1200 developed much slower than the other PEG coated EMG1200 and remain suspended in VS55 for 6 days.

EMG308 is dispersible in H2O but precipitates out of VS55 within 10 minutes (not shown). PEG coating significantly increased EMG308 colloidal stability in VS55 regardless of MW. Increasing the MW of PEG slowed aggregation of IONPs, where mPEG500 took 2 hours, mPEG2000 over 4 hours and mPEG5000 took over 8 hours to precipitate out.

Chiu et al success with coating lab made IONP is likely due to the lack of previous coating on the core. EMG308 is first coated with fatty acid, before coating with hydrophilic surfactant. Stabilizing EMG308 in CPA with PLink requires replacing two different ligands. The major difference in stability times in VS55 of 8 hours with 308-PEG5000, initially hydrophilic, and 6 days 1200-PEG5000, initially hydrophobic, may be attributed to left over hydrophobic layer of EMG1200 preventing cores from getting as close.

Alternatively, the reaction conditions of EMG1200 using CH2Cl2 and EMG308 using H2O may account for the difference. There is some optimization to be done on the reaction conditions of the ligand exchange to increase the amount of PEG coated on to the IONPs. Importantly, in both cases the IONPs are stable in VS55 for long enough to load, cryopreserve, nanowarm and unload IONPs from biological samples modelled using HDF cells, Figure 9. Colloidal stability was compared with and without cryopreservation and nanowarming of 1200-PEG5000 and 308-PEG5000 Figure S9 E and F respectively. Thermocycling of IONPs in CPA did not affect aggregation timing, cooling may slightly delay aggregation. 308-PEG5000 coated aggregate slow after cryopreservation and nanowarming as compared to control, fig S9F. Chiu et al also saw similar results, where cryopreservation and nanowarming did not affect stability. IONPs in CPA can be stored indefinitely using cryopreservation and nanowarming on demand to use when needed without need for sonication or redistribution.

HRMAS NMR coating analysis

Surface coating of the IONPs is important to quantify to understand both if coating is taking place and to what extent. High colloidal stability in solution will likely be correlated with high coating HRMAS NMR characterization was used to determine PEG addition to the core to give more detailed understanding ligand exchange.[131] Sample preparation for HRMAS is dependent on the signal, where high concentration of IONPs will broaden the line shape of spectra, but too low concentration makes visualizing ligands impossible. A low concentration with 1000 scans was chosen to increase better resolved peaks. Each sample was individually shimmed using the shimming program to increase the solvent peak

height and decrease the peak width at 10% and 50% 0.1 peak height. In D2O the solvent peak width at half max ranged from 1-15 ppm depending on sample composition, and purity of solvent used.

Each spectra had phase and baseline correction adjusted individually as slight concentration changes of IONP changed the spectra patterns. After processing the data, the spectra were integrated across three regions of interest: 0.5-1.32 ppm, 1.32-2.18, and 3.47-3.8, and all MW and concentrations of PEG shown in Figure S11. The region of 0.5-1.4ppm is the fatty acid coating, it is on both 1200-PEG5000, Figure 6E and 308-PEG5000, Figure 6F. This region was clipped to 1.32 ppm as there was significant interference from a broad alcohol/acid peak from 1.32-2.18 ppm. Using a clipped region allowed for consistent integration across all spectra regardless of PEG or resolution.

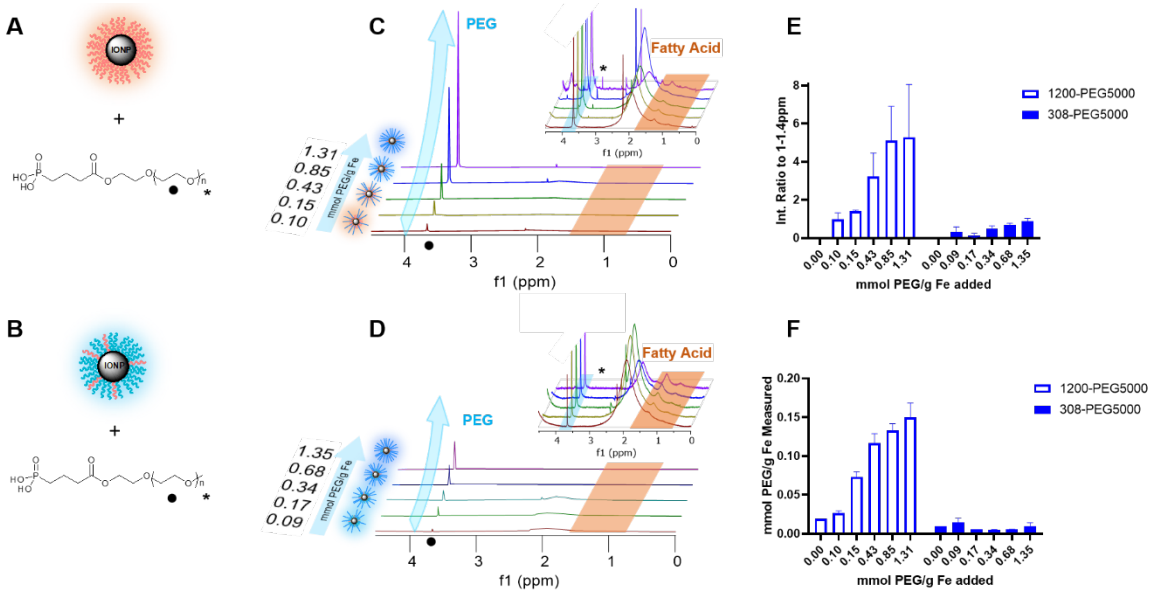

Figure 3.6. Characterization of PLink-PEG5000 coating on IONPs by HRMAS NMR and TGA. **A**, PEG coated EMG1200, initially hydrophobic IONP, and **B,** PEG coated EMG308, initially hydrophilic IONP. Cartoon representation of reaction and resulting IONPs. Black dot represents repeating chain of PEG in NMR spectra, Black star represents PEG methyl group in NMR spectra. **C,** PEG coated EMG1200, initially hydrophobic IONP, and **D**, PEG coated EMG308, initially hydrophilic IONP. Representative HRMAS NMR spectra stack of increasing PEG5000 concentration on IONPs. Inset is zoomed of same chemical shift range. Black dot represents chemical shift of PEG polymer chain (3.47-3.8 ppm),

black star (inset) represents chemical shift methyl group of PEG5000 (3.28-3.4 ppm) and orange trapezoid represents Fatty acid chemical shift (0.5-1.32 ppm). Resolved singlet of methyl group can be visualized in inset. The acid/alcohol peak can be visualized from 1.32-2.18ppm which may be an artifact of solvent, pH or PEG. **E,** HRMAS NMR data analysis of PEG5000 concentration during ligand exchange, where spectra is normalized to integration of fatty acid peak 0.5-1.32ppm. Results are reported in integration ratio of PEG peak to fatty acid peak. As PEG concentration is increased in ligand exchange, Fatty acid is removed and the ratio increases. **F** Analogous TGA data analysis of PEG5000 concentration during ligand exchange, where concentration measured is determined by weight loss percent in PEG range (300 - 430 °C).

There is a lack of consistent resolution in peaks so the integration was normalized by the spectra, where the integration of fatty acid peaks 0.5-1.4ppm was set to 1. The resulting integration of PEG therefore shows the relative amount of PEG to amount of fatty acid. A second comparison of fatty acid to PEG of all MW and concentrations of IONPs using normalization of the integration from 0-4ppm shows similar results, Figure S12. This ppm range includes the relevant groups and allows for normalization to individual spectra's resolution, as well as the decrease of fatty acid in comparison to an increase in PEG.

The chemical composition of EMG1200 is described as a hydrophobic fatty acid, determined likely to be oleic acid from the HRMAS NMR fatty acid peaks 0.5-1.4ppm comparison. EMG308 is described as EMG1200 coated with a hydrophilic surfactant which was determined to still have oleic acid on it, fatty acid peaks 0.5-1.4ppm, but also have a catechol like component, 7.5-7.9 ppm (data not shown). The catechol is very likely the attachment to the core based on dopamine IONP attachments.

The amount of PEG was increased with higher PEG concentration in either 1200-PEG5000, Figure 6C or 308-PEG5000 Figure 6D. 1200-PEG5000 IONPs had significantly more PEG then 308-PEG coated IONPs. This information matched with the TGA data as well as the stability study results.

TGA coating analysis

TGA was used to determine and verify HRMAS data for PEG surface coverage on the IONP, 1200-PEG5000, Figure 6A, and 308-PEG5000, Figure 6B. The amount of coating was determined by TGA Figure S13. We tested IONPs coated with PEG5000 since this group of IONPs showed the best results. The amount of PEG increased with addition of PEG concentration on both EMG1200 and EMG308. It plateaued in between 0.5-1 mmol PEG/g Fe which follows with the results from size, stability and heating. Further there was clearly more PEG attached on EMG1200 samples then on EMG308. The reaction conditions of the ligand exchange using CH2Cl2, a less polar organic solvent, with methanol, a polar solvent, may aid the exchange of the fatty acid for PEG. The reaction conditions of EMG308 use DI water, a very polar solvent, with methanol. In our HRMAS work we learned EMG308 has fatty acid surrounding it as well, Figure 6D. Suggesting that using two highly polar solvents for the ligand exchange may not be optimal for exchanging both the hydrophilic surfactant and left over hydrophobic fatty acid. The low interaction of the fatty acid with solvent may have sterically hindered the overall addition of PLink-PEG to the core. TGA verified PEG is attaching to the core and there is opportunity to better coat our hydrophilic core to increase concentration of stable IONPs in VS55.

Heating characterization

Heating capability is important for nanowarming, where high heating cores result in a lower need for IONPs. The PLink should not affect the capability of the core to heat to be a feasible coating method. Hydrophobic EMG1200 uncoated is not stable in water and does

not heat. Adding PLink-PEG5000 on to EMG1200 decreases aggregation in water, Figure 5A, which also increases SAR, Figure 7. Interestingly stability in water did not correspond to maximum heating in water. Although the size is minimized at 0.20 mol PEG/ g Fe, Figure 5A, heating is not maximized until concentrations above 0.43 mol PEG/g Fe on EMG1200, Figure 7. EMG1200 has a SAR in chloroform, following equation 1 replacing chloroform for water values, of 200 W/g Fe (data not shown), a solvent it is stable in. 1200-PEG5000 coated with 0.06 or 0.15 mmol PEG/g Fe are not stable in water and have low SAR, 25W/g Fe and 79W/g Fe. 0.2 mmol PEG/ g Fe afforded stability in water (Figure S8), but did not maximize SAR, 135 W/ g Fe. 1200-PEG5000 coated with 0.4, 0.8, 1.2 mmol PEG/g Fe were also stable in water for 35 days, and SAR was maximized, ranging 177-184 W/g Fe, approximated to 180W/g Fe due to Fe quantification of +/- 10% error. Therefore stability alone cannot be used to determine optimal amounts.

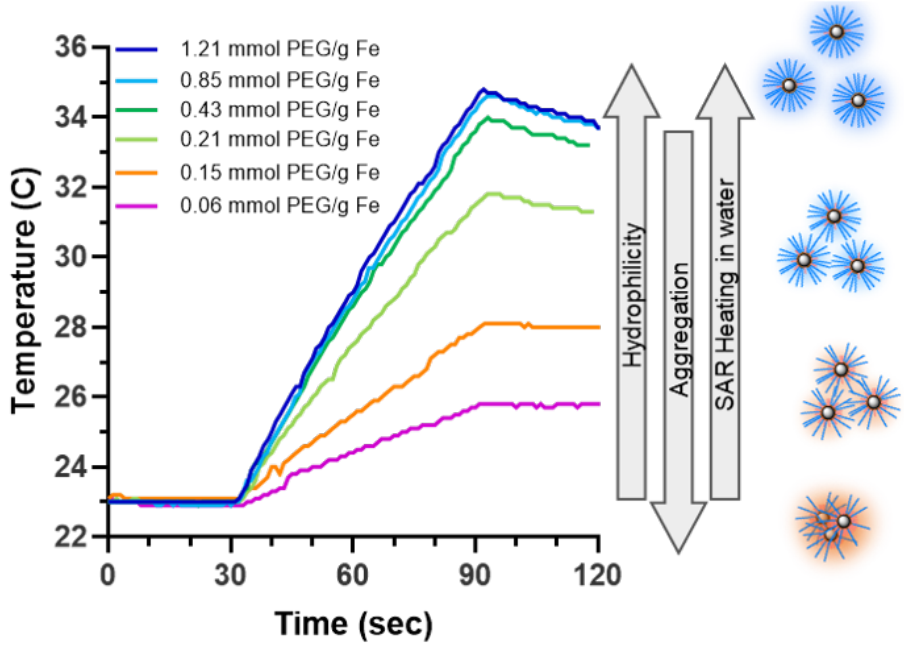

Figure 3.7. Study of IONPs heating capabilities as a function of PEG5000 coating on EMG1200, initially hydrophobic IONPs. Concentration of IONPs is 4.5+/- 0.3 mg Fe/mL. Where

increasing PEG leads to higher heating rates due to a decrease in aggregation until saturation at roughly 0.8 mmol PEG/g Fe.

PLink PEG coated IONPs were tested in water and VS55 to determine 1. If PLink PEG coating on hydrophobic EMG1200 increasing stability in water also resulted in maximizing SAR in water, 2. If PLink preserved SAR of already stabilized hydrophilic EMG308 in water, 3. SAR preservation of both IONPs in VS55. SAR was optimized in water for both EMG1200, initially hydrophobic, and EMG308, initially hydrophilic using our 1 kW coil as previously described.[7, 29, 33, 102] Heating rates were tested at 6 mg Fe/mL in 1 mL total volume in water. This concentration of iron was chosen to be above the noise of poorly heating IONPs. 1 mg Fe/mL of IONPs was not statically above the background heating of water reference for 1200-PEG IONPs with low concentrations of PEG (data not shown). In our previous work we showed SAR measured from 1-15 mg Fe/mL are statistically the same, further Fe quantification to +/- 10% is expected.[7] Therefore we tested samples with 4-8 mg Fe/mL the expected range of IONP concentration in an organ.[7] The SAR of EMG1200 uncoated was determined using chloroform as the solvent which it is stable in, 200 W/g Fe (data not shown). The SAR of EMG308 uncoated, using water as a solvent, it is stable in in 400 W/g Fe, from our previous work.[7] PLink-PEG of MW 500, 2000 and 5000 Da were coated on to EMG1200 and EMG308 in concentration ranging from 0.06-1.35 mmol PEG/ g Fe IONP. As shown in Figure 5A, increasing PEG MW and concentration increased stability of EMG1200 in water and preserved EMG308 stability. The effect on SAR was similar; increasing PEG MW and concentration on EMG1200 Figure 7&8 increased SAR and preserved SAR on EMG308, Figure 8.

MW and concentration affected EMG1200 SAR in water. PEG 500, Figure 8A, resulted in the lowest heating effects where the SAR was 20-35 W/g Fe regardless of concentration of PEG. PEG2000, Figure 8B, was able to maximize SAR in water with concentrations of 0.5 mmol/g Fe and above. PEG5000, Figure 8C, was also able to maximize SAR with concentrations of 0.4 mmol PEG/ g Fe and above. In cases of EMG1200 coated with PEG2000 and PEG5000, 0.5 and 0.4 mmol PEG/g Fe, respectively, is sufficient to achieve maximum SAR by ordinary one-way Anova, Figure S14A.

PLink PEG coating on EMG308 did not decrease the SAR with increase concentration or varying the MW. Using PLink as an ligand anchor does not damage the IONP cores structure or cores heating capabilities. EMG308 has a SAR of 400W/g Fe in water before coating, by adding increasing concentrations of PEG500, 2000 and 5000, Figure 8D-F, and no statistical difference was observed after coating, Figure S14.

SAR in VS55 was lower in water for PLink-PEG 1200 and 308, as previously observed with silica coating as well.[7] The MW and concentration of PLink PEG coating effect on SAR of EMG1200 and EMG308 followed a similar trend in VS55 to water. EMG308 had minimal effect on SAR from increasing MW or concentration, Figure 8D-F. PEG500, Figure 8A on EMG1200 in any concentration was low, 17-25 W/g Fe. PEG2000, Figure 8B increased the SAR to 51 W/g Fe at maximum coating. PEG5000, Figure 8C, at 0.8mmol PEG/g showed the best effect on EMG1200, SAR in VS55 of 73 W/g Fe.

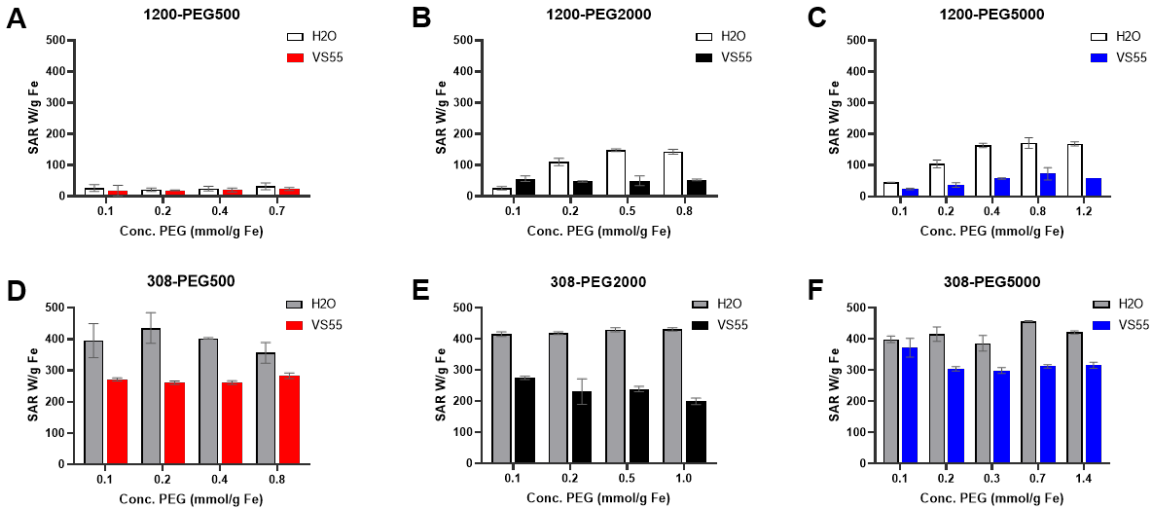

Figure 3.8. Heating capabilities of IONPs as a function of PEG MW and concentration during ligand exchange in water and VS55. 1 mL of 4-8 mg Fe/mL IONPs in water of VS55, n=3, ΔT determined from slope over first 30 seconds. **Top** PEG coated EMG1200, initially hydrophobic IONP coated with 0.8mmol PEG/g Fe **A,** PEG500 **B,** PEG2000, and **C,** PEG5000. Black boarder and white fill - IONP heating in water, solid fill – IONPs heating in VS55. Effect on heating in water is greater than heating in VS55 due to both PEG MW and concentration on initially hydrophobic EMG1200. **Bottom** PEG coated EMG308, initially hydrophilic IONP coated with 0.8mmol PEG/g Fe **D,** PEG500 E**,** PEG2000, and **F** PEG5000. Black boarder and grey fill - IONP heating in water, solid fill – IONPs heating in VS55. Effect on heating in VS55 is slightly affected by PEG MW or concentration on initially hydrophobic EMG1200, yet heating in water is not affected.

The PLink coating method did not show any negative effects on heating capability, proving it is a good candidate for a small molecule coating method for nanowarming. MW of PEG had minimal effect on SAR of EMG308 in VS55. PEG 5000 coated IONPs had better SAR in VS55, Figure 8C&F. PEG5000 coated IONPs showed superior stability and heating capabilities for nanowarming applications and were chosen for cell studies.

Cell toxicity and nanowarming studies

IONPs and the nanowarming effect were tested on HDF cell viability as we have shown in our previous studies.[7, 27, 103] Initially, the toxicity of IONPs 1200-PEG5000 and 308-

PEG5000 in cell media was compared to fresh cells, Figure 9.[33] Toxicity of HDF cells was determined by exposure to IONPs in media. HDF cell viability was not affected by either 308-PEG5000 or 1200-PEG5000 at any concentration of Fe. The viability of HDF cells, however, decreases with increasing concentration of EMG308 from our previous studies.[7]

The toxicity of step loading and unloading IONPs within VS55 and additional stress of IONPs was tested using our previous described procedure, Figure 9B.[7] 1-10 mg Fe/mL of 308-PEG5000 was used to compare to our previous studies. To account for the lower SAR of 1200-PEG5000, Figure 8C, a higher range of concentrations 1-30 mg Fe/mL was tested. All tests resulted in viability above 97%. There was no statistical difference in viability between fresh cells and those treated with VS55 and IONP loading and unloading procedure, determined by one way Anova.

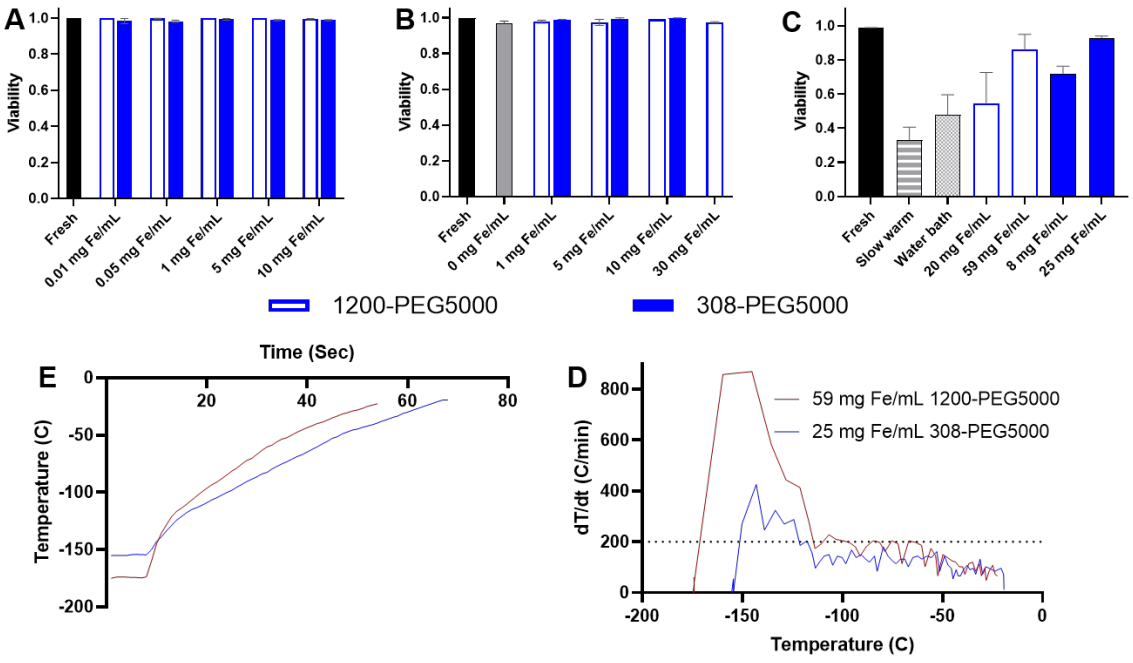

Figure 3.9. Cell studies. **A,** HDF Cells incubated in EMG1200 or EMG308 coated with 0.8mmol PEG5000/g Fe. IONPs added to cell media and incubated overnight. **B,** load and unload VS55 and IONPs on to HDF cells. Step loading increasing percentages of VS55 in Euro Collins (EC): 0%(EC), 18.75%, 25%, 50%, 75% and 100% with IONPs over ice. Step unloading percentages 50%, 18.75%, 0% (EC) Each solution was added to cells for 3 minute increments before removal and addition of next step. concentration. **C,**

Cryopreservation of HDF cells with VS55 and different rewarming techniques. 96 Well plate was cut into individual wells where cells are loaded. Cells are step loaded with VS55 as above, for nanowarming IONPs are added to 100% VS55. Cut wells are placed into a cryotube with a thermocouple and place in LN_2 Vapor and cooled to -150 °C. Cryotubes are then warmed in various ways. For slow warmed a LN_2 is Styrofoam box and allowed to cool for 5 minutes, when the LN_2 is removed and the cryotube is added. The cryotube is allowed to warm up slowly to 0 ºC . VS55 is then step unloaded. Water bath is placing the cryotube in 37ºC water bath until the sample is at 0 ºC when the VS55 is step unloaded. IONP samples are placed into the RF coil and warmed to 0 ºC when again VS55 is step unloaded. 308-PEG5000 is at a concentration of 10 mg Fe/mL and 1200-PEG5000 is at 30 mg Fe/mL due to lower SAR in VS55. **D,** Nanowarming HDF cells from cryopreserved state. **E,** Derivative of nanowarming HDF cells temperature by time based on temperature. This results in the heating rate °C/min at each temperature. In both best case scenarios heating rates are close to 200 °C/min or above, dotted line.

Cryopreservation and rewarming of HDF cells were tested using both 308-PEG5000 and 1200-PEG5000 and compared to slow warming and a water bath, Figure 9C.[7, 27] HDF cells vitrified and rewarmed slowly with VS55 had 33% viability. Convective warming in the 37 °C water bath the viability was increased to 48%. Cells which were loaded with CPAs and either 1200-PEG5000 or 308-PEG5000 and nanowarmed had higher viability than either slow-warmed or water bath warmed cells. 1200-PEG5000 required significantly more concentration of IONPs to achieve the same heating rates as 308-PEG5000 IONPs due to the lowered SAR and decreased SAR in VS55. Initially 20 mg Fe/mL of 1200-PEG5000 was used for rewarming HDF cells, this resulted in 54% viability, slightly above using a water bath. Tripling this concentrating to 60mg/mL increased the heating rates to over 200 °C/min, Figure 9D and the viability increased to 87%, Figure 9C. 308-PEG5000 showed similar results, at 8mg Fe/mL viability is 73%, but after increasing the concentration of IONPs to 25 mg Fe/mL viability is increased to 93%, as shown with statistical analysis in Figure S15. Figure 9D shows the warming profile of both 1200-PEG5000 and 308-PEG5000, both reach -20 °C in under 50 secs. The derivative, Figure 9E, shows a heating rate above or close to 200 °C/min, well above any other heating method. Herein, we show that heating rate, and therefore viability can be tuned using

increasing concentrations of IONPs of various SAR. Using higher concentrations of IONPs with lower SARW/g Fe similar viability is achieved as when using lower concentrations of high SAR W/g Fe IONPs.

CONCLUSIONS

The use of a phosphonate small molecule linker, (Plink) to attach PEG directly to IONP cores showed that the linker did not affect the heating capabilities of the core. The model ligand of PEG was attached to the core through PLink and of the three MW tested, PEG5000 allowed for the best effect on stability. A minimum concentration of 0.4 mmol PEG/g Fe is sufficient to maximize stability and heating. Coating amount plateaus with 0.8 and 1.2+ mmol PEG/g Fe as observed by TGA and HRMAS. At the highest concentration PEG may interfere sterically and slightly decrease the amount of PEG coated on to IONPs. The best coated IONPs were determined from highest heating, and longest colloidally stable in VS55: 0.8mmol PEG5000/g Fe on EMG1200 and EMG308. These two IONPs were used for testing cell toxicity and cryopreservation and nanowarming viability. Neither IONP resulted in toxicity during overnight incubation or following the loading and unloading procedure of CPA without cryopreservation. Viability of cryopreserved HDF cells was tuned by increasing concentrations of IONPs, resulting in survival of 87% with 60 mg/mL of 1200-PEG5000 and 93% with 25 mg Fe/mL of 308-PEG5000. Both PLink-PEG5000 coated IONPs are capable of heating rates at or above 200 °C/min. Further, the heating rate can be tuned to increase viability in cryopreserved samples, such as HDF cells, by choosing a IONP and an adjusting concentration. the concentration. Our future studies include exploring maximizing concentrations of IONPs in CPA to maximize heating rates and viability of biological samples. Coating efficiency will be optimized by reaction conditions, such as: aprotic solvents, increasing temperature and scaling up.

SUPPORTING INFORMATION

Experimental

Table S3.1. VS55 components. Chemicals and concentrations in the CPA VS55, with Euro Collins as the carrier solution.

CPA: VS55		
Component	**Chemical**	**Mol/L**
VS55	DMSO	3.1
	Formamide	3.1
	Propylene Glycol	2.2
	HEPES	0.01
Euro Collins Carrier solution	Glucose	0.19
	KH_2PO_4	0.01
	K_2HPO_4	0.04
	KCl	0.02
	$NaHCO_3$	0.01

NMR analysis

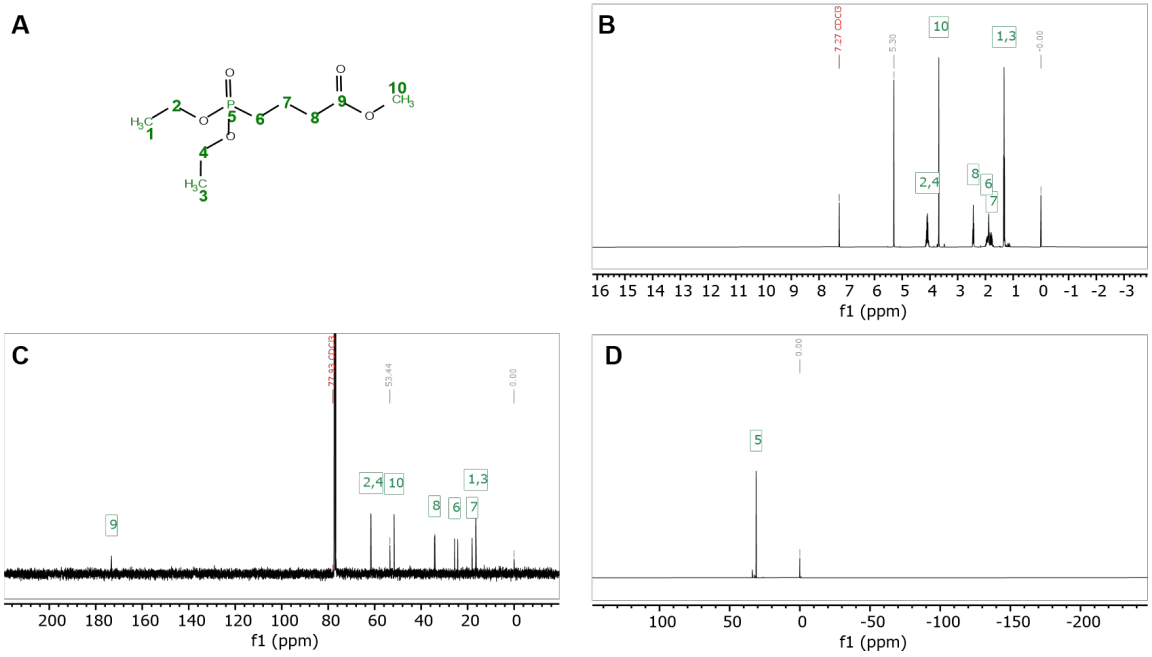

Figure S3.1. Area of interest 1H NMR (400 MHz, CDCl3) spectra for synthesis A. Methyl 4-(diethoxyphosphoryl)butanoate (**2**); **B.** 4-(diethoxyphosphoryl)butanoic acid (**3**) **C.** PEG 4-(diethoxyphosphoryl)butanoate (**4**); **D.** (PEG-4-oxobutyl)phosphonic acid (**5**)

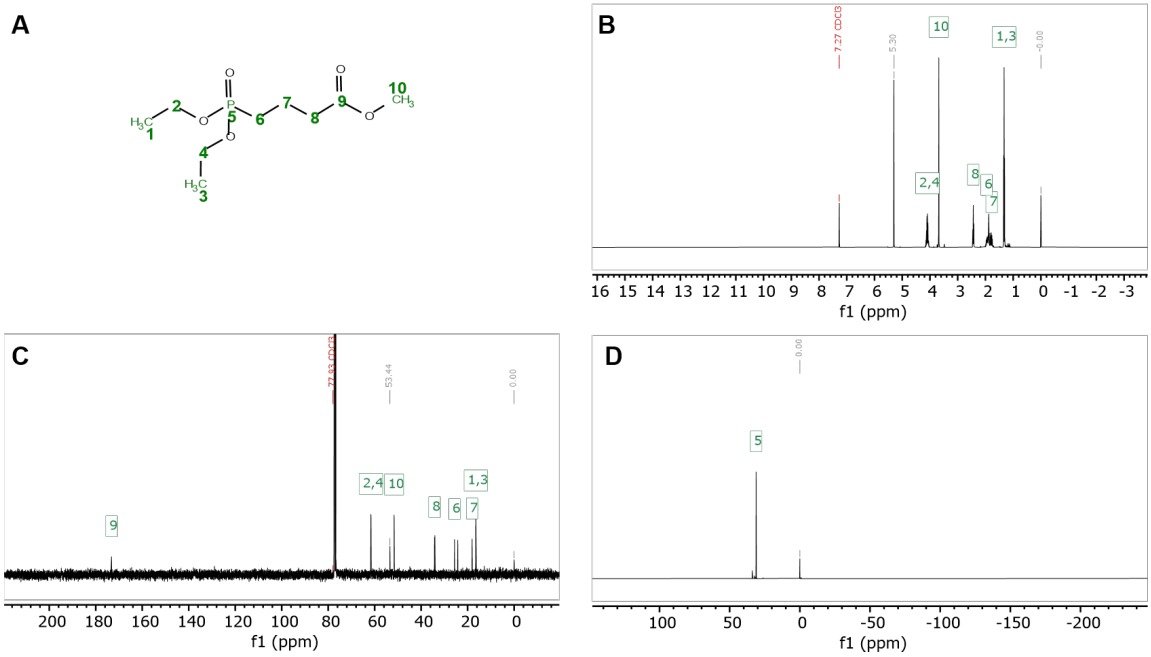

Figure S3.2. NMR spectra of methyl 4-(diethoxyphosphoryl)butanoate (2) A. Chemical structure **B.** ^{1}H NMR (400 MHz, $CDCl_3$) **C.** ^{13}C NMR (101 MHz, $CDCl_3$) **D.** ^{31}P NMR (162 MHz, $CDCl_3$)

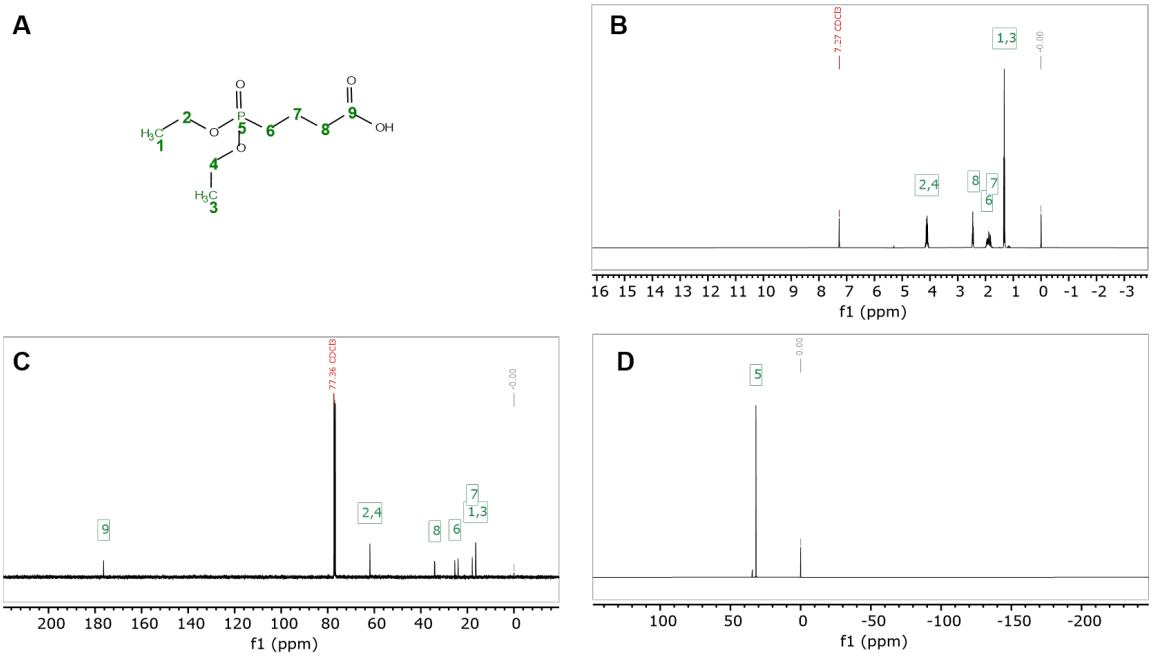

Figure S3.3. NMR spectra of 4-(diethoxyphosphoryl)butanoic acid) (3) A. Chemical structure **B.** ^{1}H NMR (400 MHz, $CDCl_3$) **C.** ^{13}C NMR (101 MHz, $CDCl_3$) **D.** ^{31}P NMR (162 MHz, $CDCl_3$)

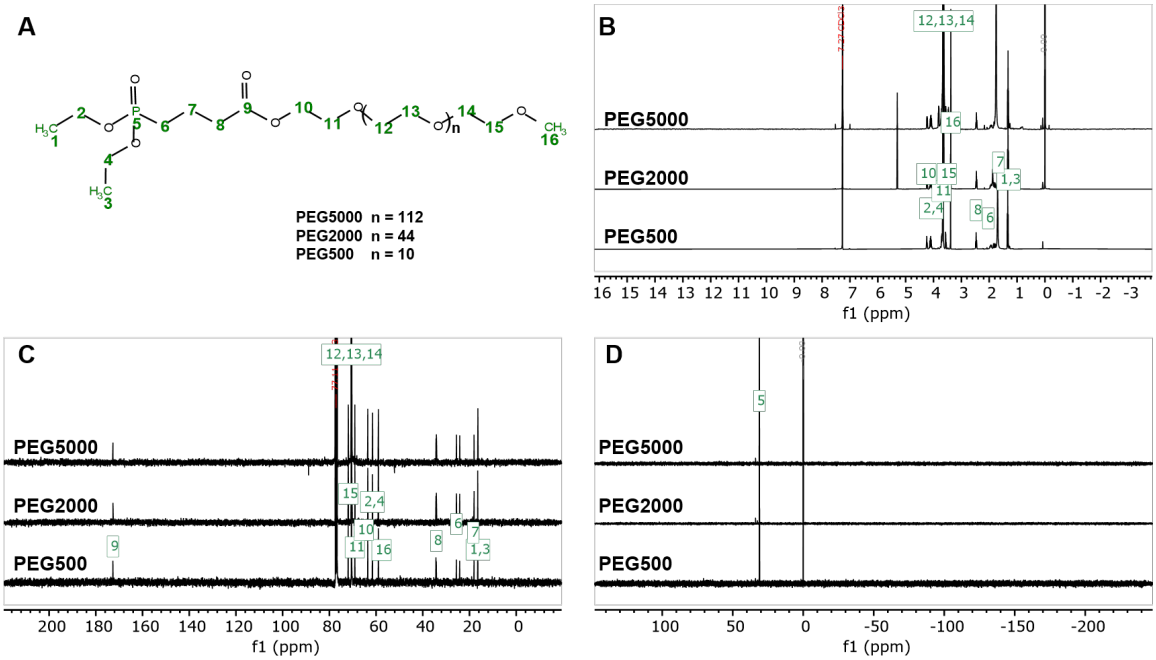

Figure S3.4. NMR spectra of PEG 4-(diethoxyphosphoryl)butanoate (**4**) **A.** Chemical structure **B.** ^{1}H NMR (400 MHz, $CDCl_3$) **C.** ^{13}C NMR (101 MHz, $CDCl_3$) **D.** ^{31}P NMR (162 MHz, $CDCl_3$)

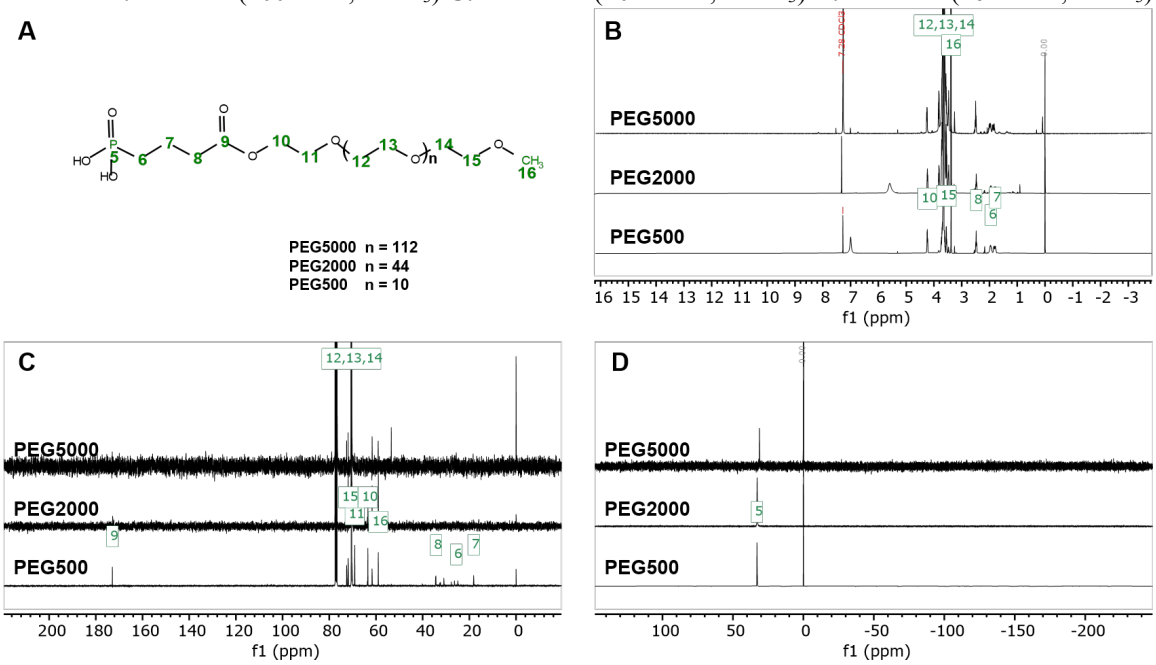

Figure S3.5. NMR spectra of (PEG-4-oxobutyl)phosphonic acid (**5**) **A.** Chemical structure **B.** ^{1}H NMR (400 MHz, $CDCl_3$) **C.** ^{13}C NMR (101 MHz, $CDCl_3$) **D.** ^{31}P NMR (162 MHz, $CDCl_3$)

IR data:

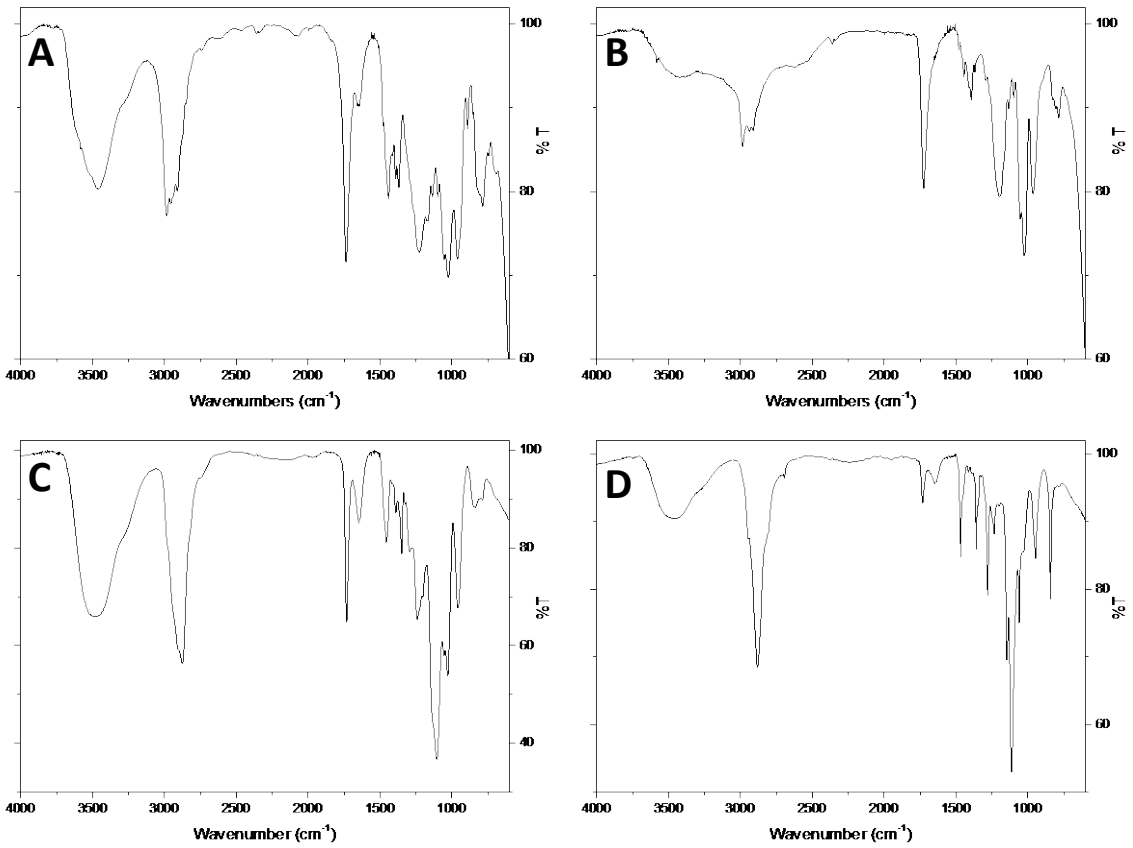

Figure S3.6. FT-IR spectra of (A) compound 2, (B) compound 3, (C) compound 4 PEG500, and (D) compound 4 PEG2000.

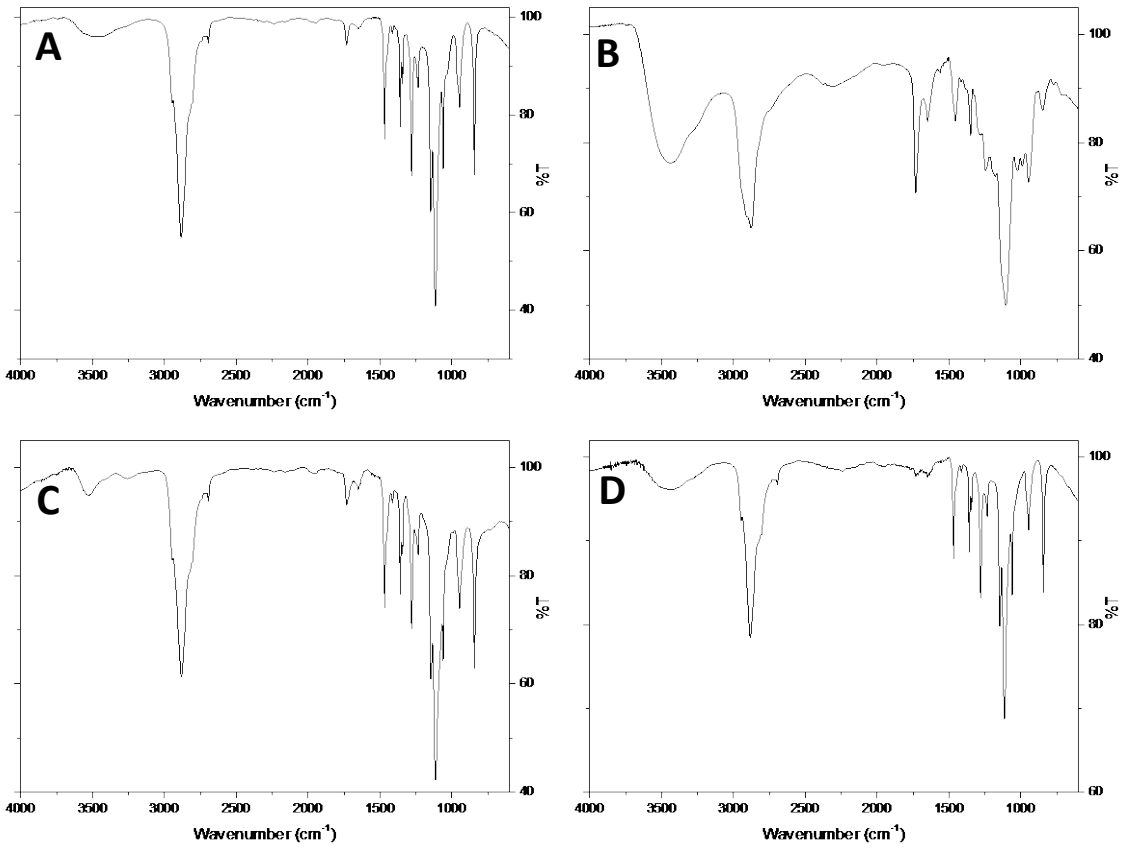

Figure S3.6B. FT-IR spectra of (A) compound 4 PEG5000, (B) compound 5 PEG500, (C) compound 5 PEG2000, and (D) compound 5 PEG5000.

MS data:

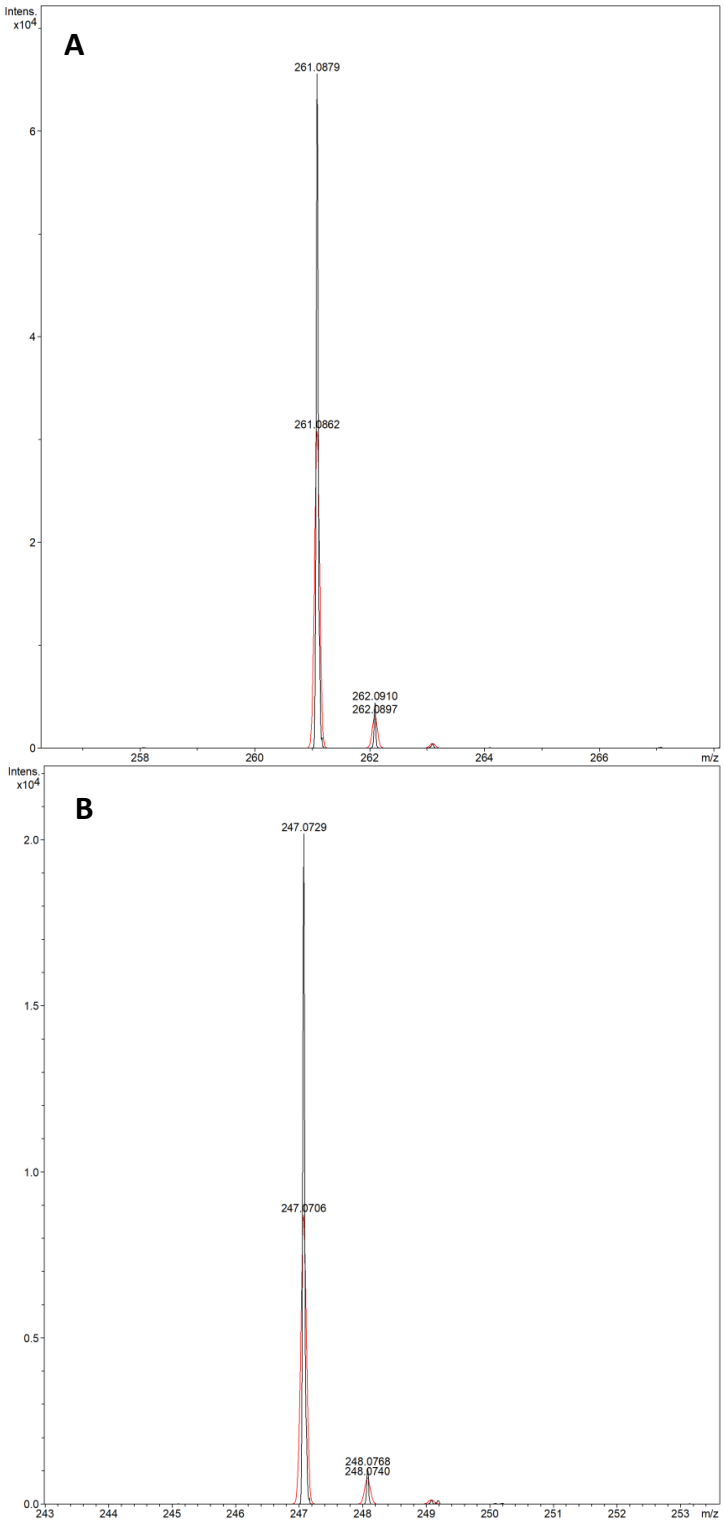

Figure S3.7. ESI-MS spectrum of (A) compound **2** ($[M+Na]^+$) and (B) compound **3** ($[M+Na]^+$), experimental (black) and calculated (red).

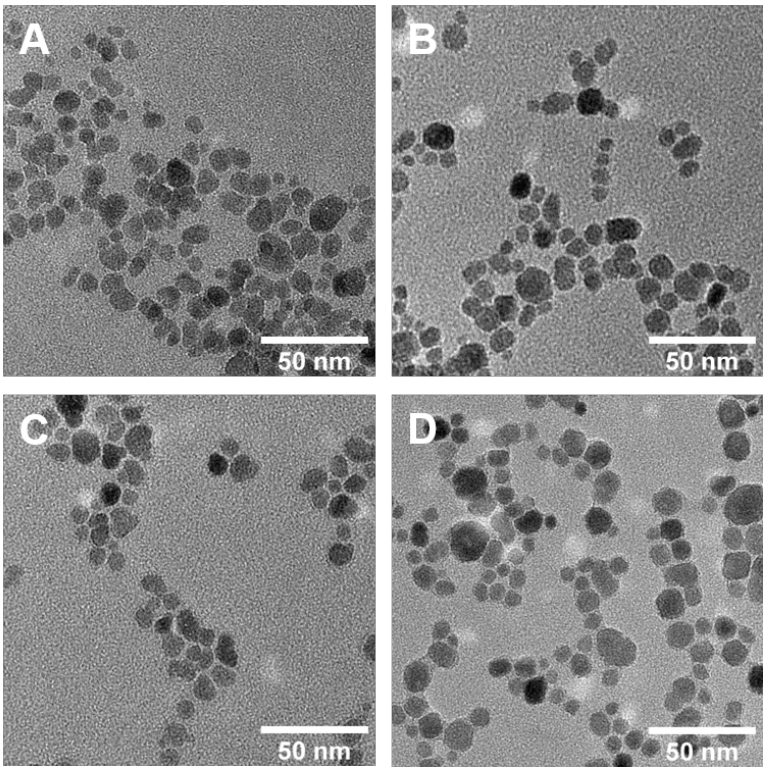

Figure S3.8. TEM images of IONPs. **A.** EMG1200-PEG5000, **B.** EMG308-PEG5000 **C.** EMG1200, **D.** EMG308.

Table S3.2. Cost analysis of EMG1200 or EMG308 coating.

Chemicals cost per g Fe of IONPs and the labor hours estimated for a large scale synthesis of 100 g of IONPs. Largest cost of materials comes from the cost of the IONP in either case. Costs are estimated from current available prices as of February 2022

Reaction	RXN yield	Chemical	MW (g/mol)	Eqv. (moles)	Cost ($/g Fe IONP)	Labor for 100 g (hours)	
						Synthesis	Purification
a	70%	Methyl-4-bromobutyrate	181	1	$ 0.12	1	4
		Triethyl phosphite	166	1.5	$ 0.03		
b	99%	Sodium hydroxide	40	2	$ 0.01	0.25	3
		H2O	*18*	*139*	$ -		
c	95%	mPEG 5000	5000	1	$ 1.10	0.25	3
		DCC	206	1.1	$ 0.08		
		DMAP	122	0.01	$ 0.00		
		DCM	*85*	*156*	$ 0.48		
d/e	80%	TMSBr	153	4	$ 1.41	1	10
		DCM	*85*	*156*	$ 0.46		
		Isoprop	*60*	*5000*	$ 6.87		
f	-	**EMG 308**	-	-	**$ 102.00**	10.5	20
		MeOH	*32*	*619*	$ 0.73		
		H2O	*18*	*4167*	$ -		
				Total cost	**$ 113.29**		
f	-	**EMG1200**	-	-	**$ 31.25**	10.5	20
		MeOH	*32*	*619*	$ 0.73		
		DCM	*85*	*1565*	$ 3.66		
				Total cost	**$ 46.20**		

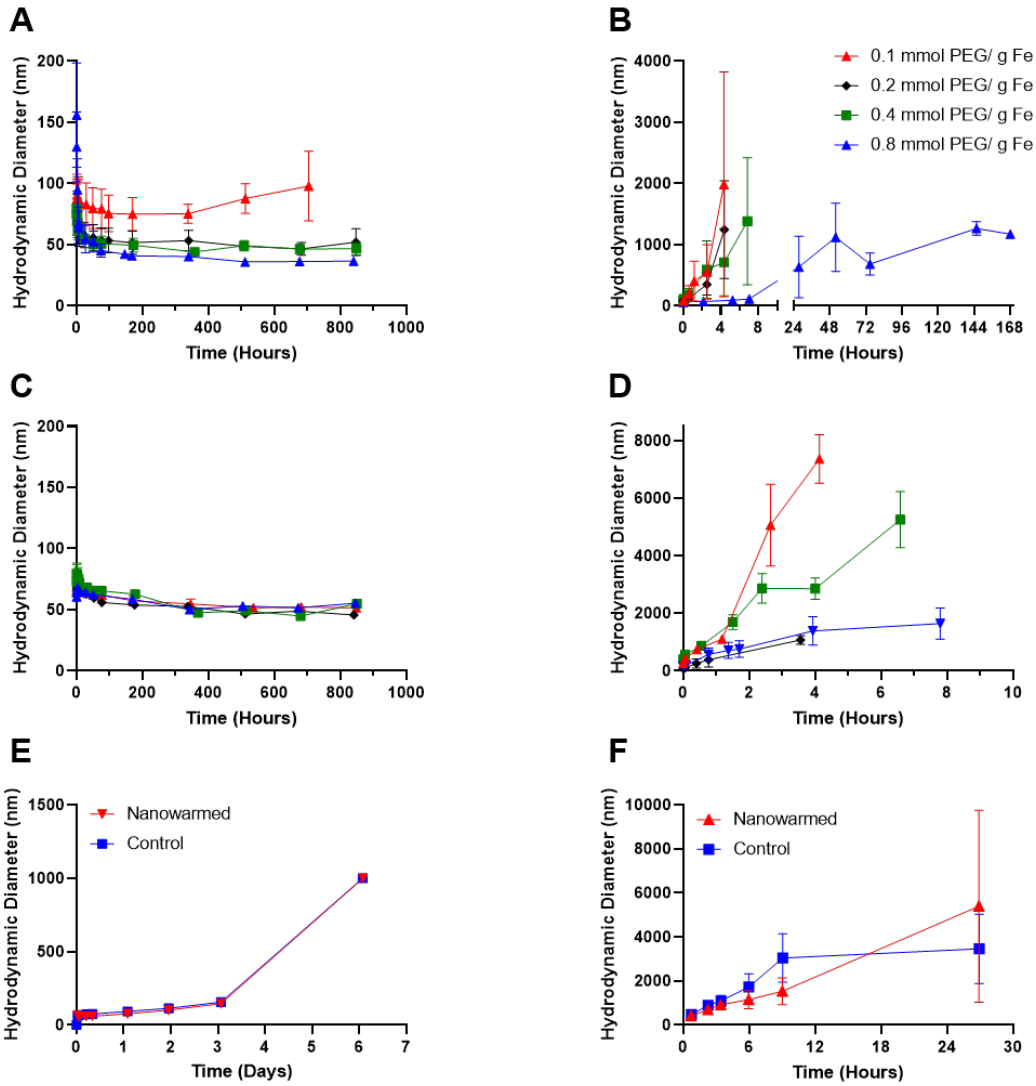

Figure S3.9. DLS stability of IONPs with increasing concentration of PEG5000 weighted by intensity. **A.** 1200-PEG5000 in H_2O, **B.** 1200-PEG5000 in VS55. **C.** 308-PEG5000 in H_2O, **D.** 308-PEG5000 in VS55. Upper left legend applies for all; Red triangle is 0.1 mmol PEG/g Fe, black square is 0.2 mmol PEG/g Fe, green triangle is 0.4 mmol PEG/g Fe, Blue diamond is 0.8 mmol PEG/g Fe. **E.** 1200-PEG5000 at 0.8 mmol PEG/g Fe with or without cryopreservation and nanowarming. **F.** 308-PEG5000 at 0.8 mmol PEG/g Fe with or without cryopreservation and nanowarming.

HRMAS sample preparation:

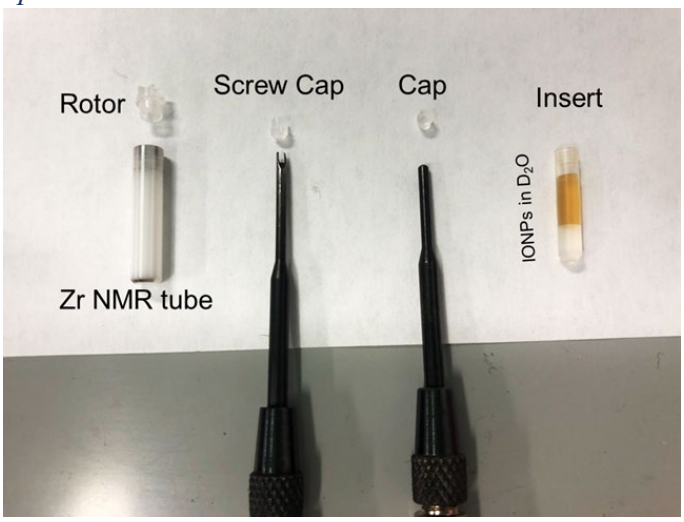

Figure S3.10. HRMAS NMR tube set up and solution color for reference

HRMAS NMR spectra of all coated samples:

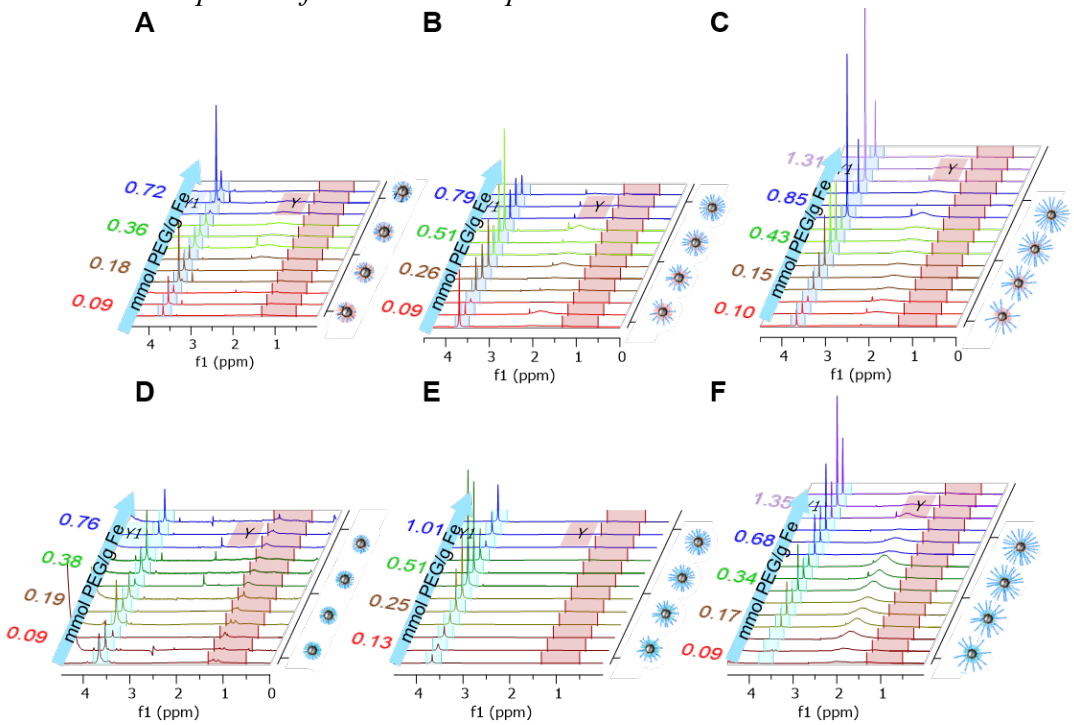

Figure S3.11. 1H HRMAS NMR (600 MHz, D_2O) of coated PLink-PEG coated IONPs. **A.** EMG1200 coated with PEG500. **B.** EMG1200 coated with PEG2000. **C.** EMG1200 with PEG5000. **D.** EMG308 coated with PEG500. **E.** EMG308 coated with PEG2000. **F.** EMG308 coated with PEG5000.

The 0.5-1.32ppm fatty acid region is broad when using D_2O, but the region is more resolved when using DMSO (data not shown). Unfortunately, DMSO d-6 provided a larger H_2O peak (3.33 ppm) which overlaps with the PEG. Accurate integration of PEG when using DMSO d-6 as solvent is not possible due to peak, so the data is not included. Chloroform was also tried as a solvent, but shimming was not possible. A clear residual solvent peak must be present to shim. In chloroform the residual solvent peak is already so narrow shimming effects cannot be clearly discerned.

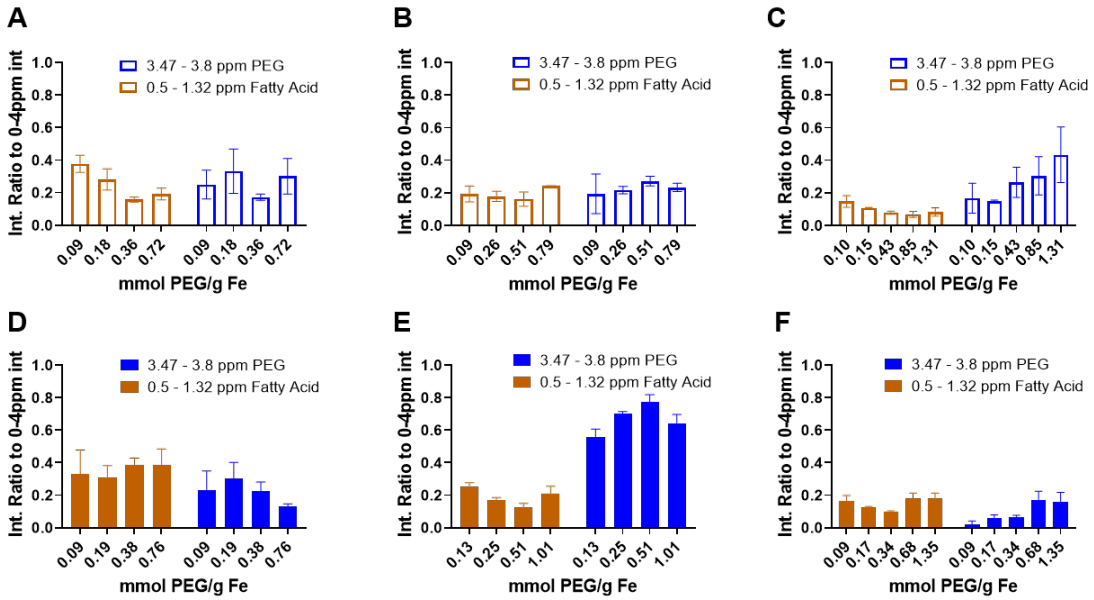

Figure S3.12. 1H HRMAS NMR analysis of PEG peak to fatty acid peak of coated PLink-PEG coated IONPs. Integral of area from 0 to 4ppm was normalized to 1, integral from 3.47 to 3.8ppm is PEG (blue) and integral from 0.5 to 1.32 ppm is fatty acid (orange). Spectra was normalized to total area of interest (0-4ppm) to account for differences in resolution between samples. **A.** EMG1200 coated with PEG500. **B.** EMG1200 coated with PEG2000. **C.** EMG1200 with PEG5000. **D.** EMG308 coated with PEG500. **E.** EMG308 coated with PEG2000. **F.** EMG308 coated with PEG5000.

TGA of all PEG5000 coated samples

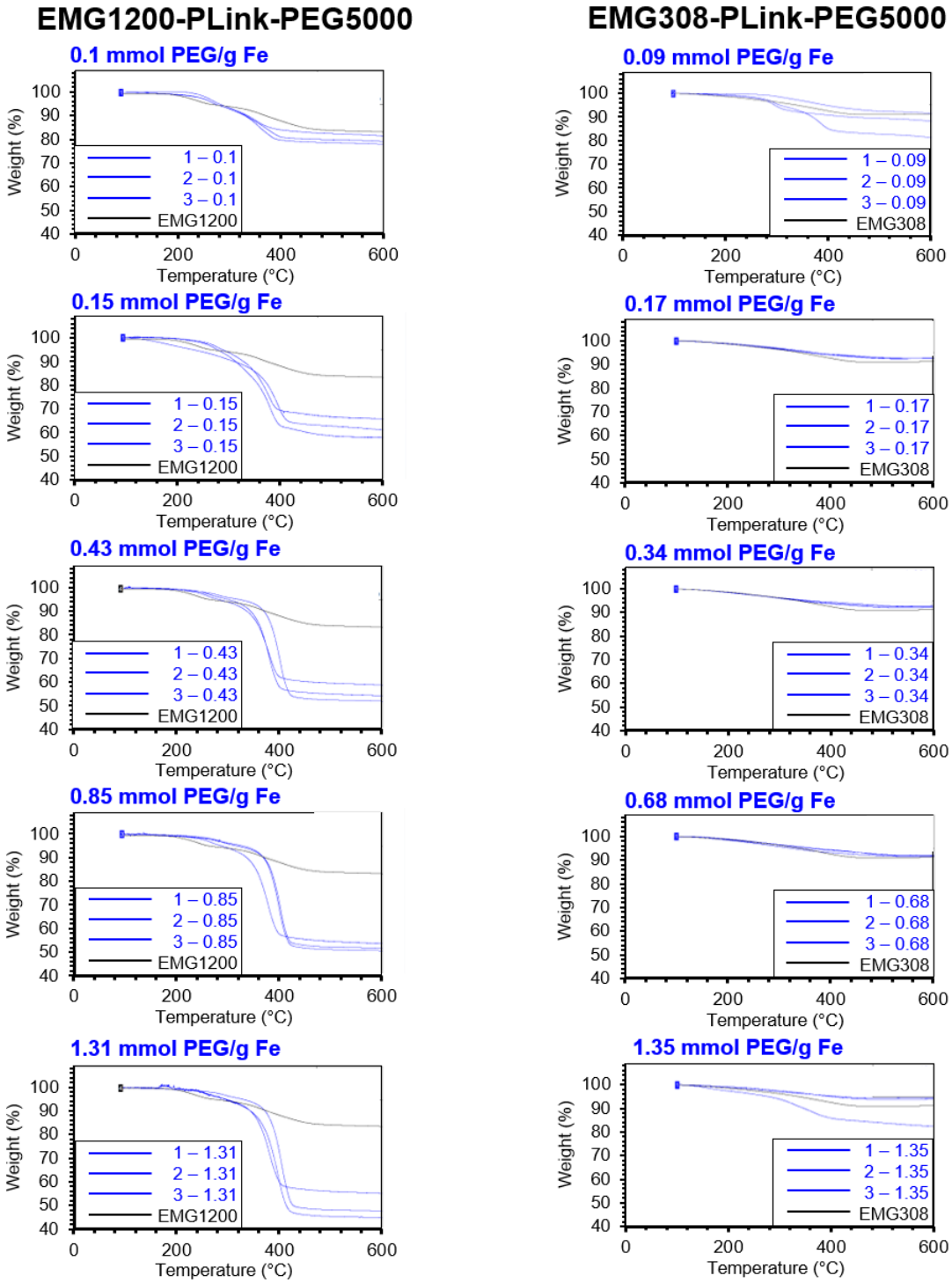

Figure S3.13. TGA data for PLink PEG5000 at various concentrations of PEG coated on IONPs. **Left**. EMG1200; uncoated – black, coated – blue. **Right**. EMG308; uncoated – black, coated – blue.

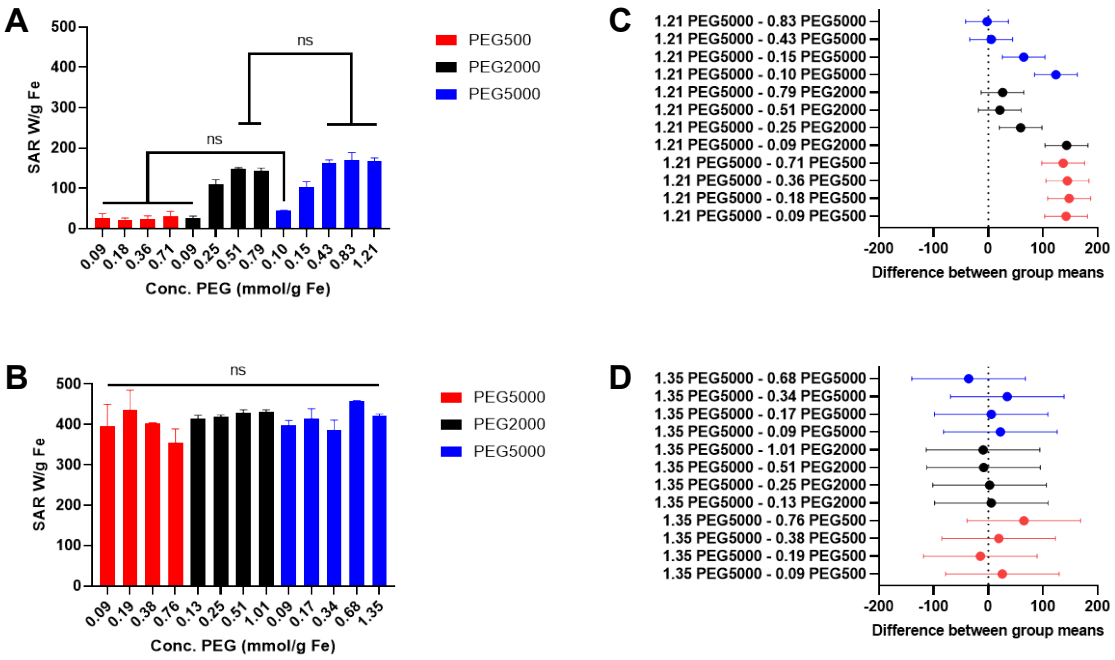

Figure S3.14. SAR in water statistical analysis. Statistical significance was determined by one-way ANOVA. ns denotes no significant difference: **A.** EMG1200 coated with PEG5000 and **B.** EMG308 coated with PEG5000. 95% Confidence Intervals Dunnett where statistically significant difference exists when the interval does not contain zero. **C.** EMG1200 coated with PEG5000 and **D.** EMG308 coated with PEG5000, confidence interval between two means of SAR values compared to a control of PEG5000 at maximum concentration.

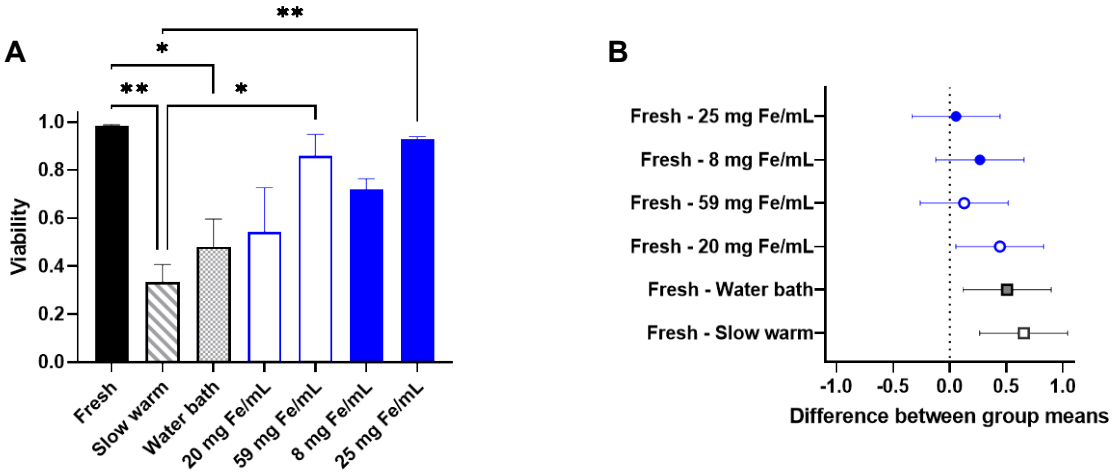

Figure S3.15. Cell cryopreservation rewarming statistical analysis **A**. Statistical significance was determined by one-way ANOVA comparison of all. Significance of P<0.05 denoted by *. Significance of P<0.01 denoted by **. **B** Confidence interval between two means of SAR values compared to a control of Fresh. 95% Confidence Intervals Dunnett where statistically significant difference exists when the interval does not contain zero.

Chapter 4: NMR Characterization of Polyethylene Glycol Conjugates for Nanoparticle Functionalization

This chapter describes the characterization of PEG polymers and conjugation by NMR. This work led to the correct NMR peak identification of ^{1}H-^{13}C NMR coupling in PEG NMR and PEG conjugation yield in coupling reactions. The work in this chapter is reproduced from the planned submission to Bioconjugate Chemistry:

Pasek-Allen, J. L.; Wilharm, R. K.; Pierre, V. C.; Bischof, J. C., Phosphonate NMR Characterization of Polyethylene Glycol Conjugates for Nanoparticle Functionalization, (**2022**)

SUMMARY

The molecular weight, purity, and functionalization of polyethylene glycols are often characterized by 1H NMR spectroscopy. Frequently forgotten, the typical ^{1}H NMR pulse sequence is not ^{13}C decoupled. For large polymers, the ^{13}C-coupled ^{1}H peaks arising from the repeating units have integrations comparable to that of the ^{1}H of the terminal groups. Ignoring this coupling leads to erroneous assignments. Advantageously, once correctly assigned, these ^{13}C-coupled ^{1}H peaks can be used to determine both the molecular weight of the polymer and the efficacy of conjugation of a terminal moiety more accurately than the uncoupled ^{1}H of the repeating unit.

INTRODUCTION

Polyethylene glycols (PEG) are commonly used for the functionalization of biomacromolecules and nanoparticles because their high hydrophilicity increases the dispersion of their cargo in physiological media. Their stability in serum and low immunogenicity are key to their numerous biomedical applications, including several that are FDA approved.[132,133] To increase their dispersion in biological media, metal and metal oxide nanoparticles are typically coated with either polyethylene glycol (PEG) or methyl ether polyethylene glycol (mPEG) of molecular weights ranging between 2000 and 5000 g/mol.[79, 134-135] The length of the polymer affects both the physical properties (e.g., relaxivity)[136] and biological properties (e.g., cell uptake) [137] of the nanoparticles, as does the density of the polymer coating. Particularly for a higher density PEG, a solid anchor to the nanoparticles is required. This anchoring is typically achieved via a functional group appropriate for the nanoparticle following well-established coordination chemistry rules of

hard and soft acids and bases. Since gold is a soft metal, gold nanoparticles are best coated with thiol-terminated PEGs. Hard ligands such as phosphonate and catecholates are best suited for iron oxide nanoparticles (IONPs) that typically consist of iron (III) or mixtures of iron (III) and iron (II) which is a hard metal.[106] Dual imaging modality or drug delivery can often be achieved by conjugating either a luminescent probe or a drug to the second solvent-exposed end of the PEG. The synthesis of such bifunctional PEG requires orthogonal conjugation chemistries that are now well-established.

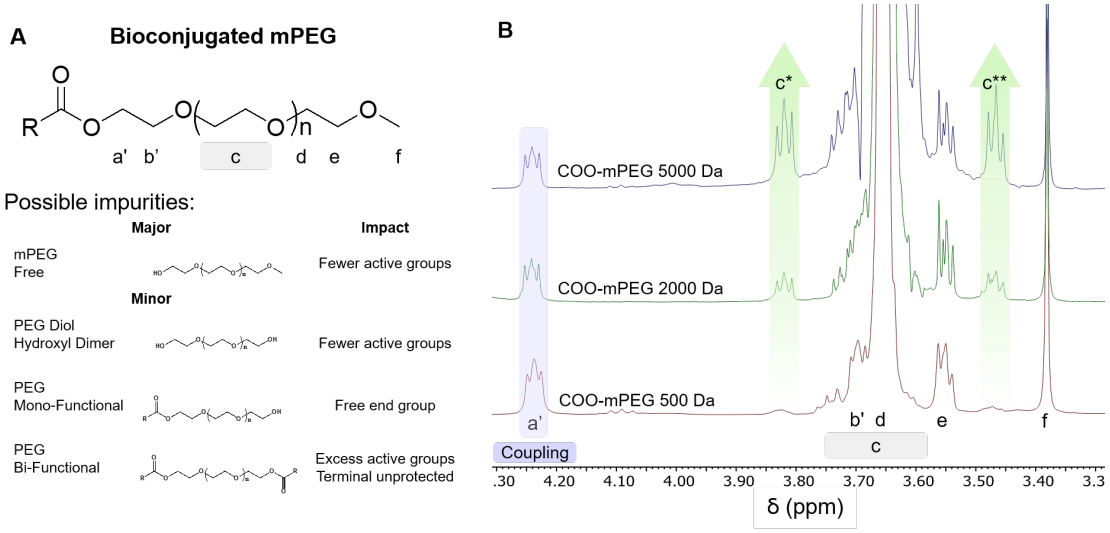

Figure 4.1. Importance of purity of a bioconjugated mPEG product. **A** Pure bioconjugate mPEG and possible impurities from side reactions and manufacturers. **B** ^{1}H NMR spectra at 400MHz, normalized to tetramethyl silane of ester bioconjugated mPEG 500, 2000, and 5000 Da. ^{1}H-^{13}C coupling is observed peaks at 3.47 and 3.82 ppm, which increase with number of repeating units.

Best practices for nanoparticle functionalization require using mono- or di-functionalized PEGs that are pure. Thus, it is important to quantify the amount of functional group per PEG polymer and to identify the presence and ratio of any unfunctionalized PEGs where one or both terminal groups are hydroxyl moieties (Figure 1). Of the different polymer characterization techniques, size exclusion chromatography (SEC) is frequently ill-suited

for such application due to conjugation of an anchoring moiety - often a small thiol or phosphonate group - which results in minor changes in the molecular weight of the macromolecule. Therefore, characterization of modified PEGs often relies on either mass-spectrometry techniques such as electron spray ionization mass spectrometry (ESI MS) or matrix assisted laser desorption ionization (MALDI), as well as ^{1}H nuclear magnetic resonance spectroscopy (^{1}H NMR). It should be noted that since ESI MS is best suited for mass per charge number (m/z) < 1,000, characterization of larger PEGs such as the ones used for nanoparticle functionalization often rely on multiple charged PEGs that carry multiple H^+, Na^+ and/or K^+ ions. Since PEGs have high affinity for alkali ions[138-139], the presence of multiple ion complexes for each m/z can render ESI MS characterization cumbersome. As such, this technique does not necessarily enable accurate and quantitative determination of the presence of unreacted PEGs.

The most common practice is thus to characterize PEG functionalization with small anchoring moieties by ^{1}H NMR.[140-144] Unfortunately, many published ^{1}H NMR of functionalized PEGs are analyzed incorrectly and do not take into consideration the ^{13}C-^{1}H coupling; this leads to erroneous peak assignments and incorrect quantification of PEG functionalization. For this reason, we will explain the correct interpretation of ^{1}H NMR spectra of functionalized PEG.

MATERIALS AND METHODS

Unless otherwise noted, starting materials were obtained from commercial suppliers and used without further purification. Pd-10 column G25 sephadex media were purchased from Global Life Sciences solutions USA LLC.

General characterization

Standard ^{1}H NMR spectra were recorded on a Bruker Avance III HD nanobay AX-400 at 400 MHz. Effect of ^{1}H-^{13}C coupling was studied using a Bruker Avance NEO 600-MHz NMR with TCI cryoprobe at 600 MHz, and on Bruker Avance II+ 400-MHz NMR with BBFO SmartProbe at 400 MHz. ^{1}H-^{13}C decoupling was achieved using the ^{1}H-^{13}C decoupling program WALTZ16 composite pulse decoupling on the Bruker Avance II+ 400-MHz NMR with BBFO SmartProbe. Chemical shifts were referenced to appropriate internal standards. Data for ^{1}H were recorded as follows: chemical shift (d, ppm), multiplicity (s, singlet; d, doublet; t, triplet; m, multiplet) integration, coupling constant. Matrix assisted laser desorption ionization mass spectra (MALDI-MS) were recorded on an Applied Biosystems-Sciex 5800 MALDI/TOF/TOF-MS at the LeClaire-DOW instrumentation facility of the Department of Chemistry of the University of Minnesota using a matrix of α-cyano-4-hydroxycinnamic acid (CCA). Data were processed using Polymerix version 3.01 (Sierre Analytics, Inc., Modesto, Ca, USA). Size exclusion chromatography (SEC): THF-SEC was performed on an Agilent 1260 series instrument (1.0 mL/min, 25 °C). Separation was obtained by a Tosoh Styragel guard column and three successive Tosoh Styragel columns (G6000, G4000, and G2000) packed with 5 μm styrene-divinylbenzene particles. Number-average molecular weight (Mn) were determined using a Wyatt OPTILAB T-rEX refractive index detector (based on a 10-point calibration curve with polystyrene standards).

Bioconjugation of mPEG

The ester coupling to mPEG was synthesized based our small molecule phosphonate linkage method from previous work.[3]

Copied with permission: "(PEG-4-oxobutyl)phosphonic acid: ^{1}H NMR (400 MHz, $CDCl_3$) δ 4.27 (t, 2H), 3.66 (m, 180H), 3.57 (t, 2H), 3.40 (s, 2H), 2.51 (t, J = 7.1 Hz, 2H), 2.07 – 1.92 (m, 2H), 1.90 – 1.76 (m, 2H). ^{13}C NMR (101 MHz, $CDCl_3$) δ 173.20 (s, 1C), 71.94 (s, 1C), 70.57 (s, 1C), 69.11 (s, 1C), 63.59 (s, 1C), 59.04 (s, 1C), 34.17 (d, J = 15.9 Hz, 1C), 24.93 (d, J = 141.8 Hz, 1C), 18.12 (d, J = 4.8 Hz, 1C). ^{31}P NMR (162 MHz, $CDCl_3$) δ 31.15 (s, 1P)."

Dilution of coupled mPEG with free mPEG

Two stock solutions were made using 3.75 mL of $CDCl_3$ added to coupled mPEG2000 (**(PEG-4-oxobutyl)phosphonic acid)** (57 mg, 0.026 mmol) or free mPEG2000 (57 mg, 0.028 mmol). Dilutions were created by adding 0, 300, 600, 900 or 1200 µL of coupled PEG solution to 1200, 900, 600, 300, or 0 µL free PEG solutions to make 0, 25, 50, 75 and 100% coupled PEG solutions, respectively.

RESULTS AND DISCUSSION

Correct assignment of ^{1}H NMR spectra of functionalized poly(ethylene glycol) polymers

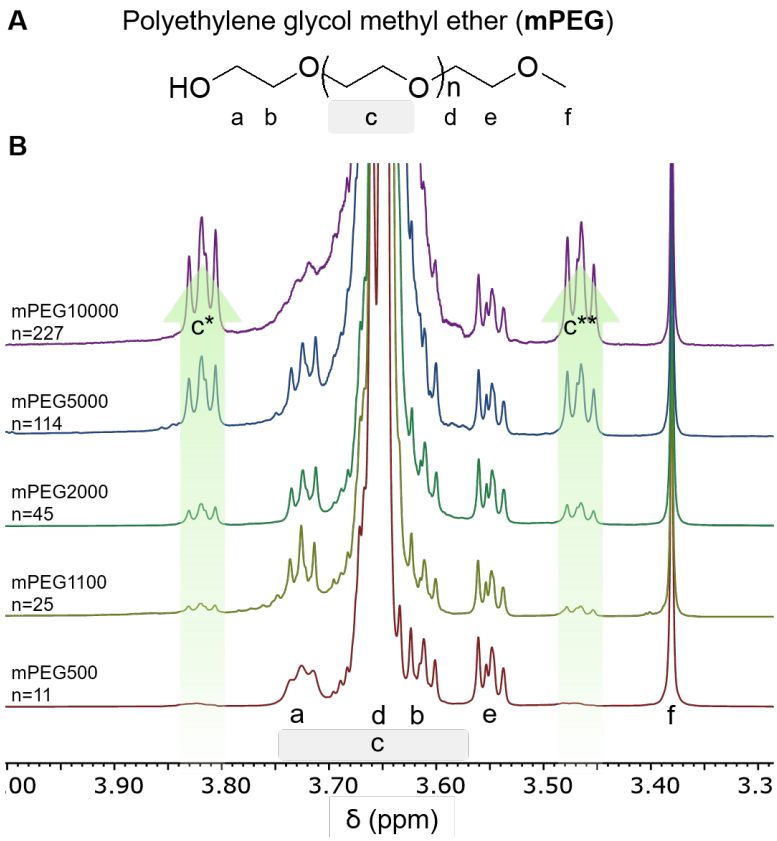

Figure 4.2. mPEG by MW **A.** Chemical structure of mPEG with end groups, and main polymer block protons labeled for reference. **B.** Formula to calculate the correct relative integration of c* and c** peaks based on the MW or the main polymer – c peak. **C.** ^{1}H NMR spectra (400 MHz, $CDCl_3$) normalized to tetramethyl silane stack of mPEGs with MW from 500 to 10000 Da. The integration of the ^{1}H - ^{13}C coupling peaks c* and c** increase with MW but resolution of a and b peaks decrease.

Frequently forgotten, the pulse sequence typically used for 1-dimensional ^{1}H NMR spectroscopy is not ^{13}C decoupled. Naturally occurring carbon is present as 1.1% ^{13}C, an NMR active nuclei with spin ½ that does couple with neighboring non-equivalent ^{1}H, splitting its peak in a standard ^{1}H NMR experiment. Given the gyromagnetic ratio of ^{13}C, this splitting results in two smaller peaks that are 115-140 Hz apart for a sp^3-hybridized C. Each of those side peaks has an integration of 0.55% of the main peak. For most small molecules, this splitting is inconsequential and is usually ignored. However, the ^{1}H-^{13}C coupling becomes significant when analyzing functionalization of large polymers such as

PEG with one functionalized terminal group given that the ratio of terminal group to repeating polymer unit is typically to 2 to 0.9% (for 2000 and 5000 g/mol PEG, respectively). Thus for a 5000 g/mol PEG, the integration of the ^{1}H signal of a CH_2 from the terminal (functionalized) group is close to that of the side bands due to the ^{1}H-^{13}C coupling of the repeating CH_2-CH_2-O unit. Because of the similarity in chemical shifts, researchers may erroneously assign the signal of the CH_2 of the terminal group to the ^{1}H-^{13}C coupling peaks of the PEG (peaks c* and c** in Figure 1B) and consequently misjudge the purity of the polymer and conjugation efficacy.

The significance of the ^{1}H-^{13}C coupling on the interpretation of one-dimensional ^{1}H NMR spectra is exemplified in the spectra of mPEG of different molecular weight in deuterated chloroform. The chemical structure of mPEG and the labels used in this discussion are shown in Figure 2A. Note that mPEG is terminated with an alcohol on one end and a methyl group on the other end. In the absence of ^{1}H-^{13}C coupling, these polymers would be anticipated to display six signals in their ^{1}H NMR spectra: the *a*, *b*, *d*, and *e* O-CH_2 proton would each be triplets, whereas *c* would be a broad peak and *f* would be a singlet. The experimental ^{1}H NMR spectra of 5 mPEGs of different molecular weight (500, 1000, 2000, 5000, and 10000) are shown in Figure 2B. Assigning the leftmost triplet to protons *a*, the small triplet adjacent to the right of the major peak as those of protons *b*, and the protons *e* adjacent on the left to the singlet corresponding to the protons *f* are typical pitfalls. Alternatively, the triplets adjacent to the left and right of the major peaks have also been assigned to protons *b* and *d*. However, such assignments[132, 141-144] are incorrect.

As shown in Figure 2, the integration of the peaks *c** and *c*** both increase with increasing PEG molecular weight. The central peak *c*, which corresponds to the repeating

monomer, broadens and eventually overlaps with the triplets *a* and *b* as the molecular weight of the polymer increases. This is to be expected since transverse relaxation time, and thus line broadening, increases with increasing rotational correlation time and polymer size. The two peaks at 3.47 ppm and 3.82 ppm, whose integration relative to the singlet of the protons *f* at 3.37 ppm increases with increasing PEG MW, are not due to impurities. The two peaks are the results of ^{1}H-^{13}C coupling of the naturally occurring 1.1% ^{13}C$^{1}H_2$-O protons of the polymer repeating unit. This ^{1}H-^{13}C coupling contains other signature elements in the ^{1}H NMR spectra. For PEG, ^{1}H-^{13}C coupling creates two identical peaks at positioned +/- 70 Hz from the central peak. Since the two side peaks correspond to ^{13}C$^{1}H_2$ while the central peak corresponds to ^{12}C$^{1}H_2$, the integration of the two side peaks always adds up to 1.1% that of the central peak. This is in accordance with the naturally occurring ratio of ^{13}C. Lastly, the splitting pattern of each ^{1}H-^{13}C coupled peak, which arises from ^{1}H-^{1}H coupling, is identical to that of the central ^{12}C$^{1}H_2$ peak. As can be seen in Figure 2, for large polymers of 5000 or 10000 g/mol, these side peaks arising from ^{1}H-^{13}C coupling have similar integration to the CH_3 protons of the terminal methyl group. Their ratio can be calculated from the equation shown below.

$$\int c^{*} + \int c^{**} = 1.1\% \int c$$

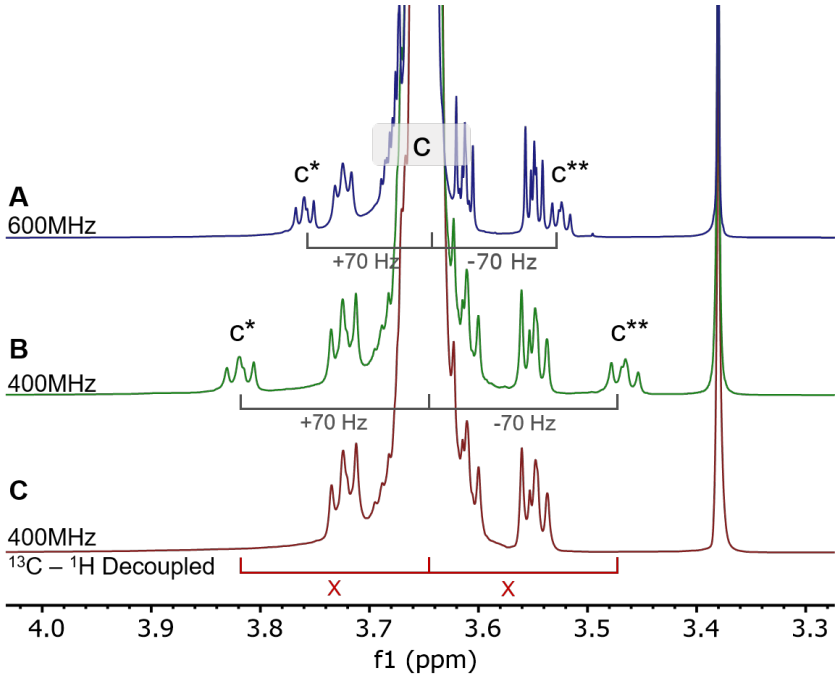

Figure 4.3. Effects of 1H-13C coupling in NMR spectra of mPEG 2000 Da. Refer back to figure 1 for labeling **A**: ^{1}H – ^{13}C decoupled spectra - c* and c** peaks are canceled. **B:** 600 MHz NMR spectra - c* (3.76 δ) and c**(3.53 δ) peaks are ± 0.115 ppm (70Hz δ) from c peak. **C:** 400 MHz NMR spectra c* (3.82 δ) and c** (3.47 δ) peaks are ± 0.175 ppm (70Hz δ) from main polymer - c peak. NMR spectra are normalized to tetramethyl silane.

Coupling constants (*J*), unlike chemical shifts, are measured in Hz. Their values in Hz are independent of the magnetic field of the NMR spectrometer. Therefore, their chemical shift (δ) will vary with magnetic field. As demonstrated by Harrel, side peaks due to ^{1}H-^{13}C couplings can be distinguished from peaks arising from chemical impurities by taking the spectra at two different magnetic fields.[143] This is exemplified with the ^{1}H NMR spectra of a 2000 MW mPEG measured at 400 and 600 MHz in Figure 3. Regardless of the magnetic field, the ^{13}C-^{1}H coupled peaks of CH_2-O are always 70 Hz upfield and downfield from the main peak. At 600 MHz, this translates to a difference of +/- 0.12 ppm; this difference is greater (0.19 ppm) at a lower magnetic field (400 MHz). Alternatively, if one uses a ^{13}C-^{1}H decoupled pulse sequence (Figure 3C), both side peaks disappear.

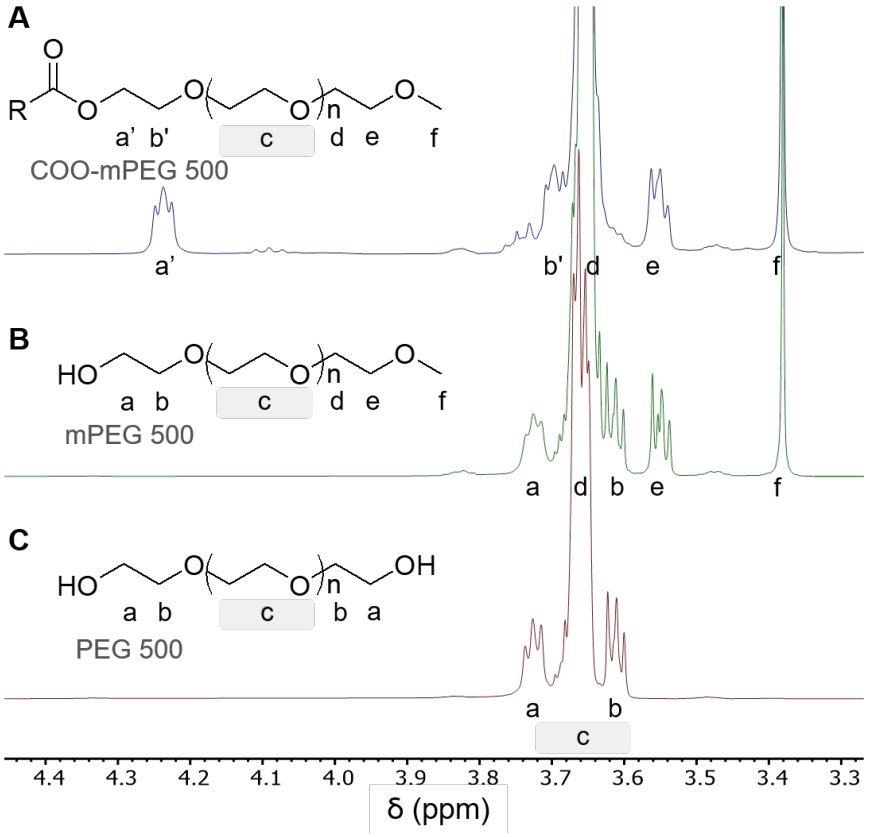

Figure 4.4. PEG conjugation. Area of interest ^{1}H NMR (400 MHz, $CDCl_3$) NMR spectra (3.30-4.40ppm) for PEG 500 Da with various end groups, normalized to tetramethyl silane. **A**. structure of mPEG500 with ester functionalization of terminal end group and relevant NMR range. R group is shown in Figure 6B. **B.** structure of mPEG500 with alcohol functionalization of terminal end group and relevant NMR range. **C.** structure of PEG500 with Diol functionalization of terminal end groups and relevant NMR range. a is CH_2 adject to alcohol, b is an ether CH_2 adject to a, c is repeating monomer of CH_2 ethers, d is an ether CH_2 adject to e, e peak is terminal ether CH_2, f peak is terminal methyl group CH_3. a' and b' are the conjugated 'a' and 'b' CH_2's coupled to ester.

Taking the above into consideration, correct ^{1}H NMR assignments for PEG, mPEG, and a typical mono-functionalized chemical structure are shown in Figure 6B, and for mPEG are shown in Figure 4. In the case of mPEG, the triplet corresponding to the terminal C*H*$_2$-O group appears at 3.60 ppm while that of the terminal C*H*$_3$ group appears at 3.58 ppm. Note the overlap of the signal of the *d* protons with that of the *c* protons. Further addition of a functional group via the formation of an ester shifts the triplet corresponding to the protons

a' and *b'* downfield by 0.51 and 0.08 ppm, respectively. Note that in this case, the triplet corresponding to the *a* protons of compound B at 3.72 ppm did not fully disappear, indicating that conjugation (formation of the ester) was not quantitative.

Comparing NMR, MS and SEC techniques to determine the molecular weight of mPEG

Correct assignment of ^{1}H NMR spectra is key to correct determination of the molecular weight of functionalized PEGs. Once this is accomplished, the MW of the PEG can be determined by comparing the integration of the singlet of the methyl group (signal corresponding to the protons *f*) to either that of the c signal corresponding to the repeating monomer unit (*NMR c* in Figure 5) or to the ^{13}C-^{1}H coupled peaks of the CH_2-O monomer (*c** or *c*** signal in Figure 2, NMR *c*** in Figure 5).

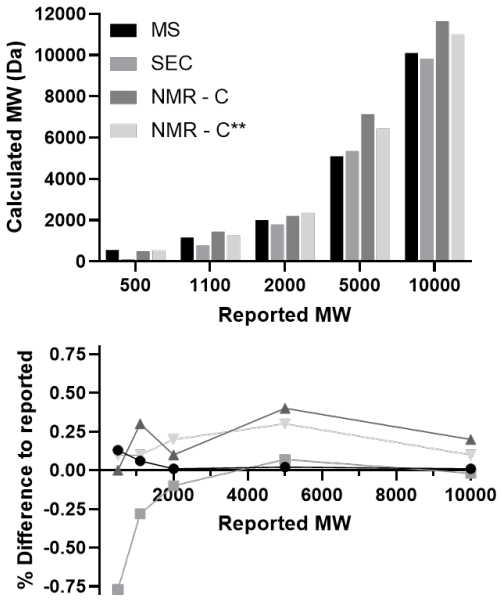

Figure 4.5. MW calculation comparison. The MW of mPEG was calculated using the three common techniques SEC, MS, and NMR normalizing F=3 using integration of main polymer – c peak, and NMR normalizing from c**=0.55c. A set of five commercial mPEG MWs (500, 1100, 2000, 5000, and 10000 Da, fig 3 bottom) were chosen due to lab availability. Reported MW is what is commercially advertised. **Top:** Values determined, **Bottom:** Difference of values to reported based on MW.

Most commonly cited in the literature is the first method. Advantageously, the second method compares two integrations that are closer in values (see supporting information for a more in-depth discussion on calculating MW with other NMR signals). Each method was

compared to both MS and SEC for commercial mPEG polymers ranging in size between 500 and 10 000 g/mol.

As shown in Figure 5, values determined by either SEC or MS technique are lower than the common NMR method, which compares integration of the terminal methyl group to the protons *c* of the $^{12}C^{1}H_2$-O to calculate MW. In contrast, except for the largest polymer, comparing the integration of the terminal methyl group to the integration of either *c** or *c*** corresponding to the $^{13}C^{1}H_2$-O (the ^{13}C coupled ^{1}H peak of the repeating unit) yields MW that are within error the same as those obtained by either SEC or MS. Advantageously, ^{13}C coupling of ^{1}H signals can be exploited to easily and more accurately determine the molecular weight of mPEG and functionalized mPEGs. Of note in this case, the *c** peak is better resolved and therefore gives more accurate results than the *c*** peak, thereby highlighting the necessity to use NMR peaks that are clearly resolved for MW calculations.

Quantifying conjugation yield and purity of functionalized PEGs

Nanoparticle coating and biomacromolecule conjugation requires PEGs that are further functionalized with either a small anchoring group (e.g., carboxylate, phosphonate, amine, thiol) or a reactive group. These PEGs are typically achieved by conjugating a small molecule with the necessary orthogonal functional or reactive group. Since such conjugation leads to small changes in molecular weight and polarity, purification of such functionalized PEGs is difficult and is not always performed. Thus, the determination of the yield of the PEG functionalization is important. Although feasible, determination of the purity of functionalized PEGs by SEC requires refractive index, and two wavelength channels are used in conjunction with a complex system of linear regressions in purity and

polydispersity. Therefore, it is significantly easier to determine the yield of conjugation and polymer purity by ^{1}H NMR spectroscopy.

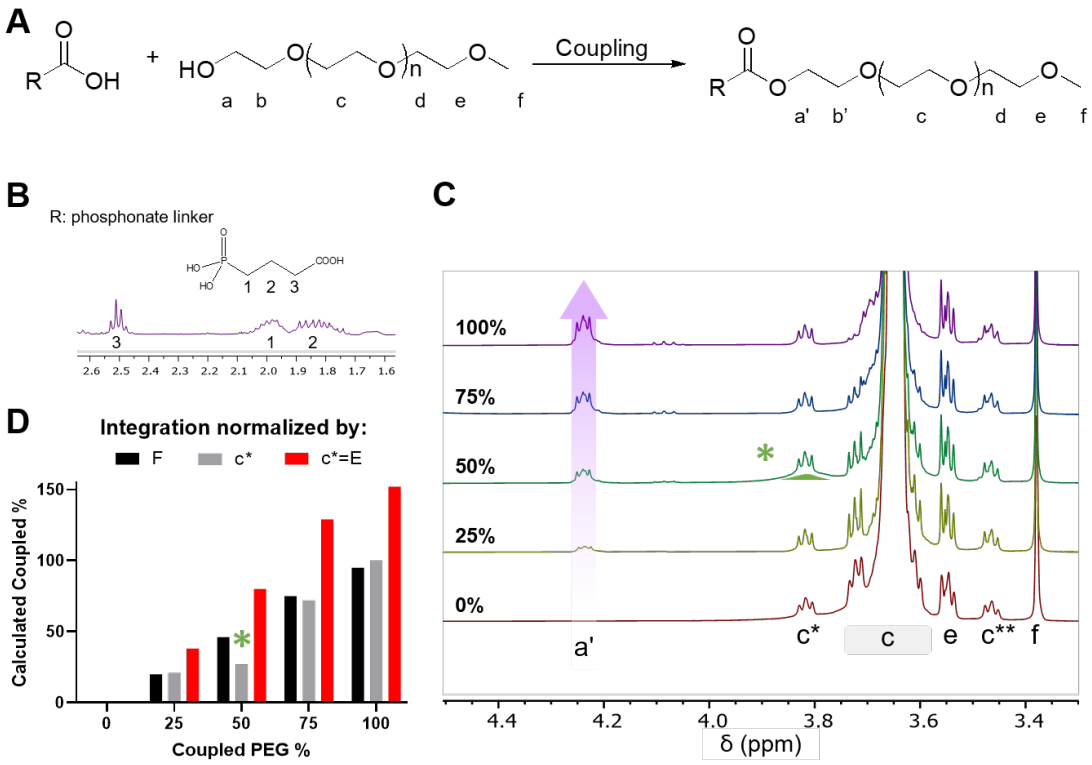

Figure 4.6. Dilution of coupled mPEG. A. Scheme of coupling ester to mPEG 2000. **B.** structure of ester linker and area of interest ^{1}H NMR (400 MHz, $CDCl_3$) NMR spectra (3.30-4.40ppm). **C.** Dilution of coupled mPEG2000 with free mPEG2000 ^{1}H NMR (400 MHz, $CDCl_3$) NMR spectra (3.30-4.40ppm) from 100-0% coupling, normalized to tetramethyl silane. **D.** Calculated % coupled amount based on normalization by F=3, E=2, c**= 0.55% C (mPEG 2000 c**=1), or the misinterpretation of c**=E=2.

In the example shown in Figure 4A, conjugation of a carboxylate to the alcohol via an ester linkage shifts the peak *a'* downfield by 0.51 ppm. The signal from *a'* is resolved sufficiently from the other peaks of the polymer so that it can be accurately integrated. Thus, the conjugation yield can be determined by comparing the integration of that peak to that of a second, well-resolved peak that does not shift upon conjugation. As outlined above, more accurate results are obtained if these two peaks have similar integration. In

the case of functionalized mPEG, such as compound B in Figure 6, the reference peak can either be the protons *f* of the methyl group or the protons *c** or *c*** corresponding to the $^{13}C^{1}H_2$-O (the ^{13}C coupled ^{1}H peak of the repeating unit). As noted above, the *c** and *c*** peaks, if well-defined, are very accurate for such calculations but only if they are interpreted correctly as belonging to the polymer repeating unit.

The ease of this ^{1}H NMR technique was demonstrated with mono-functionalized mPEG (Figure 6A). In this case, the mPEG was conjugated to a phosphonate (Figure 6B), which we previously demonstrated to be an excellent anchoring group for iron oxide nanoparticles.[3, 106] To document this technique's ability to determine purity of functionalized PEGs, the ^{1}H NMR spectra of the purified phosphonate linker, PLink-PEG2000, was recorded in the presence of increasing concentration of mPEG2000 (Figure 6C). In each case, the purity of the PLink polymer was determined by comparing the integration of the CH_2 of the phosphonate linker to either the methyl protons *f* or the $^{13}C^{1}H_2$-O of the polymer repeating unit. The results were compared to those obtained by SEC and MS (see Figure S11). In each case, normalizing the spectra to the correct integration of *c***=1 (0.0055 × 2000 Da/44 × 4 protons) consistently gave accurate purity levels. Interestingly, normalizing the spectra to the methyl protons *f* was far less accurate (Figure 6D).

CONCLUSION

^{1}H NMR is a powerful technique to characterize the molecular weight, purity, and functionalization of polyethylene glycols. However, accurate interpretation requires acknowledgement that the fraction of terminal group to repeating monomer unit is small. As such, unless a ^{13}C decoupled ^{1}H pulse sequence is used, one cannot ignore the 1.1%

natural abundance of carbon-13 in standard one-dimensional ^{1}H NMR spectra, which is standard for all polymers. Advantageously, if identified correctly, coupling of ^{13}C to the two ^{1}H of the repeating CH_2 groups of the polymers gives an excellent chemical handle to calculate both the molecular weight and the conjugation efficacy of the polymer with greater accuracy and ease than SEC and MS. Furthermore, this method can be used for protonated polymers other than PEG.

SUPPORTING INFORMATION

Full NMR spectra:

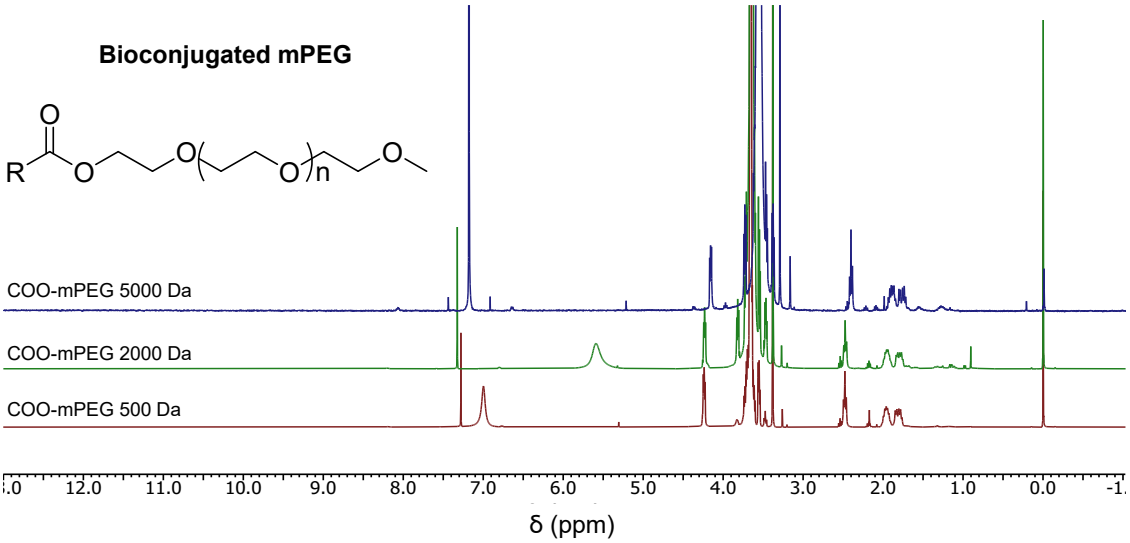

Figure S4.1. Full ^{1}H NMR spectra of ester mPEG stack.

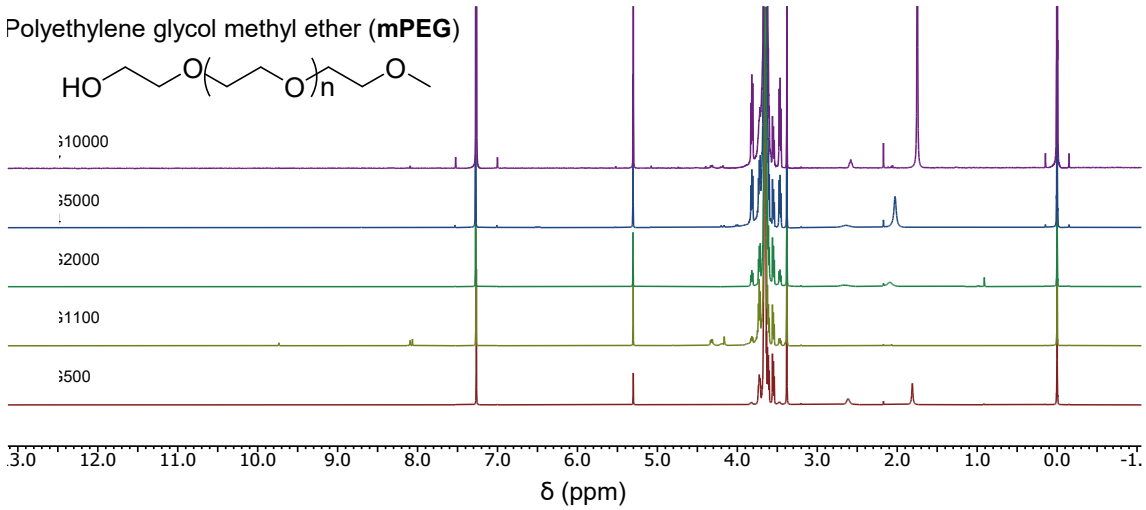

Figure S4.2. Full ^{1}H NMR spectra of mPEG MW stack

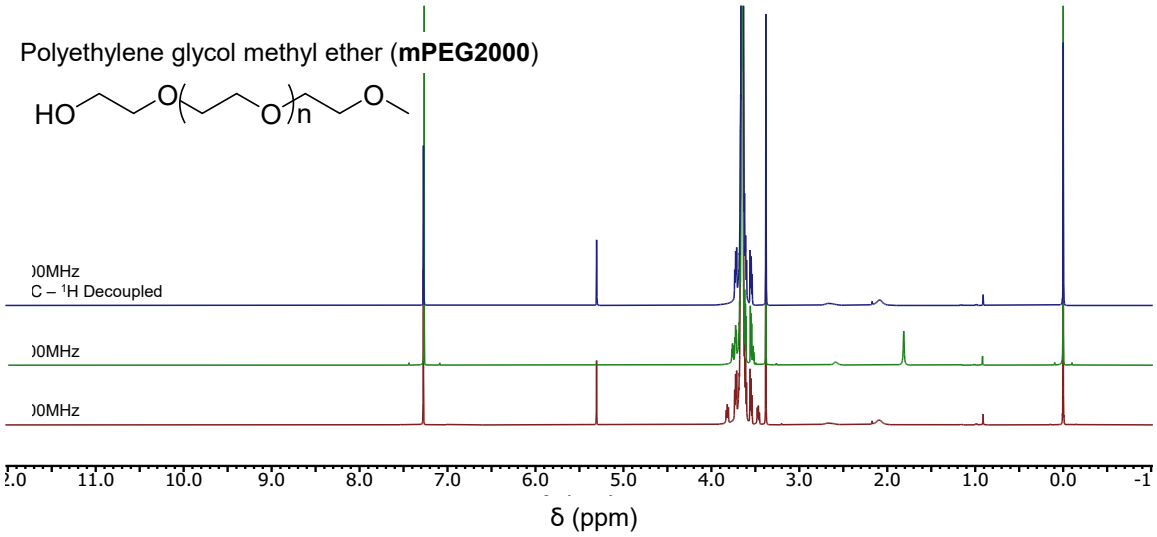

Figure S4.3. Full ^{1}H NMR spectra of mPEG ^{1}H-^{13}C decoupling determination.

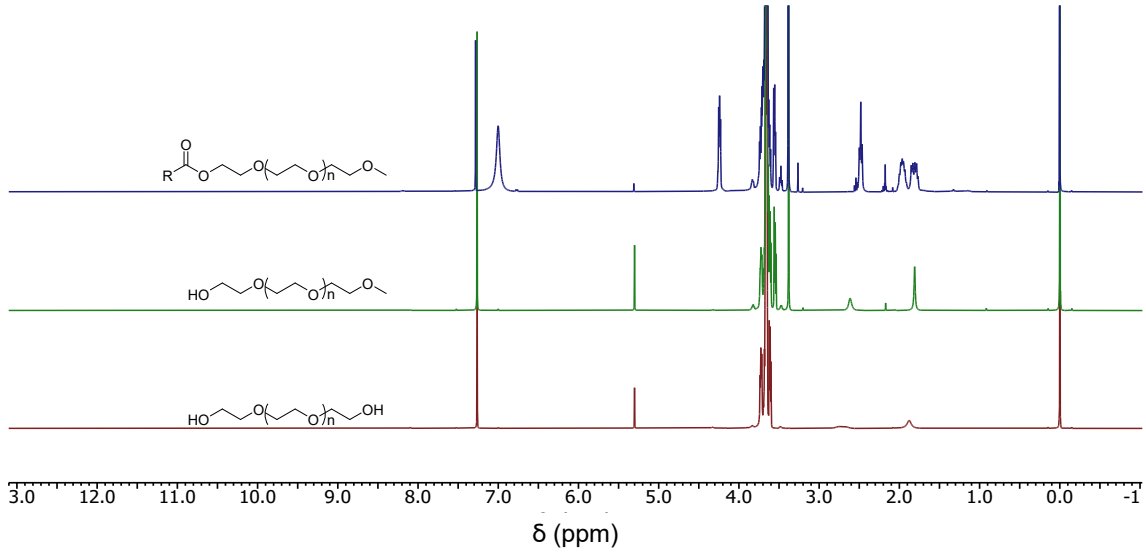

Figure S4.4. Full ^{1}H NMR spectra of mPEG peak identification.

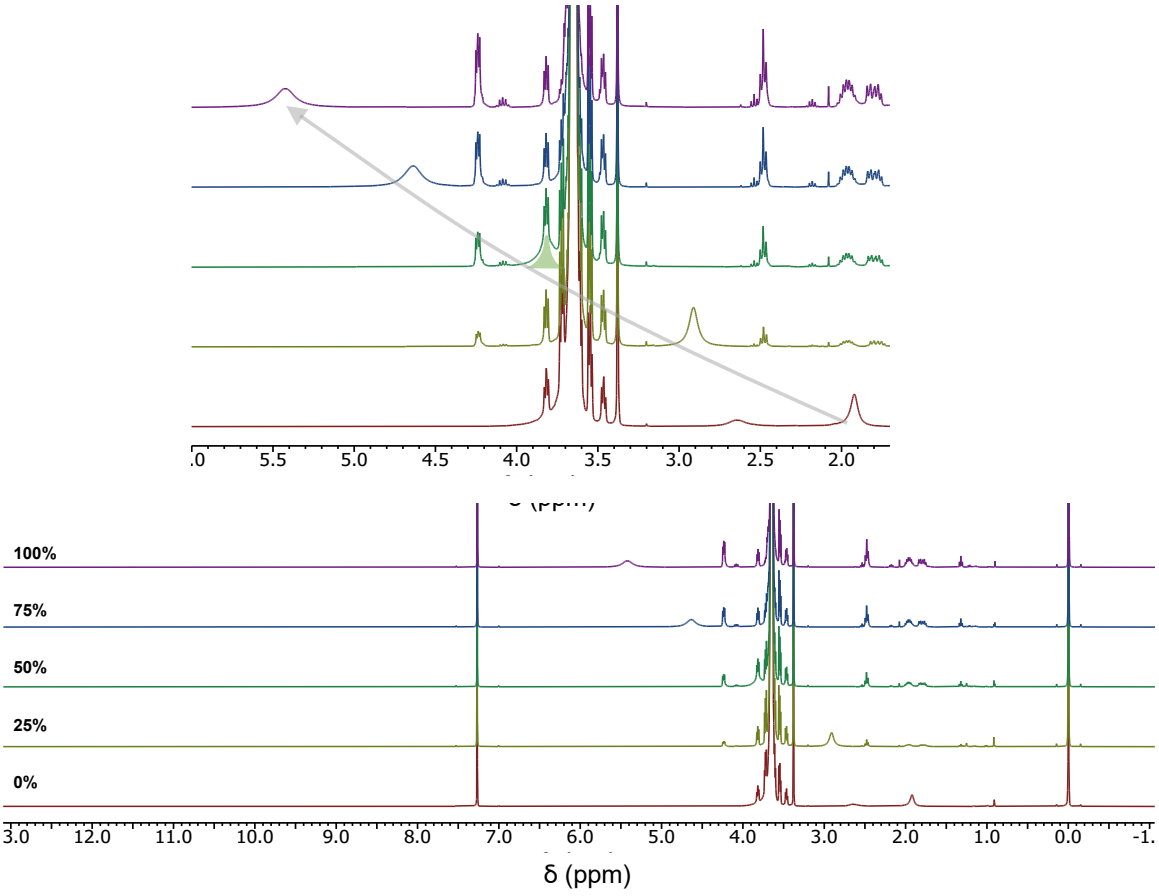

Figure S4.5. 1H NMR spectra of ester mPEG dilution with free PEG. 100% is purified coupled mPEG2000, 0% is commercial mPEG2000. **A.** Zoomed in ^{1}H NMR spectra of dilutions, grey arrow depicts movement of mPEG alcohol peak with increased coupling. Green star and green shading depict overlap of PEG alcohol peak with c* peak. The alcohol peak may overlap with PEG peaks depending on concentration and coupling percentage. **B.** Full spectra of A.

MW comparison

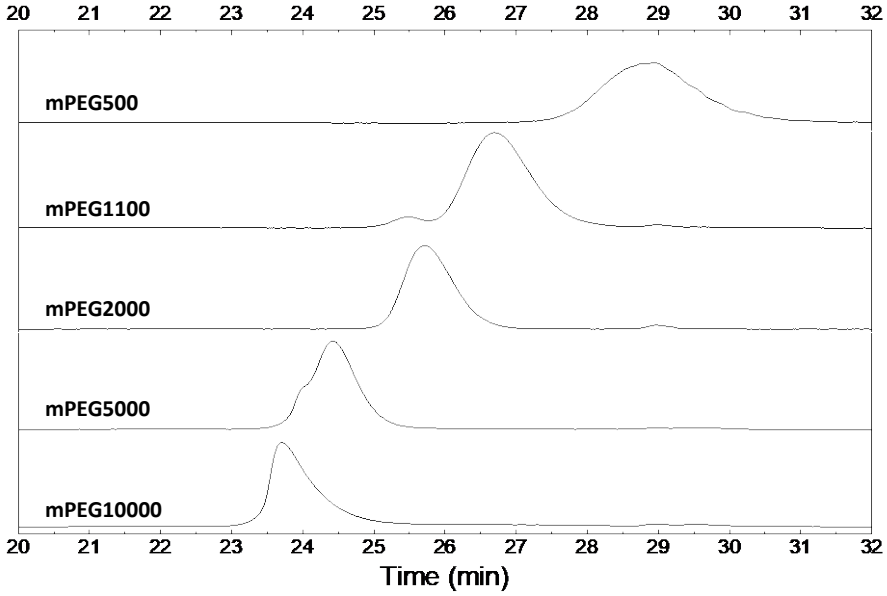

Figure S4.6. SEC chromatograms of mPEG (in THF). Secondary unresolved peaks in PEG 1100 and PEG 5000 are likely due to smaller PEG chains formed during synthesis and not removed during purification.

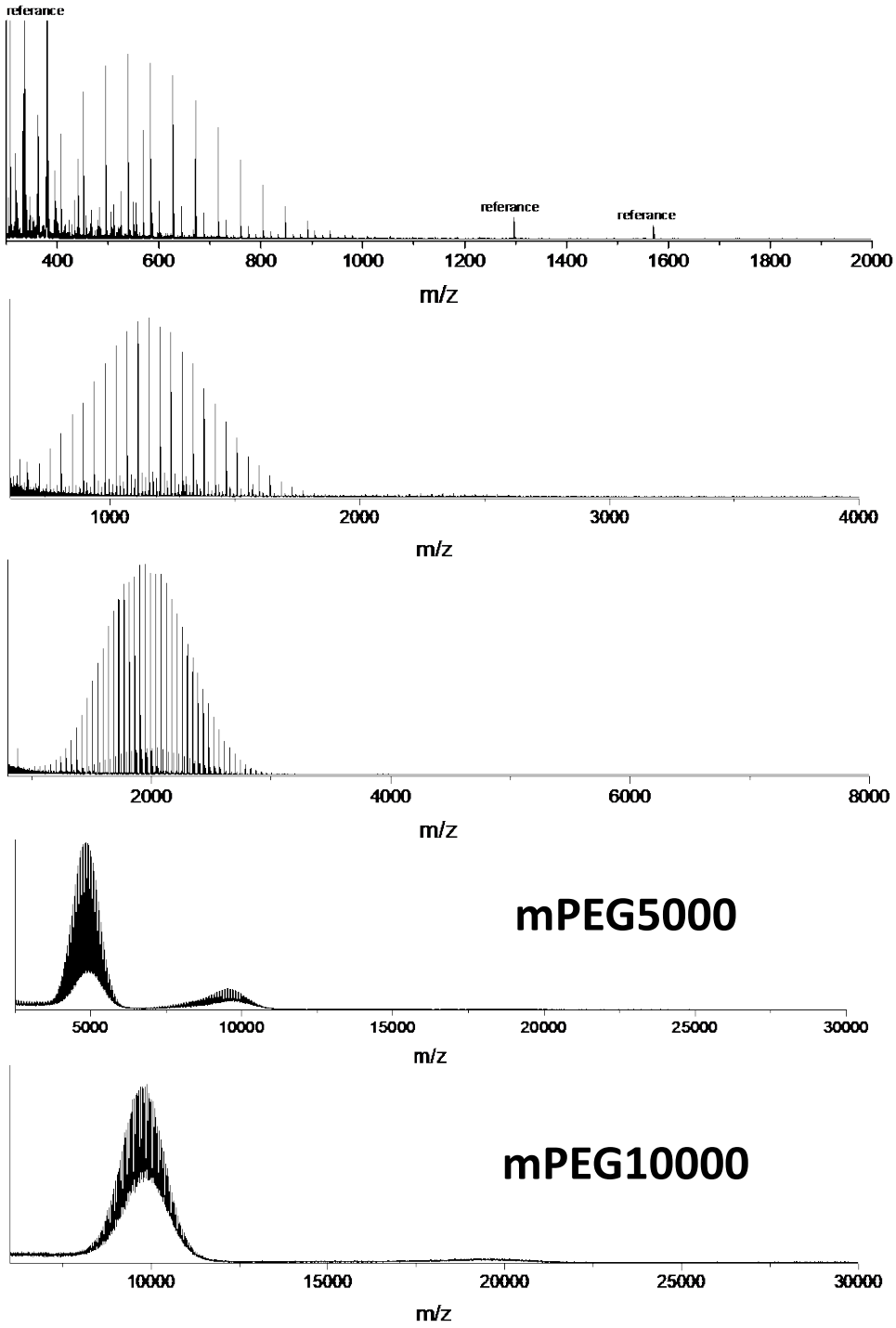

Figure S4.7. MALDI-MS spectra of mPEG. Internal reference peaks at 307 m/z, 379 m/z, 1297 m/z and 1571 m/z were not included in M_n calculations. (MS work was completed by Randall Wilharm)

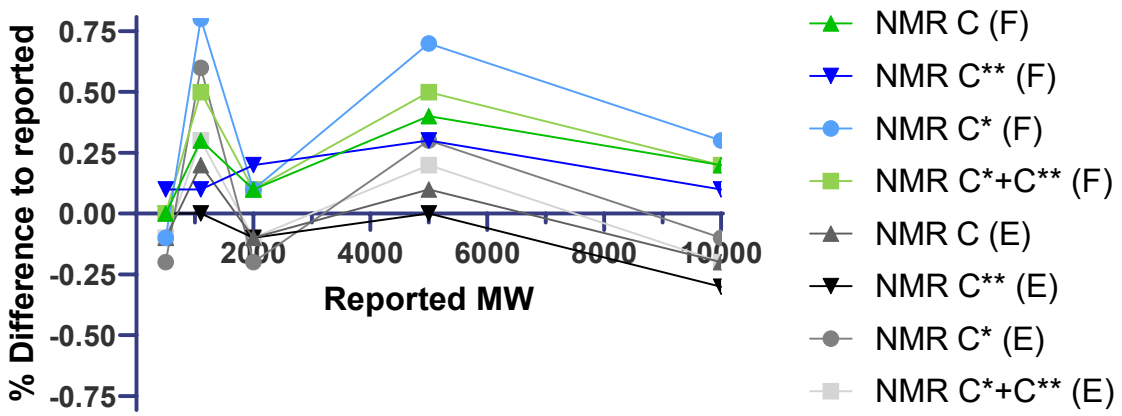

Figure S4.8. 1H NMR mPEG MW determination normalizing to various peaks and calculating MW from c or c* peaks. There is a large discrepancy between normalizing with either the "f" or "e" peak and the reported amount. The "f" peak may overestimate the MW of mPEG if there is some PEG diol as an impurity. The "e" peak would have similar issue except that at larger MW the main peak starts to overlap and increase the integral, resulting in an under estimation of the MW. Additionally, the c* and c** method agreed with the normalization methods closely.

Coupling Dilution comparison

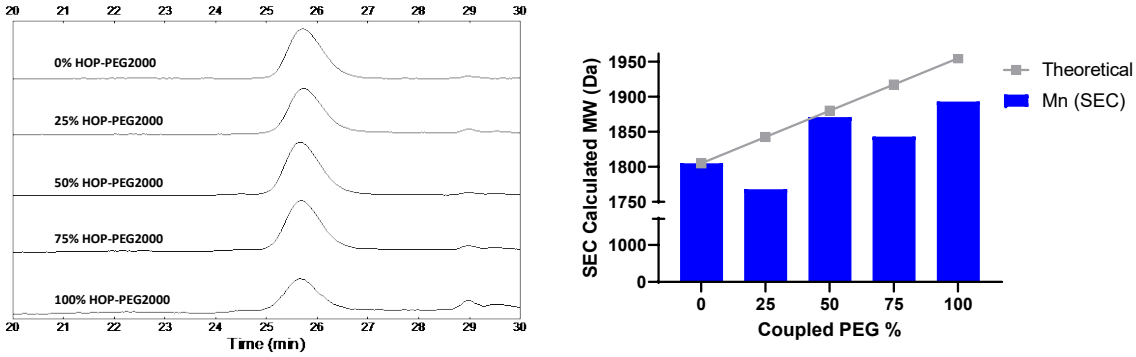

Figure S4.9.SEC analysis of coupling PEG A. SEC chromatograms of mPEG2000 diluted with HOP-PEG2000 (in THF). **B**. MW of coupled PEG dilution using SEC, blue bars showing the calculated values, grey line showing theoretical MW based on phosphate linker of 150 Da and the percentage added.

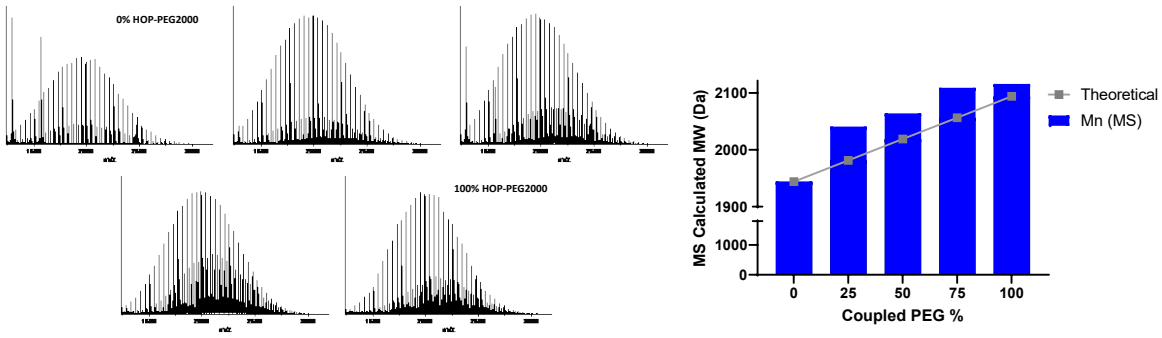

Figure S4.10. MS analysis of coupling PEG A. MALDI-MS spectra for samples of mPEG2000 diluted with HOP-PEG2000. Internal reference peaks at 1297 m/z, 1571 m/z and 2466 m/z were not included in M_n calculations. **B**. MW of coupled PEG dilution using MS, blue bars showing the calculated values, grey line showing theoretical MW based on phosphate linker of 150 Da and the percentage added.

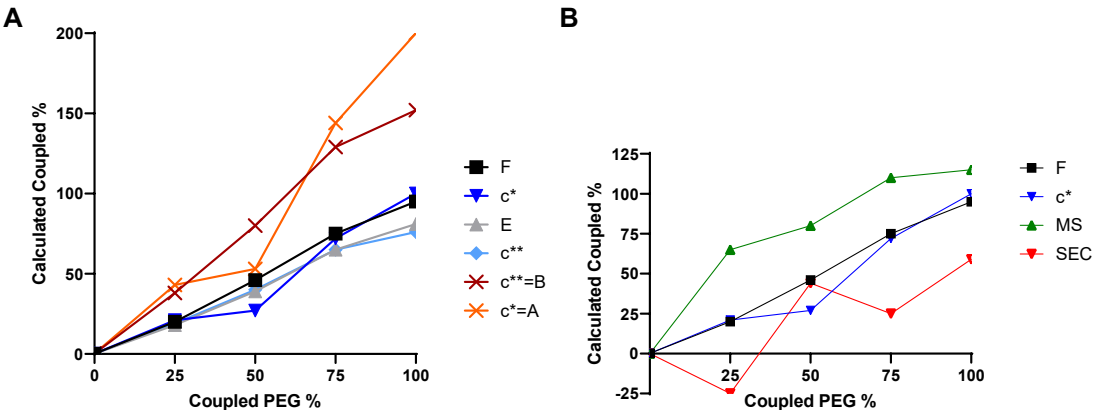

Figure S4.11. Comparison of NMR, SEC, and MS of coupling. A. Coupling calculated by ^{1}H NMR by using various peaks to normalize the spectra, compared to misidentifying c* and c** peaks as end groups. **B.** Coupling calculated based on MW determined by SEC (fig s9) or MS (fig s10) compared to using ^{1}H NMR normalized by either methyl peak or c* peak.

Discussion on determining yield coupled PEG

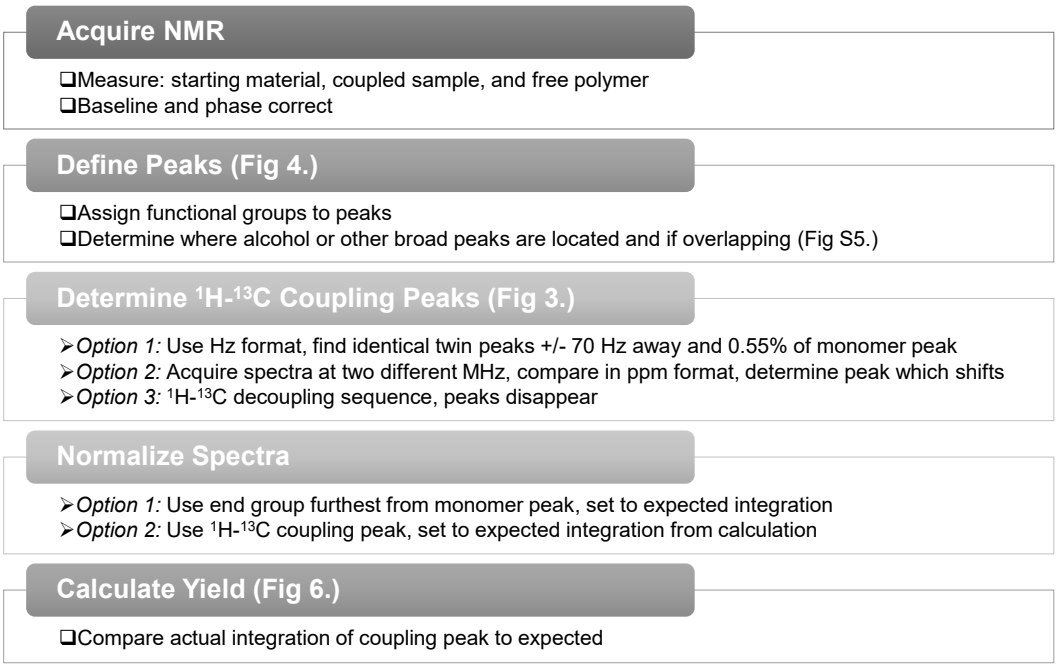

Figure S4.12. Flow chart to correctly find coupling yield.

Taking ^{1}H NMR using approximately 20 mg /mL of sample on each starting material, coupled sample, and free polymer will give a starting point understanding of which peaks are created or removed during coupling, similar to Figure S5 0% and 100%. This comparison can also be used to understand the left-over terminal groups of the polymer, which are not affected by coupling. If a broad peak is observed in the free polymer sample but not in coupled sample, it is possible the peak is overlapping with another peak, as in Figure S5 50%. Increasing or decreasing the concentration of the material may change the position of the peak. Alternatively, one can analytically (ensuring total polymer concentration remains constant) dilute the coupled sample with known amounts of free polymer, such as in Figure S5, and trace the overlap back to the approximate location in the initial sample. The large polymer peaks can be identified by the magnitude and

chemical shift. ^{1}H-^{13}C coupling peaks need to be identified so as to not be misconstrued as terminal monomers, as they both mimic the monomer peak shape and are close to the polymer shifts, but do not integrate as such. This can be done in various ways; two ways are illustrated in Figures 2 and 3. The simplest way is to view spectra in absolute frequency (Hz) where the ^{1}H-^{13}C coupling peaks will be exactly +/- 70 Hz from main polymer peak with integration of 0.0055 of it. Using the same sample on an instrument with a different frequency will allow comparison of the two spectra in ppm format. The ^{1}H-^{13}C coupling peaks will shift based on the MHz of the instrument (70Hz/instrument MHz = ppm shift). A ^{1}H-^{13}C decoupling pulse sequence after the initial scan can also be used, and the twin peaks will be removed. Finally, the ^{1}H NMR spectra of a sample polymer with a larger MW can be compared to the spectra of the original sample. After successfully identifying all peaks, the next step is to normalize the spectra.

The ^{1}H NMR spectra can be normalized to any peak by identifying an integration range and setting it to the expected values or number of protons. To determine coupling yield of a polymer to another compound, it is best to normalize with a peak related to the polymer but with the least interference from the main polymer peak. Generally, this will be the end group peak furthest from the main polymer peak unless it is overlapping with an alcohol or other broad peak. Any peak that has overlap interference from a broad peak, such as in Figure S5 50%, should not be used to normalize. The absolute integration of the peak will be increased from the addition of the broad peak and will result in lowered integration and lower calculated yield. If the next furthest peak is a ^{1}H-^{13}C coupling peak, integration should be set to 0.0055 of the main polymer peak (equation below). $Mw_{polymer}$ can be determined by GPC (MW above 2000), MS, or NMR.

$$\int c = \#protons_{monomer} * \frac{MWpolymer - MWendgroup}{MWmonomer}$$

Finally, coupling yield can be determined by the resulting integration of the coupling peak normalized to the chosen peak. The integration divided by the expected number of protons is the yield.

$$Yield = \frac{coupling\ Integration}{\#\ of\ protons}$$

Chapter 5: Conclusion and Future Work

This chapter will discuss the overall results from the development of iron oxide nanoparticle (IONP) coating methods and heating applications. In addition, we also discuss our future work and optimization of coating EMG308. This chapter was prepared individually by the author with the permission of other collaborators.

Iron oxide nanoparticles

In Chapter 1, the use of IONPs for biomedical applications was discussed. To review, IONPs are small particles, 1-100 nm, with magnetic Fe_3O_4 or γ-Fe_2O_3 core, which under 20 nm are superparamagnetic.[1] An alternating magnetic field can be applied to bulk IONPs, resulting in spin state switching and magnetic hysteresis creating measurable (increase greater than <1 °C localized increase in temperature.[1] This hyperthermia effect can be employed in both tumor thermal therapy to damage tumors and in rewarming cryopreserved samples. Tumor treatment requires a nanoparticle formulation where IONPs accumulate at the tumor at a concentration for effective thermal therapy. Unfortunately, if injected directly, the vascular blood flow can diffuse magnetic NPs making highly vascularized solid tumors difficult for MFH treatments. Embedding IONPs in embolic agents is a promising option to prevent diffusion of IONPs.[92-93] Liquid embolic agents are particularly promising formulations as embolic agents are dissolved in solutions and are liquid before solidifying or gelling in-situ. IONPs can be co-dissolved in solution with liquid embolic agents. Additionally, embolic agents have been used previously for treatment of other tumors.[21]

IONPs formulations must be optimized for use, and tumor treatment has vastly different needs than cryopreservation needs. Cryopreservation to the ice-free vitrified or glassy state requires CPAs. CPAs are complex aqueous organic ionic solutions. IONPs for nanowarming cryopreserved samples and must be colloidally stable in CPA and heat at a high rate.[25] We have tested several IONPs for this use and found that commercial IONPs EMG1200 and EMG308 were not stable in CPA. msIONPs were stable in CPA and high

heating, but expensive to scale up (1g Fe = $2,000 per human kidney). [27] Silica coated IONPs (sIONPs) are stable in CPA and have high heating. In addition, they are optimized for cost ($0.50/mg, or $500/human kidney) and scale up. However, the sIONPs are time-consuming to purify and required a three-fold increase in diameter (27x increase in volume fraction), resulting in a decreased maximum iron concentration.[7, 27] Phosphonate small molecule coatings on IONPs are inexpensive, biocompatible, easy to synthesize, and small.[35-39, 43, 46-49, 52] We chose to explore a phosphonate small molecule linker for coating IONPs in cryopreservation applications.

Tumor thermal therapy

Chapter 2 described the development of an injectable thermal therapy implant for deep tumors, such as glioblastoma. PHIL, a liquid embolic agent, was used as a carrier vehicle and embolic support structure for a magnetic hyperthermia implant. IONPs did not affect the PHIL precipitation from solution and embedded in PHIL upon precipitation. IONPs coprecipitated with PHIL in all models tested: in water to create a tablet, in a 3D AVM agarose model, in a cryotube, and in a postmortem mouse hind limb tumor. The PHIL-IONP precipitate was observable on both μCT (primarily PHIL contrast) and MRI using MB-SWIFT (primarily IONP contrast) as tested on the tablet model. MR imaging was able to observe IONP concentration differences, which in future studies may allow for predictable heating or further tuning heating profiles based on precipitate deposit. It was demonstrated that despite the ability to encapsulate both EMG (IONP core, Ferrotec) and silica coated EMG in PHIL, only the sIONPs are colloidally stable in DMSO and PHIL. We also showed that the addition of IONPs to PHIL does not lead to premature precipitation of PHIL. The stability of the IONPs in the PHIL-DMSO solution affected the

heating capabilities after precipitation. EMG308 had poor colloidal stability in DMSO and had degraded heating when precipitated. sIONPs were able to heat to effective clinical temperatures (above 8 °C) when embedded in PHIL precipitate. Regardless of the coil used, precipitates from any model tested were capable of heating to clinically relevant temperatures, although this was concentration dependent. The precipitate was capable of being heated and reheating multiple times with reproducible temperature rises at each timepoint tested over 1 month in PBS at 37 °C. PHIL-sIONPs were capable of injecting into and solidifying in postmortem mouse hind limb tumors. Furthermore, the application of an alternating magnetic field (AMF) from our RF coil was able to heat the embolized tumors to therapeutic temperatures. These results show RF heating of PHIL-sIONP embolic precipitate has potential for thermal treatment of vascularized tumors.

In future studies, PHIL-IONP precipitation will be studied in live animal models. The chemical biocompatibility of PHIL-IONP precipitates will be studied by injecting a range of IONPs concentrations in PHIL using a mouse model. The effect of heating on tumor growth will be studied for clinical relevance; this will be tested using various field strengths and time profiles on the precipitation of PHIL with IONPs in live tumor models. The effect of blood flow on the dispersion of the PHIL-sIONP precipitate in tumor beds and physiology across the animal also will be studied. In addition, optimization of IONP concentration in PHIL formulation, RF field strength profiles, and PHIL deployment in-situ will be characterized and refined.

Coating IONPs for stability in CPA

In Chapter 3, we proposed and characterized the coating of commercial IONPs using a phosphonate small molecule with PEG. The synthesis of a small molecule phosphonate linker (PLink) was completed and confirmed by NMR. PLink was coupled with PEG, and a ligand exchange was used to bind PEG directly to IONP cores. In tests of heating in water, initially hydrophobic IONPs (EMG1200) recoated with PEG were shown to have increased heating capabilities with increased coating concentrations. Additionally, recoating initial hydrophilic EMG308 with PEG did not affect the heating in water. Effectively, the PLink coating did not damage the heating capabilities of the core in EMG308, and the increased dispersion of EMG1200 in water increased heating. Of the three MW tested (PEG500, PEG2000, and PEG5000), PEG5000 had the best stability results on both IONPs. A minimum concentration of 0.4 mmol PEG/g Fe was required to stabilize IONPs, but coating amount was maximized with 0.8 mmol PEG/g Fe, which was determined by TGA and HRMAS NMR. The coating amount resulting in highest heating and longest colloidally stable in VS55, 0.8 mmol PEG5000/g Fe, was selected for subsequent study. Both EMG1200 and EMG308 were coated with this amount of PEG5000 and tested for feasibility with cryopreservation and nanowarming. First, toxicity was tested by incubating cells overnight with a range of IONP concentrations. Neither IONP type nor concentration effected cell viability; cell viability remained comparable to that of fresh cells. Step loading CPA with without IONPs did not demonstrate any effect on viability. Finally, cells were step loaded with CPA and cryopreserved with and without IONPs and nanowarming. Due to increased heating rate, cell survival during nanowarming depended on concentration of IONPs in CPA. Under these conditions, cell survival was 87% with 60 mg/mL of 1200-PEG5000 and 93% with 25 mg Fe/mL of 308-PEG5000. At these

concentrations, the resulting heating rate was at or above 200 °C/min with both IONPs. Future studies will focus on optimizing the ligand exchange and coating of PLink-PEG5000 on EMG308. In addition, we will seek to determine the maximum concentration of IONPs in CPA and the maximum heating rate.

Our future work will be geared toward optimizing the PEG coating on IONPs for stability in CPA at large scale for cryopreserving organs of human scale. This will require upwards of 2 g Fe per kidney. The reaction of IONPs EMG308 (27-120 mg Fe, 0.5-2 mLs EMG308)-with PLink-PEG5000 (0.08-0.2 g, 0.016-0.039 mmol) was optimized based on reaction solvents (DMSO, acetonitrile, and isopropanol), temperatures (20-80 °C), concentrations (6-50 mg Fe/mL), sonication (10 minutes-3 hours), and times (1-11 days). Metric for success was settling time by visual time lapse videography and aggregation by DLS size in VS55 with Euro-Collins. The optimized reaction was tested at large scale (n=3), 9900 mg Fe (180 mL EMG308) with 29 g PLink-PEG5000. Magnetic separation and trans flow filtration (TFF) were used for purification of excess PEG, which further reduced excess PEG. All three scale ups are stable in other CPAs such as VMP and M22 as well as H_2O, but stability in VS55 with EC varied by reaction conditions. Control IONPs, and partially optimized IONPs (80 °C, 1 day, 12 mg Fe/mL) had no statistical difference in heating capabilities, i.e., specific absorption rate (SAR). Additionally, there is less than 0.5% wt % difference of IONP between batches by TGA and confirmed with HRMAS NMR. Optimized IONPs at 150 mg Fe/mL were used to heat from -196 °C to -20 °C in 5 seconds (2112 °C/min), (360 kHz and 20 kA/m), 30x faster than published work. We will continue to investigate repeatability and characterization of IONPs for large scale synthesis. Additionally, we will study ice formation in samples upon cooling to determine

appropriate CPAs for organ nanowarming. Finally, we will consider PLink coated EMG308 IONPs perfused through organs for cryopreservation and nanowarming feasibility.

NMR characterization of PEG

In chapter 4, we discussed characterization methods of the PEG polymer. ^{1}H NMR characterization is a commonly used widespread technique for analysis of compounds such as polymers to determine chemical purity, yield, and molecular weight. Polymers such as polyethylene glycols often are analyzed in part by this method but have a slight complication with repeating monomers, creating an unfamiliar type of coupling peak which can result in misinterpretation. Due to the fraction of terminal group to repeating monomer unit on a polymer being small, the 1.1% natural abundance of carbon-13 spin splitting must be accounted for in standard one-dimensional ^{1}H NMR spectra. A ^{13}C decoupled ^{1}H pulse sequence can be used to avoid misinterpretation, but this practice is not standard for general chemistry. Once correctly identified, the coupling of ^{1}H- ^{13}C on to the 4 H's of the CH_2CH_2O repeating monomer groups in the polymers can be used as a reference to normalize the spectra or calculate both the molecular weight and the conjugation efficacy of the polymer. This method was compared to SEC and MS and was more accurate in determining conjugation yield and satisfactory in determining MW. Therefore, this NMR method can be used for organic polymers other than PEG with similar results.

References

1. Mahmoudi, M.; Sant, S.; Wang, B.; Laurent, S.; Sen, T., Superparamagnetic iron oxide nanoparticles (SPIONs): development, surface modification and applications in chemotherapy. *Adv Drug Deliv Rev* **2011,** *63* (1-2), 24-46.
2. Salvatore, A.; Montis, C.; Berti, D.; Baglioni, P., Multifunctional Magnetoliposomes for Sequential Controlled Release. *ACS Nano* **2016,** *10* (8), 7749-60.
3. Pasek-Allen, J. L.; Wilharm, R. K.; Gao, Z.; Pierre, V. C.; Bischof, J. C., Phosphonate coating of commercial iron oxide nanoparticles for nanowarming cryopreserved samples. *Journal of Materials Chemistry B* **2022**.
4. Manuchehrabadi, N.; Gao, Z.; Zhang, J.; Ring Hattie, L.; Shao, Q.; Liu, F.; McDermott, M.; Fok, A.; Rabin, Y.; Brockbank Kelvin, G. M.; Garwood, M.; Haynes Christy, L.; Bischof John, C., Improved tissue cryopreservation using inductive heating of magnetic nanoparticles. *Science Translational Medicine* **2017,** *9* (379), eaah4586.
5. Sharma, A.; Rao, J. S.; Han, Z.; Gangwar, L.; Namsrai, B.; Gao, Z.; Ring, H. L.; Magnuson, E.; Etheridge, M.; Wowk, B.; Fahy, G. M.; Garwood, M.; Finger, E. B.; Bischof, J. C., Vitrification and Nanowarming of Kidneys. *Advanced Science* **2021,** *8* (19), 2101691.
6. Gao, Z.; Namsrai, B.; Han, Z.; Joshi, P.; Rao, J. S.; Ravikumar, V.; Sharma, A.; Ring, H. L.; Idiyatullin, D.; Magnuson, E. C.; Iaizzo, P. A.; Tolkacheva, E. G.; Garwood, M.; Rabin, Y.; Etheridge, M.; Finger, E. B.; Bischof, J. C., Vitrification and Rewarming of Magnetic Nanoparticle-Loaded Rat Hearts. *Advanced Materials Technologies* **2022,** *7* (3), 2100873.
7. Gao, Z.; Ring, H. L.; Sharma, A.; Namsrai, B.; Tran, N.; Finger, E. B.; Garwood, M.; Haynes, C. L.; Bischof, J. C., Preparation of Scalable Silica-Coated Iron Oxide Nanoparticles for Nanowarming. *Advanced Science* **2020,** *7* (4), 1901624.
8. Dani, R. K.; Schumann, C.; Taratula, O.; Taratula, O., Temperature-tunable iron oxide nanoparticles for remote-controlled drug release. *AAPS PharmSciTech* **2014,** *15* (4), 963-972.
9. Mai, B. T.; Balakrishnan, P. B.; Barthel, M. J.; Piccardi, F.; Niculaes, D.; Marinaro, F.; Fernandes, S.; Curcio, A.; Kakwere, H.; Autret, G.; Cingolani, R.; Gazeau, F.; Pellegrino, T., Thermoresponsive Iron Oxide Nanocubes for an Effective Clinical Translation of Magnetic Hyperthermia and Heat-Mediated Chemotherapy. *ACS Applied Materials & Interfaces* **2019,** *11* (6), 5727-5739.
10. M, J.; U, G.; B, T.; K, T.; CH, C.; N, W.; R, S.; A, J.; SA, L.; P, W., Thermotherapy of prostate cancer using magnetic nanoparticles: feasibility, imaging, and three-dimensional temperature distribution. *European urology* **2007,** *52* (6).
11. K, G. R.; R, M.; D, S. W.; C, H. R.; C, P. J.; B, T. C., Selective Inductive Heating of Lymph Nodes. *Annals of surgery* **1957,** *vol. 146*.
12. AA, E.; M, S.; M, A.; A, E.-S.; HA, S., Magnetic nanoparticle-induced hyperthermia treatment under magnetic resonance imaging. *Magnetic resonance imaging* **2011,** *29* (2).
13. Das, P.; Colombo, M.; Prosperi, D., Recent advances in magnetic fluid hyperthermia for cancer therapy. *Colloids and Surfaces B: Biointerfaces* **2019,** *174*, 42-55.
14. Johannsen, M.; Gneveckow, U.; Taymoorian, K.; Thiesen, B.; Waldöfner, N.; Scholz, R.; Jung, K.; Jordan, A.; Wust, P.; Loening, S. A., Morbidity and quality of life during thermotherapy using magnetic nanoparticles in locally recurrent prostate cancer: Results of a prospective phase I trial. *International Journal of Hyperthermia* **2007,** *23* (3), 315-323.
15. Johannsen, M.; Thiesen, B.; Wust, P.; Jordan, A., Magnetic nanoparticle hyperthermia for prostate cancer. *International Journal of Hyperthermia* **2010,** *26* (8), 790-795.

16. Maier-Hauff, K.; Rothe, R.; Scholz, R.; Gneveckow, U.; Wust, P.; Thiesen, B.; Feussner, A.; von Deimling, A.; Waldoefner, N.; Felix, R.; Jordan, A., Intracranial Thermotherapy using Magnetic Nanoparticles Combined with External Beam Radiotherapy: Results of a Feasibility Study on Patients with Glioblastoma Multiforme. *Journal of Neuro-Oncology* **2007,** *81* (1), 53-60.
17. Study of Focal Ablation of the Prostate With NanoTherm® Therapy System for Intermediate-Risk Prostate Cancer - Full Text View - ClinicalTrials.gov. 2022.
18. Mahmoudi, K.; Bouras, A.; Bozec, D.; Ivkov, R.; Hadjipanayis, C., Magnetic hyperthermia therapy for the treatment of glioblastoma: a review of the therapy's history, efficacy and application in humans. *International journal of hyperthermia : the official journal of European Society for Hyperthermic Oncology, North American Hyperthermia Group* **2018,** *34* (8), 1316-1328.
19. Feng, Q.; Liu, Y.; Huang, J.; Chen, K.; Huang, J.; Xiao, K., Uptake, distribution, clearance, and toxicity of iron oxide nanoparticles with different sizes and coatings. *Scientific Reports* **2018,** *8* (1), 2082.
20. Rosenblum, D.; Joshi, N.; Tao, W.; Karp, J. M.; Peer, D., Progress and challenges towards targeted delivery of cancer therapeutics. *Nature Communications* **2018,** *9* (1), 1410.
21. Sun, Z.; Song, C.; Wang, C.; Hu, Y.; Wu, J., Hydrogel-Based Controlled Drug Delivery for Cancer Treatment: A Review. *Molecular Pharmaceutics* **2020,** *17* (2), 373-391.
22. Plitz, J.; Rabin, Y.; Walsh, J. R., The effect of thermal expansion of ingredients on the cocktails VS55 and DP6. *Cell Preservation Technology* **2004,** *2* (3), 215-226.
23. Fahy, G. M.; Wowk, B.; Wu, J.; Phan, J.; Rasch, C.; Chang, A.; Zendejas, E., Cryopreservation of organs by vitrification: perspectives and recent advances. *Cryobiology* **2004,** *48* (2), 157-78.
24. Han, Z.; Bishop, J. C., PERSPECTIVE: Critical Cooling and Warming Rates as a Function of CPA Concentration. *Cryo letters* **2020,** *41* (4), 185-193.
25. Manuchehrabadi, N.; Shi, M.; Roy, P.; Han, Z.; Qiu, J.; Xu, F.; Lu, T. J.; Bischof, J., Ultrarapid Inductive Rewarming of Vitrified Biomaterials with Thin Metal Forms. *Annals of biomedical engineering* **2018,** *46* (11), 1857-1869.
26. Taylor, M.; Song, Y.; Brockbank, K., Vitrification in Tissue Preservation. In *Life in the Frozen State*, CRC Press: 2004; pp 603-641.
27. Manuchehrabadi, N.; Gao, Z.; Zhang, J.; Ring, H. L.; Shao, Q.; Liu, F.; McDermott, M.; Fok, A.; Rabin, Y.; Brockbank, K. G. M.; Garwood, M.; Haynes, C. L.; Bischof, J. C., Improved tissue cryopreservation using inductive heating of magnetic nanoparticles. *Sci Transl Med* **2017,** *9* (379).
28. Ring, H.; Tong, S.; Gao, Z.; Manuchehrabadi, N.; Jiang, K.; Pailloux, S.; Dresel, M.; Pierre, V.; Haynes, C.; Garwood, M.; Bao, G.; Bischof, J., Designing Iron Oxide Nanoparticles for Image Guided Thermal Medicine Applications. American Chemical Society (ACS): 2019.
29. Etheridge, M. L.; Hurley, K. R.; Zhang, J.; Jeon, S.; Ring, H. L.; Hogan, C.; Haynes, C. L.; Garwood, M.; Bischof, J. C., Accounting for biological aggregation in heating and imaging of magnetic nanoparticles. *Technology* **2014,** *2* (3), 214-228.
30. Jeon, S.; Hurley, K. R.; Bischof, J. C.; Haynes, C. L.; Hogan, C. J., Quantifying intra- and extracellular aggregation of iron oxide nanoparticles and its influence on specific absorption rate. *Nanoscale* **2016,** *8* (35), 16053-64.
31. Tong, S.; Quinto, C. A.; Zhang, L.; Mohindra, P.; Bao, G., Size-Dependent Heating of Magnetic Iron Oxide Nanoparticles. *ACS nano* **2017,** *11 7*, 6808-6816.
32. Tong, S.; Quinto, C. A.; Zhang, L.; Mohindra, P.; Bao, G., Size-Dependent Heating of Magnetic Iron Oxide Nanoparticles. *ACS Nano* **2017,** *11* (7), 6808-6816.

33. Hurley, K. R.; Ring, H. L.; Etheridge, M.; Zhang, J.; Gao, Z.; Shao, Q.; Klein, N. D.; Szlag, V. M.; Chung, C.; Reineke, T. M.; Garwood, M.; Bischof, J. C.; Haynes, C. L., Predictable Heating and Positive MRI Contrast from a Mesoporous Silica-Coated Iron Oxide Nanoparticle. *Molecular Pharmaceutics* **2016,** *13* (7), 2172-2183.
34. Zahn, N.; Kickelbick, G., Synthesis and aggregation behavior of hybrid amphiphilic titania Janus nanoparticles via surface-functionalization in Pickering emulsions. *Colloids and Surfaces A: Physicochemical and Engineering Aspects* **2014,** *461*, 142-150.
35. Tudisco, C.; Oliveri, V.; Cantarella, M.; Vecchio, G.; Condorelli, G. G., Cyclodextrin Anchoring on Magnetic Fe3O4 Nanoparticles Modified with Phosphonic Linkers. *European Journal of Inorganic Chemistry* **2012,** *2012* (32), 5323-5331.
36. Tudisco, C.; Cambria, M. T.; Sinatra, F.; Bertani, F.; Alba, A.; Giuffrida, A. E.; Saccone, S.; Fantechi, E.; Innocenti, C.; Sangregorio, C.; Dalcanale, E.; Condorelli, G. G., Multifunctional magnetic nanoparticles for enhanced intracellular drug transport. *Journal of Materials Chemistry B* **2015,** *3* (20), 4134-4145.
37. Tudisco, C.; Cambria, M. T.; Condorelli, G. G., Chapter 12 - Multifunctional Magnetic Nanoparticles for Theranostic Applications. In *Biomedical Applications of Functionalized Nanomaterials*, Sarmento, B.; das Neves, J., Eds. Elsevier: 2018; pp 335-370.
38. Tudisco, C.; Bertani, F.; Cambria, M. T.; Sinatra, F.; Fantechi, E.; Innocenti, C.; Sangregorio, C.; Dalcanale, E.; Condorelli, G. G., Functionalization of PEGylated Fe3O4 magnetic nanoparticles with tetraphosphonate cavitand for biomedical application. *Nanoscale* **2013,** *5* (23), 11438-11446.
39. Smolensky, E. D.; Park, H. Y. E.; Berquó, T. S.; Pierre, V. C., Surface functionalization of magnetic iron oxide nanoparticles for MRI applications – effect of anchoring group and ligand exchange protocol. *Contrast Media & Molecular Imaging* **2011,** *6* (4), 189-199.
40. Shultz, M. D.; Reveles, J. U.; Khanna, S. N.; Carpenter, E. E., Reactive Nature of Dopamine as a Surface Functionalization Agent in Iron Oxide Nanoparticles. *Journal of the American Chemical Society* **2007,** *129* (9), 2482-2487.
41. Mohapatra, S.; Pramanik, P., Synthesis and stability of functionalized iron oxide nanoparticles using organophosphorus coupling agents. *Colloids and Surfaces A: Physicochemical and Engineering Aspects* **2009,** *339* (1), 35-42.
42. Mazur, M.; Barras, A.; Kuncser, V.; Galatanu, A.; Zaitzev, V.; Turcheniuk, K. V.; Woisel, P.; Lyskawa, J.; Laure, W.; Siriwardena, A.; Boukherroub, R.; Szunerits, S., Iron oxide magnetic nanoparticles with versatile surface functions based on dopamine anchors. *Nanoscale* **2013,** *5* (7), 2692-2702.
43. Lam, T.; Avti, P. K.; Pouliot, P.; Tardif, J.-C.; Rhéaume, É.; Lesage, F.; Kakkar, A., Surface engineering of SPIONs: role of phosphonate ligand multivalency in tailoring their efficacy. *Nanotechnology* **2016,** *27* (41), 415602.
44. Korpany, K. V.; Majewski, D. D.; Chiu, C. T.; Cross, S. N.; Blum, A. S., Iron Oxide Surface Chemistry: Effect of Chemical Structure on Binding in Benzoic Acid and Catechol Derivatives. *Langmuir* **2017,** *33* (12), 3000-3013.
45. Davis, K.; Cole, B.; Ghelardini, M.; Powell, B. A.; Mefford, O. T., Quantitative Measurement of Ligand Exchange with Small-Molecule Ligands on Iron Oxide Nanoparticles via Radioanalytical Techniques. *Langmuir* **2016,** *32* (51), 13716-13727.
46. Daou, T. J.; Buathong, S.; Ung, D.; Donnio, B.; Pourroy, G.; Guillon, D.; Bégin, S., Investigation of the grafting rate of organic molecules on the surface of magnetite nanoparticles as a function of the coupling agent. *Sensors and Actuators B: Chemical* **2007,** *126* (1), 159-162.

47. Daou, T. J.; Begin-Colin, S.; Grenèche, J. M.; Thomas, F.; Derory, A.; Bernhardt, P.; Legaré, P.; Pourroy, G., Phosphate Adsorption Properties of Magnetite-Based Nanoparticles. *Chemistry of Materials* **2007,** *19* (18), 4494-4505.
48. Bonvin, D.; Aschauer, U. J.; Bastiaansen, J. A. M.; Stuber, M.; Hofmann, H.; Mionić Ebersold, M., Versatility of Pyridoxal Phosphate as a Coating of Iron Oxide Nanoparticles. *Nanomaterials (Basel, Switzerland)* **2017,** *7* (8), 202.
49. Basly, B.; Popa, G.; Fleutot, S.; Pichon, B. P.; Garofalo, A.; Ghobril, C.; Billotey, C.; Berniard, A.; Bonazza, P.; Martinez, H.; Felder-Flesch, D.; Begin-Colin, S., Effect of the nanoparticle synthesis method on dendronized iron oxides as MRI contrast agents. *Dalton Transactions* **2013,** *42* (6), 2146-2157.
50. Davis, K.; Qi, B.; Witmer, M.; Kitchens, C. L.; Powell, B. A.; Mefford, O. T., Quantitative Measurement of Ligand Exchange on Iron Oxides via Radiolabeled Oleic Acid. *Langmuir* **2014,** *30* (36), 10918-10925.
51. Maier, G. P.; Bernt, C. M.; Butler, A., Catechol oxidation: considerations in the design of wet adhesive materials. *Biomaterials Science* **2018,** *6* (2), 332-339.
52. Daou, T. J.; Grenèche, J. M.; Pourroy, G.; Buathong, S.; Derory, A.; Ulhaq-Bouillet, C.; Donnio, B.; Guillon, D.; Begin-Colin, S., Coupling Agent Effect on Magnetic Properties of Functionalized Magnetite-Based Nanoparticles. *Chemistry of Materials* **2008,** *20* (18), 5869-5875.
53. Stauffer, P. R., Evolving technology for thermal therapy of cancer. *International Journal of Hyperthermia* **2005,** *21* (8), 731-744.
54. A, A.; SK, K.; M, W.; H, Z.; C, C.; M, A.; M, H.; Y, Z.; TL, D.; C, H.; R, I., Magnetic nanoparticle hyperthermia enhances radiation therapy: A study in mouse models of human prostate cancer. *International journal of hyperthermia : the official journal of European Society for Hyperthermic Oncology, North American Hyperthermia Group* **2015,** *31* (4).
55. Le Renard, P. E.; Jordan, O.; Faes, A.; Petri-Fink, A.; Hofmann, H.; Rüfenacht, D.; Bosman, F.; Buchegger, F.; Doelker, E., The in vivo performance of magnetic particle-loaded injectable, in situ gelling, carriers for the delivery of local hyperthermia. *Biomaterials* **2010,** *31* (4), 691-705.
56. Zhang, Z.-Q.; Song, S.-C., Thermosensitive/superparamagnetic iron oxide nanoparticle-loaded nanocapsule hydrogels for multiple cancer hyperthermia. *Biomaterials* **2016,** *106*, 13-23.
57. Vollherbst, D. F.; Chapot, R.; Bendszus, M.; Möhlenbruch, M. A., Glue, Onyx, Squid or PHIL? Liquid embolic agents for the embolization of cerebral arteriovenous malformations and dural arteriovenous fistulas. *Clinical Neuroradiology* **2021**, 1-14.
58. Giwa, S.; Lewis, J. K.; Alvarez, L.; Langer, R.; Roth, A. E.; Church, G. M.; Markmann, J. F.; Sachs, D. H.; Chandraker, A.; Wertheim, J. A.; Rothblatt, M.; Boyden, E. S.; Eidbo, E.; Lee, W. P. A.; Pomahac, B.; Brandacher, G.; Weinstock, D. M.; Elliott, G.; Nelson, D.; Acker, J. P.; Uygun, K.; Schmalz, B.; Weegman, B. P.; Tocchio, A.; Fahy, G. M.; Storey, K. B.; Rubinsky, B.; Bischof, J.; Elliott, J. A. W.; Woodruff, T. K.; Morris, G. J.; Demirci, U.; Brockbank, K. G. M.; Woods, E. J.; Ben, R. N.; Baust, J. G.; Gao, D.; Fuller, B.; Rabin, Y.; Kravitz, D. C.; Taylor, M. J.; Toner, M., The promise of organ and tissue preservation to transform medicine. *Nature Biotechnology* **2017,** *35* (6), 530-542.
59. Ravikumar, R.; Leuvenink, H.; Friend, P. J., Normothermic liver preservation: a new paradigm? *Transplant International* **2015,** *28* (6), 690-699.
60. Sack, K., Transplant Experts Blame Allocation System for Discarding Kidneys. **2012**.
61. Wigfield, C. H.; Cypel, M.; Yeung, J.; Waddell, T.; Alex, C.; Johnson, C.; Keshavjee, S.; Love, R. B., Successful Emergent Lung Transplantation After RemoteEx VivoPerfusion Optimization and Transportation of Donor Lungs. *American Journal of Transplantation* **2012,** *12* (10), 2838-2844.

62. Srinivasan, A.; Burton, E. C.; Kuehnert, M. J.; Rupprecht, C.; Sutker, W. L.; Ksiazek, T. G.; Paddock, C. D.; Guarner, J.; Shieh, W.-J.; Goldsmith, C.; Hanlon, C. A.; Zoretic, J.; Fischbach, B.; Niezgoda, M.; El-Feky, W. H.; Orciari, L.; Sanchez, E. Q.; Likos, A.; Klintmalm, G. B.; Cardo, D.; LeDuc, J.; Chamberland, M. E.; Jernigan, D. B.; Zaki, S. R., Transmission of Rabies Virus from an Organ Donor to Four Transplant Recipients. *New England Journal of Medicine* **2005,** *352* (11), 1103-1111.
63. HIV Transmitted from a Living Organ Donor-New York City, 2009. *American Journal of Transplantation* **2011,** *11* (6), 1334-1337.
64. CDC Media Relations: Press Release. https://www.cdc.gov/media/pressrel/r020927d.htm.
65. Hsin, M. K.; Zamel, R.; Cypel, M.; Hashimoto, K.; Chen, M.; Machuca, T.; Wishart, D.; Han, B.; Waddell, T. K.; Liu, M.; Keshavjee, S., Metabolic Profiling of Perfusate from Clinical Ex Vivo Lung Perfusion Yields Potential Biomarkers of Early Lung Transplant Outcomes. *The Journal of Heart and Lung Transplantation* **2014,** *33* (4), S96-S97.
66. Hosgood, S. A.; Barlow, A. D.; Hunter, J. P.; Nicholson, M. L., Ex vivonormothermic perfusion for quality assessment of marginal donor kidney transplants. *British Journal of Surgery* **2015,** *102* (11), 1433-1440.
67. Bruinsma, B. G.; Sridharan, G. V.; Weeder, P. D.; Avruch, J. H.; Saeidi, N.; Özer, S.; Geerts, S.; Porte, R. J.; Heger, M.; van Gulik, T. M.; Martins, P. N.; Markmann, J. F.; Yeh, H.; Uygun, K., Metabolic profiling during ex vivo machine perfusion of the human liver. *Scientific Reports* **2016,** *6* (1).
68. Hosgood, S. A.; van Heurn, E.; Nicholson, M. L., Normothermic machine perfusion of the kidney: better conditioning and repair? *Transplant International* **2014,** *28* (6), 657-664.
69. Whitson, B. A.; Black, S. M., Organ assessment and repair centers: The future of transplantation is near. *World Journal of Transplantation* **2014,** *4* (2), 40.
70. Advancing Tissue Science and Engineering: A Foundation for the Future A Multi-Agency Strategic Plan. *Tissue Engineering* **2007,** *13* (12), 2825-2826.
71. White House Highlights AST's New Initiative with Organ Preservation Alliance. 2016.
72. Kandaswamy, R.; Skeans, M. A.; Gustafson, S. K.; Carrico, R. J.; Tyler, K. H.; Israni, A. K.; Snyder, J. J.; Kasiske, B. L., OPTN/SRTR 2013 Annual Data Report: Pancreas. *American Journal of Transplantation* **2015,** *15* (S2), 1-20.
73. Rall, W. F.; Fahy, G. M., Ice-free cryopreservation of mouse embryos at −196 °C by vitrification. *Nature* **1985,** *313* (6003), 573-575.
74. Fahy, G. M.; Wowk, B.; Wu, J.; Paynter, S., Erratum to “Improved vitrification solutions based on the predictability of vitrification solution toxicity” [Cryobiology 48 (2004) 22–35]. *Cryobiology* **2004,** *48* (3), 365.
75. Fahy, G. M.; MacFarlane, D. R.; Angell, C. A.; Meryman, H. T., Vitrification as an approach to cryopreservation. *Cryobiology* **1984,** *21* (4), 407-426.
76. Brockbank, K.; Walsh, J.; Song, Y.; Taylor, M., Vitrification. In *Encyclopedia of Biomaterials and Biomedical Engineering, Second Edition - Four Volume Set*, CRC Press: 2008; pp 3046-3057.
77. Baicu, S.; Taylor, M. J.; Chen, Z.; Rabin, Y., Vitrification of Carotid Artery Segments: An Integrated Study of Thermophysical Events And Functional Recovery Toward Scale-Up for Clinical Applications. *Cell Preservation Technology* **2006,** *4* (4), 236-244.
78. Rovers, S. A.; van der Poel, L. A. M.; Dietz, C. H. J. T.; Noijen, J. J.; Hoogenboom, R.; Kemmere, M. F.; Kopinga, K.; Keurentjes, J. T. F., Characterization and Magnetic Heating of Commercial Superparamagnetic Iron Oxide Nanoparticles. *The Journal of Physical Chemistry C* **2009,** *113* (33), 14638-14643.

79. Walkey, C. D.; Olsen, J. B.; Guo, H.; Emili, A.; Chan, W. C. W., Nanoparticle Size and Surface Chemistry Determine Serum Protein Adsorption and Macrophage Uptake. *Journal of the American Chemical Society* **2012,** *134* (4), 2139-2147.
80. Hirsch, L. R.; Stafford, R. J.; Bankson, J. A.; Sershen, S. R.; Rivera, B.; Price, R. E.; Hazle, J. D.; Halas, N. J.; West, J. L., Nanoshell-mediated near-infrared thermal therapy of tumors under magnetic resonance guidance. *Proceedings of the National Academy of Sciences* **2003,** *100* (23), 13549-13554.
81. Gemert, M. J. C. v.; Welch, A. J., Clinical use of laser-tissue interactions. *IEEE Engineering in Medicine and Biology Magazine* **1989,** *8* (4), 10-13.
82. Ko, G.; Choi, J. W.; Lee, N.; Kim, D.; Hyeon, T.; Kim, H. C., Recent progress in liquid embolic agents. *Biomaterials* **2022,** *287*, 121634.
83. Mohammadi, A. M.; Hawasli, A. H.; Rodriguez, A.; Schroeder, J. L.; Laxton, A. W.; Elson, P.; Tatter, S. B.; Barnett, G. H.; Leuthardt, E. C., The role of laser interstitial thermal therapy in enhancing progression-free survival of difficult-to-access high-grade gliomas: a multicenter study. *Cancer medicine* **2014,** *3* (4), 971-9.
84. Jordan, A.; Scholz, R.; Wust, P.; Fähling, H.; Felix, R., Magnetic fluid hyperthermia (MFH): Cancer treatment with AC magnetic field induced excitation of biocompatible superparamagnetic nanoparticles. *Journal of Magnetism and Magnetic Materials* **1999,** *201*, 413-419.
85. Diederich, C. J., Thermal ablation and high-temperature thermal therapy: overview of technology and clinical implementation. *Int J Hyperthermia* **2005,** *21* (8), 745-53.
86. Shah, R. R.; Dombrowsky, A. R.; Paulson, A. L.; Johnson, M. P.; Nikles, D. E.; Brazel, C. S., Determining iron oxide nanoparticle heating efficiency and elucidating local nanoparticle temperature for application in agarose gel-based tumor model. *Materials Science and Engineering: C* **2016,** *68*, 18-29.
87. FS, B.; B., G., *Biological and Medical Aspects of Electromagnetic Fields | Ben Greeneb*. CRC Press, Taylor & Francis Group: Boca Raton (FL), 2006.
88. A, A.; J, J.; A, S.; SK, K.; V, N.; C, Y.; TL, D.; A, K.; RC, G.; R, I., Design and construction of a Maxwell-type induction coil for magnetic nanoparticle hyperthermia. *International journal of hyperthermia : the official journal of European Society for Hyperthermic Oncology, North American Hyperthermia Group* **2020,** *37* (1).
89. C, K.; Y, Z.; M, H.; H, Z.; C, C.; D, B.; J, M.; M, W.; E, B.; C, G.; A, G.; C, B.; TL, D.; R, I., Preliminary study of injury from heating systemically delivered, nontargeted dextran-superparamagnetic iron oxide nanoparticles in mice. *Nanomedicine (London, England)* **2012,** *7* (11).
90. WJ, A.; IA, B.; DP, C., Usable frequencies in hyperthermia with thermal seeds. *IEEE transactions on bio-medical engineering* **1984,** *31* (1).
91. Krishnan, S.; Diagaradjane, P.; Cho, S. H., Nanoparticle-mediated thermal therapy: evolving strategies for prostate cancer therapy. *Int J Hyperthermia* **2010,** *26* (8), 775-89.
92. Giustini, A. J.; Petryk, A. A.; Cassim, S. M.; Tate, J. A.; Baker, I.; Hoopes, P. J., Magnetic nanoparticle hyperthermia in cancer treatment. *Nano Life* **2010,** *1* (01n02), 17-32.
93. Deatsch, A. E.; Evans, B. A., Heating efficiency in magnetic nanoparticle hyperthermia. *Journal of Magnetism and Magnetic Materials* **2014,** *354*, 163-172.
94. Yu, K.; Liang, B.; Zheng, Y.; Exner, A.; Kolios, M.; Xu, T.; Guo, D.; Cai, X.; Wang, Z.; Ran, H.; Chu, L.; Deng, Z., PMMA-Fe(3)O(4) for internal mechanical support and magnetic thermal ablation of bone tumors. *Theranostics* **2019,** *9* (14), 4192-4207.
95. Vollherbst, D. F.; Sommer, C. M.; Ulfert, C.; Pfaff, J.; Bendszus, M.; Möhlenbruch, M. A., Liquid Embolic Agents for Endovascular Embolization: Evaluation of an Established (Onyx) and a

Novel (PHIL) Embolic Agent in an In Vitro AVM Model. *American Journal of Neuroradiology* **2017,** *38* (7), 1377.
96. Sirakov, S. S.; Sirakov, A.; Minkin, K.; Hristov, H.; Ninov, K.; Penkov, M.; Karakostov, V.; Orlov, K.; Gorbatykh, A.; Kislitsin, D.; Raychev, R., Initial experience with precipitating hydrophobic injectable liquid in cerebral arteriovenous malformations. *Interventional Neuroradiology* **2019,** *25* (1), 58-65.
97. Lucatelli, P.; Corona, M.; Teodoli, L.; Nardis, P.; Cannavale, A.; Rocco, B.; Trobiani, C.; Cipollari, S.; Zilahi De Gyurgyokai, S.; Bezzi, M.; Catalano, C., Use of Phil Embolic Agent for Bleeding in Non-Neurological Interventions. *Journal of Clinical Medicine* **2021,** *10* (4), 701.
98. Idiyatullin, D.; Corum, C. A.; Garwood, M., Multi-Band-SWIFT. *J Magn Reson* **2015,** *251*, 19-25.
99. Look, D. C.; Locker, D. R., Time saving in measurement of NMR and EPR relaxation times. *Review of Scientific Instruments* **1970,** *41* (2), 250-251.
100. Zhang, J.; Chamberlain, R.; Etheridge, M.; Idiyatullin, D.; Corum, C.; Bischof, J.; Garwood, M., Quantifying iron-oxide nanoparticles at high concentration based on longitudinal relaxation using a three-dimensional SWIFT Look-Locker sequence. *Magn Reson Med* **2014,** *71* (6), 1982-1988.
101. Schneider, C. A.; Rasband, W. S.; Eliceiri, K. W., NIH Image to ImageJ: 25 years of image analysis. *Nature Methods* **2012,** *9* (7), 671-675.
102. Etheridge, M. L.; Bischof, J. C., Optimizing magnetic nanoparticle based thermal therapies within the physical limits of heating. *Ann Biomed Eng* **2013,** *41* (1), 78-88.
103. Etheridge, M. L.; Xu, Y.; Rott, L.; Choi, J.; Glasmacher, B.; Bischof, J. C., RF heating of magnetic nanoparticles improves the thawing of cryopreserved biomaterials. *Technology* **2014,** *02* (03), 229-242.
104. HL, R.; A, S.; R, I.; JC, B., The impact of data selection and fitting on SAR estimation for magnetic nanoparticle heating. *International journal of hyperthermia : the official journal of European Society for Hyperthermic Oncology, North American Hyperthermia Group* **2020,** *37* (3).
105. Ranjbartehrani, P.; Etheridge, M.; Ramadhyani, S.; Natesan, H.; Bischof, J.; Shao, Q., Characterization of Miniature Probes for Cryosurgery, Thermal Ablation, and Irreversible Electroporation on Small Animals. *Advanced Therapeutics* **2022,** *n/a* (n/a), 2100212.
106. Smolensky, E.; Park, H.-Y.; Berquo, T.; Pierre, V., Surface Functionalization of Magnetic Iron Oxide Nanoparticles for MRI Applications – Effect of Anchoring Group and Ligand Exchange Protocol. *Contrast media & molecular imaging* **2010,** *6*, 189-99.
107. Vollherbst, D. F.; Otto, R.; Do, T.; Kauczor, H. U.; Bendszus, M.; Sommer, C. M.; Möhlenbruch, M. A., Imaging artifacts of Onyx and PHIL on conventional CT, cone-beam CT and MRI in an animal model. *Interventional Neuroradiology* **2018,** *24* (6), 693-701.
108. SA, S.; WC, D., Thermal dose determination in cancer therapy. *International journal of radiation oncology, biology, physics* **1984,** *10* (6).
109. S, B.; DJ, S.; JC, B., Supraphysiological thermal injury in Dunning AT-1 prostate tumor cells. *Journal of biomechanical engineering* **2000,** *122* (1).
110. Sapareto, S. A.; Dewey, W. C., Thermal dose determination in cancer therapy. *International Journal of Radiation Oncology* Biology* Physics* **1984,** *10* (6), 787-800.
111. Brace, C., Thermal tumor ablation in clinical use. *IEEE Pulse* **2011,** *2* (5), 28-38.
112. X, H.; S, B.; JC, B., Thermal therapy in urologic systems: a comparison of arrhenius and thermal isoeffective dose models in predicting hyperthermic injury. *Journal of biomechanical engineering* **2009,** *131* (7).

113. MP, L., Induced thermal resistance in the mouse ear: the relationship between heating time and temperature. *International journal of radiation biology and related studies in physics, chemistry, and medicine* **1979,** *35* (5).
114. M, N.; V, M.; C, C., Mechanisms of focal heat destruction of liver tumors. *The Journal of surgical research* **2005,** *127* (2).
115. Pomfret, R.; Miranpuri, G.; Sillay, K., The substitute brain and the potential of the gel model. *Ann Neurosci* **2013,** *20* (3), 118-122.
116. Zhang, J.; Ring, H. L.; Hurley, K. R.; Shao, Q.; Carlson, C. S.; Idiyatullin, D.; Manuchehrabadi, N.; Hoopes, P. J.; Haynes, C. L.; Bischof, J. C.; Garwood, M., Quantification and biodistribution of iron oxide nanoparticles in the primary clearance organs of mice using T(1) contrast for heating. *Magn Reson Med* **2017,** *78* (2), 702-712.
117. Etheridge, M. L.; Xu, Y.; Rott, L.; Choi, J.; Glasmacher, B.; Bischof, J. C., RF heating of magnetic nanoparticles improves the thawing of cryopreserved biomaterials. *https://doi.org/10.1142/S2339547814500204* **2014**.
118. Ring, H. L.; Zhang, J.; Klein, N. D.; Eberly, L. E.; Haynes, C. L.; Garwood, M., Establishing the overlap of IONP quantification with echo and echoless MR relaxation mapping. *Magn Reson Med* **2018,** *79* (3), 1420-1428.
119. Hart, A.; Smith, J. M.; Skeans, M. A.; Gustafson, S. K.; Stewart, D. E.; Cherikh, W. S.; Wainright, J. L.; Kucheryavaya, A.; Woodbury, M.; Snyder, J. J.; Kasiske, B. L.; Israni, A. K., OPTN/SRTR 2015 Annual Data Report: Kidney. *Am J Transplant* **2017,** *17 Suppl 1* (Suppl 1), 21-116.
120. Fahy, G. M.; MacFarlane, D. R.; Angell, C. A.; Meryman, H. T., Vitrification as an approach to cryopreservation. *Cryobiology* **1984,** *21* (4), 407-26.
121. Ring, H.; Tong, S.; Gao, Z.; Manuchehrabadi, N.; Jiang, K.; Pailloux, S.; Dresel, M.; Pierre, V.; Haynes, C.; Garwood, M.; Bao, G.; Bischof, J., *Designing Iron Oxide Nanoparticles for Image Guided Thermal Medicine Applications*. 2019.
122. Wang, Y.; Gao, Z.; Han, Z.; Liu, Y.; Yang, H.; Akkin, T.; Hogan, C. J.; Bischof, J. C., Aggregation affects optical properties and photothermal heating of gold nanospheres. *Scientific Reports* **2021,** *11* (1), 898.
123. Tong, S.; Hou, S.; Ren, B.; Zheng, Z.; Bao, G., Self-assembly of phospholipid-PEG coating on nanoparticles through dual solvent exchange. *Nano letters* **2011,** *11* (9), 3720-3726.
124. Sharma, A.; Cornejo, C.; Mihalic, J.; Geyh, A.; Bordelon, D. E.; Korangath, P.; Westphal, F.; Gruettner, C.; Ivkov, R., Physical characterization and in vivo organ distribution of coated iron oxide nanoparticles. *Scientific Reports* **2018,** *8* (1), 4916.
125. Arnaud, F. G.; Khirabadi, B.; Fahy, G. M., Physiological evaluation of a rabbit kidney perfused with VS41A. *Cryobiology* **2003,** *46* (3), 289-294.
126. Rallabandi, R. Toward a Unified Synthesis of Tetrahydro-α-Carboline Based Natural Products and Modular Synthesis and Characterization of Multifunctionalized Fe3O4 Nanoparticles: Application in Gene Delivery and Synthesis of Very Long Chain Polyunsaturated Fatty Acids (VLC-Pufa) and Administration in Mouse Model of STGD3 and AMD. 2018.
127. Goff, J. D.; Huffstetler, P. P.; Miles, W. C.; Pothayee, N.; Reinholz, C. M.; Ball, S.; Davis, R. M.; Riffle, J. S., Novel Phosphonate-Functional Poly(ethylene oxide)-Magnetite Nanoparticles Form Stable Colloidal Dispersions in Phosphate-Buffered Saline. *Chemistry of Materials* **2009,** *21* (20), 4784-4795.
128. Davis, K.; Qi, B.; Witmer, M.; Kitchens, C. L.; Powell, B. A.; Mefford, O. T., Quantitative measurement of ligand exchange on iron oxides via radiolabeled oleic acid. *Langmuir : the ACS journal of surfaces and colloids* **2014,** *30 36*, 10918-25.

129. Chiu-Lam, A.; Staples, E.; Pepine Carl, J.; Rinaldi, C., Perfusion, cryopreservation, and nanowarming of whole hearts using colloidally stable magnetic cryopreservation agent solutions. *Science Advances 7* (2), eabe3005.
130. Neal, C. R.; Arkill, K. P.; Bell, J. S.; Betteridge, K. B.; Bates, D. O.; Winlove, C. P.; Salmon, A. H. J.; Harper, S. J., Novel hemodynamic structures in the human glomerulus. *American Journal of Physiology-Renal Physiology* **2018,** *315* (5), F1370-F1384.
131. Polito, L.; Colombo, M.; Monti, D.; Melato, S.; Caneva, E.; Prosperi, D., Resolving the Structure of Ligands Bound to the Surface of Superparamagnetic Iron Oxide Nanoparticles by High-Resolution Magic-Angle Spinning NMR Spectroscopy. *Journal of the American Chemical Society* **2008,** *130* (38), 12712-12724.
132. Di Palma, J. A.; Smith, J. R.; Cleveland, M., Overnight efficacy of polyethylene glycol laxative. *The American journal of gastroenterology* **2002,** *97* (7), 1776-9.
133. Yuan, L.; Xian Rong, Q.; Yoshie, M.; Tsuneji, N., PEG–PLA diblock copolymer micelle-like nanoparticles as all-trans-retinoic acid carrier: in vitro and in vivo characterizations. *Nanotechnology* **2009,** *20* (5), 055106.
134. Charmainne Cruje; Chithrani, D. B., Polyethylene Glycol Density and Length Affects Nanoparticle Uptake by Cancer Cells. *Journal of Nanomedicine Research* **2014,** *1*.
135. Li, Y.; Kröger, M.; Liu, W. K., Endocytosis of PEGylated nanoparticles accompanied by structural and free energy changes of the grafted polyethylene glycol. *Biomaterials* **2014,** *35* (30), 8467-8478.
136. Zhang, W.; Martinelli, J.; Peters, J. A.; van Hengst, J. M. A.; Bouwmeester, H.; Kramer, E.; Bonnet, C. S.; Szeremeta, F.; Tóth, É.; Djanashvili, K., Surface PEG Grafting Density Determines Magnetic Relaxation Properties of Gd-Loaded Porous Nanoparticles for MR Imaging Applications. *ACS Appl Mater Interfaces* **2017,** *9* (28), 23458-23465.
137. Xiao, R. Z.; Zeng, Z. W.; Zhou, G. L.; Wang, J. J.; Li, F. Z.; Wang, A. M., Recent advances in PEG–PLA block copolymer nanoparticles. *International Journal of Nanomedicine* **2010,** *5*, 1057-1065.
138. Hortal, A. R.; Hurtado, P.; Martínez-Haya, B.; Arregui, A.; Bañares, L., Solvent-Free MALDI Investigation of the Cationization of Linear Polyethers with Alkali Metals. *The Journal of Physical Chemistry B* **2008,** *112* (29), 8530-8535.
139. Bogan, M. J.; Agnes, G. R., Poly(ethylene glycol) doubly and singly cationized by different alkali metal ions: Relative cation affinities and cation-dependent resolution in a quadrupole ion trap mass spectrometer. *Journal of the American Society for Mass Spectrometry* **2002,** *13* (2), 177-186.
140. Ait Bachir, Z.; Huang, Y.; He, M.; Huang, L.; Hou, X.; Chen, R.; Gao, F., Effects of PEG surface density and chain length on the pharmacokinetics and biodistribution of methotrexate-loaded chitosan nanoparticles. *Int J Nanomedicine* **2018,** *13*, 5657-5671.
141. Facchinatto, W.; Fiamingo, A.; Martins, D.; Campana, S., Characterization and physical-chemistry of methoxypoly(ethylene glycol)-g-chitosan. *International Journal of Biological Macromolecules* **2018,** *124*.
142. Mulay, P.; Shrikhande, G.; Puskas, J. E., Synthesis of Mono- and Dithiols of Tetraethylene Glycol and Poly(ethylene glycol)s via Enzyme Catalysis. *Catalysts* **2019,** *9* (3), 228.
143. Harrell, M. L.; Bergbreiter, D. E., Using 1H NMR Spectra of Polymers and Polymer Products To Illustrate Concepts in Organic Chemistry. *Journal of Chemical Education* **2017,** *94* (11), 1668-1673.
144. Izunobi, J. U.; Higginbotham, C. L., Polymer Molecular Weight Analysis by 1H NMR Spectroscopy. *Journal of Chemical Education* **2011,** *88* (8), 1098-1104.